Process Quality Improvement in Thermosonic Wire Bonding

by

Jaesik Lee

A thesis
presented to the University of Waterloo
in fulfillment of the
thesis requirement for the degree of
Doctor of Philosophy
in
Mechanical Engineering

Waterloo, Ontario, Canada, 2008

I hereby declare that I am the sole author of this thesis. This is a true copy of the thesis, including any required final revisions, as accepted by my examiners.

I understand that my thesis may be made electronically available to the public.

Abstract

This thesis demonstrates the feasibility of methods developed to increase the quality of the crescent bond together with the tail bond quality. Low pull force of the crescent bond limits the usage of insulated Au wire in microelectronics assembly. Premature break of the tail which results in the stoppage of the bonding machine is one of obstacles to overcome for Cu wire. The primary focus of this thesis is to understand the tail and crescent bonding process and then to propose methodologies to improve thermosonic wire bonding processes when Cu and insulated Au wires are used.

Several series of experiments to investigate the crescent and tail bonding processes are performed on auto bonders. Cu and insulated Au wires with diameters of 25μm are bonded on the diepads of Ag leadframes. For simplicity, wire loops are oriented perpendicular to the ultrasonic direction.

It was found that the crescent bond breaking force by pulling the wire loop (pull force) with insulated Au wire is about 80 % of that of bare Au wire. A modification of the crescent bonding process is made to increase the pull force with insulated Au wire. In the modified process, an insulation layer removing stage (cleaning stage) is inserted before the bonding stage. The cleaning stage consists of a scratching motion (shift) toward to the ball bond in combination with ultrasound. Bonds are then made on the fresh diepad with the insulation removed from the contact surface of the insulated Au wire. This process increases the pull force of the crescent bond up to 26% which makes it comparable to the results obtained with bare Au wire.

An online tail breaking force measurement method is developed with a proximity sensor between wire clamp and horn. Detailed understanding of tail bond formation is achieved by studying tail bond imprints with scanning electron microscopy and energy dispersive x-ray analysis. Descriptions are given of the dependence of the tail breaking force on the bonding parameters, metallization variation, and cleanliness of the bond pad. Simultaneous optimization with pull force and tail breaking force can optimize the Cu wire bonding process both with high quality and robustness. It is recommended to first carry out conventional pull force optimization followed by a minimization of the bonding force parameter to the lowest value still fulfilling the pull force cpk requirement. The tail bond forms not only under the capillary chamfer, but also under the capillary hole. The tail breaking force includes both the interfacial bond breaking strength and the breaking strength of the thinned portion of the wire that will remain at the substrate as residue.

Close investigations of the tail bond imprint with scanning electron microscopy indicate the presence of fractures of the substrate indicating substrate material being picked up by Cu wire tail. Pick up is found on Au and Cu wires, but the amount of pick up is much larger on Cu wire. The effect on the hardness of the subsequently formed Cu free air ball (FAB) as investigated with scanning electron microscopy and micro - hardness test shows that Cu FABs containing Au and Ag pick ups are softer than those without pick up. However, the hardness varies significantly more with Au pick up. The amount of Au pick up is estimated higher than 0.03 % of the subsequently formed FAB volume, exceeding typical impurity and dopant concentrations (0.01 %) added during manufacturing of the wire.

Acknowledgments

I would like to thank my supervisors Dr. Y. Zhou and Dr. M. Mayer for their input, support and guidance over the duration of this work. This work is supported by MK Electron. Co. Ltd. (Yonging, Korea), Microbonds Inc. (Markham, Canada), Natural Science and Engineering Research Council (NSERC), AuTEK, and Ontario Centres of Excellence (OCE) (all from Canada). I would like to thank everyone in the CAMJ group at University of Waterloo for the help and input they provided to this study. I would like to thank Dr. J. P. Jung for his advice. The technical help of Oerilikon Esec is gratefully acknowledged (Switzerland, USA, and Singapore).

Without the support of my family, the completion of this thesis would have not been possible. My deepest appreciation is to extend to my parents and my fiancee, Miso, for their love and support to fulfill my academic pursuits. I acknowledge with sincerity, the affection and encouragement of my brother, my sister, and my brothers-in-law and my sisters-in-law for their moral support.

To my family

&

fiancee

Table of Contents

List of Figures

List of Tables

Publications

Journal Papers

- J. Lee, M. Mayer, Y. Zhou, S. J. Hong, J. T. Moon, and J. Persic, “Influence of gold pick up on the hardness of copper free air ball,” Submitted to *Microelectron. Reliab*.
- J. Lee, M. Mayer, Y. Zhou, S. J. Hong, and J. T. Moon, “Silver pick up during tail formation and its effect on Cu free air ball diameter and hardness,” Submitted to *IEEE Trans. Comp. Packag. Technol*.
- J. Lee, M. Mayer, Y. Zhou, and J. Persic, “Microelectronic wire bonding with insulated Au wire: Effects of process parameters on insulation removal and crescent bonding,” Accepted in *Mater. Trans*.
- J. Lee, M. Mayer, Y. Zhou, S. J. Hong, and J. T. Moon, “Concurrent optimization of crescent bond pull force and tail breaking force in thermosonic Cu wire bonding process,” Accepted in *IEEE Trans. Electron. Packag. Manuf.*
- J. Lee, M. Mayer, Y. Zhou, S. J. Hong, and S. M. Lee, “Tail breaking force in thermosonic wire bonding with novel bonding wires,” *Materials Science Forum*, Vols. 580 - 582, pp. 201 - 204, 2008.
- J. Lee, M. Mayer, Y. Zhou, and S. J. Hong, “Iterative optimization of tail breaking force of 1mil wire thermosonic ball bonding processes and the influence of plasma cleaning,” *Microelectron. J*. Vol. 38, pp. 842 - 847, 2007.

- J. Lee. M. Mayer. and Y. Zhou, “The feasibility of Au ball bonding on Sn - plated Cu,” *J. Electron. Mater.* Vol. 36, pp. 682 - 689, 2007.

Conference Presentations and Proceedings

- J. Lee, M. Mayer, Y. Zhou, S. J. Hong, and J. T. Moon, “Silver pick - up during tail formation and its effect on free air ball in thermosonic copper ball bonding,” *IEEE Electron. Comp. Technol. Conf. (ECTC)*, Orlando, USA, 2008, pp. 2024 - 2029.
- J. Lee, M. Mayer, Y. Zhou, and J. Persic, “Pull force and tail breaking force optimization of the crescent bonding process with insulated Au wire,” *IEEE Electron. Packag. Technol. Conf. (EPTC)* Singapore, 2007, pp. 725 - 730.
- J. Lee, M. Mayer, Y. Zhou, S. J. Hong, and S. M. Lee, “Tail breaking force in thermosonic wire bonding wire novel bonding wires,” *Intl. Joining Welding Conf. (IJWC)*, Seoul, Korea, 2007, pp. 271,

Chapter 1 Introduction

In the last three decades impressive progress in microelectronics has generated enormous computational power and storage capacity with ever decreasing cost per function [1]. It has led to numerous challenges specially in computing, telecommunication, and consumer devices, driving the microelectronics industry. Microelectronic devices contain many electrical components such as transistors, intergrated circuit chips, diodes, and capacitors. These components need to be interconnected to each other in order to receive power and receive/transmit signals. Interconnection technologies mainly include wire bonding, tape automated bonding (TAB), and flip chip bonding. About 90 % of IC packaging used wire bonding in 2006 [2] due to its high flexibility, low defect rates, high reliability, very large industry infrastructure, and rapid advances in equipment, tools, and materials technology [3]. The market share of wire bonding in 2010 will still be more than 85 %, and in turn 192.2 billion wire bonded units will be made [2]. The assembly cost for wire bond in large die size (17 mm by 17 mm) is 30 % cheaper than that with flip chip connection [2].

With demands for high integration and scale - down in recent IC packages and reduction of wire diameter and increased looping and layout complexity, methods need to be found to accommodate these trends since current bonding wire material has physical limitations. One is to replace bare Au wire with Cu and/or insulated Au wires. The industry is currently trying to implement these changes in the thermosonic wire bonding process.

Thinner diameter Cu wire can be used to obtain the same electrical properties compared to thicker Au wire due to the lower electrical resistivity [4], and higher wire tensile strength and stiffness of Cu [5]. Insulated Au wire can prohibit neighboring wires from short circuiting due to

the insulation layer deposited on Au wire [6, 7]. This insulation layer allows more interconnection per unit area at the chip level and reduces pad and looping limitations.

However, due to the additional layers of foreign material on the wire surface, i.e. oxide layer on Cu and insulation layer on Au wire, respectively, the characteristics of the crescent bonding process are different. There is a lack of quantitative understanding of the crescent bonding process using Cu and insulated Au wires. Advanced crescent bonding process specifications to improve crescent bond quality (strength) does not exist. Further, understanding of the tail bond which is formed together with the crescent bond is lacking. Once the effects of the additional surface layers (Oxide and insulation layers) are better understood, new materials combinations, cost effectiveness, and/or productivity may be realized in thermosonic wire bonding.

Therefore, Copper and insulated Au wires are used in this study. They allow both development of crescent bonding processes for copper and insulated Au wires, and this also facilitates an understanding of the tail bonding process and its effect on the ball bonding process

1.1 Objectives

This study is performed to gain fundamental understandings of crescent and tail bond processes and their interactions with different bonding wire materials. With the knowledge obtained from those two processes, quality improvement in the crescent bonding process is to be assessed. Further, the effects of tail bond on the ball bonding process are to be clarified. To this end, the following tasks are undertaken.

(a) Guidelines developed to improve initial quality of crescent bonds (Insulated Au wire)

(b) Guidelines developed for optimization of the crescent bond process (Cu wire)

(c) Investigation of tail bond formation by carrying out a bond imprint study

(d) Investigation of the influence of substrate material pick up on FAB formation

1.2 Thesis Organization

This work is focused on wire bonding processes based on crescent and tail bond principles. Chapter 1 introduces an overview of thermosonic wire bonding technology. Recent issues in wire bonding are to be assessed. Objectives and organization of this thesis are addressed. Online tail breaking force (TBF) measurement method for tail bond strength measurement is developed [8] and calibrated in Chapter 2. Preliminary comparison of bonding wires are performed. Chapter 3 develops enhancement of crescent bonding quality using an advanced bonding process (cleaning stage process) when insulated Au wire is used [9]. Influence of bonding parameters on insulation removal is discussed. A new concept for the optimization of the crescent bonding process with Cu wire [10] is addressed in Chapter 4. Fundamental understanding of tail bond formation is developed using a tail bond imprint study. Influences of substrate materials picked up by wire tail on free air ball (FAB) formation [11, 12] are explored in Chapter 5.

1.3 Process Description

Wire bonding is an electronic packaging process which provides electrical connection between chip and substrates with fine wires. It has been widely used for the first level interconnection since thermocompression wedge and ball bonding for microelectronics was developed by Bell Laboratories in 1957 [3]. Ultrasonic wedge bonding was introduced to the microelectronics industry about 1960 and became dominant in device production. Concoulas [3] first combined ultrasonic energy with heat to produce thermosonic bonding in 1970. Improvements specially in bonding machines, bonding wire, and capillaries have been taking place since.

Wire bonding uses thin gold, aluminum, or copper wires which are bonded first to the chip metallization and then to the substrate or leadframe metallization. Wire bonding technologies are categorized as thermocompression, ultrasonic, or thermosonic bond depending on the forms of energy applied. More than 95% of all wire bonds are made with thermosonic ball bonding. The thermosonic ball bonding process uses a combination of heat, bonding force, and ultrasonic energy to make a weld at each end of the wire, applied with a needle - like disposable tool called a capillary.

The thermosonic ball bonding process steps are illustrated in Figs. 1.1 (a) - (e). A high - voltage electrical - flame -off (EFO) is applied between wire and an electrode causing the wire to be molten and resolidified, resulting in formation of a ball because of the surface tension of the molten metal [Fig. 1.1 (a)]. The capillary is lowered to the chip, which is typically heated to 150 ^{o}C. The attached transducer delivers ultrasonic oscillation to the capillary. A weld is created between the ball and the chip surface [Fig. 1.1 (b)], which is known to be solid - state - bonding process [13]. Next, the capillary is moved to the location on the substrate to which the chip needs

to be wired [Fig. 1.1 (c)]. The capillary again descends to the substrate surface. The wire is welded with a combination of heat, force, and ultrasonic energy, but without ball formation [Fig. 1.1 (d)]. This is called the crescent bond (or wedge bond, stitch bond, 2nd bond). In the final step, the capillary moves up to the preset height and tears the wire with clamp closed to form another tail, leading to another EFO [Fig. 1.1 (e)].

As the semiconductor industry moves to shrinking die and pad pitch and 3-D packaging solutions to meet the demands of lower cost, higher number of I/O interconnection, and more miniaturization for electronic devices, new and disruptive technologies need to meet the many

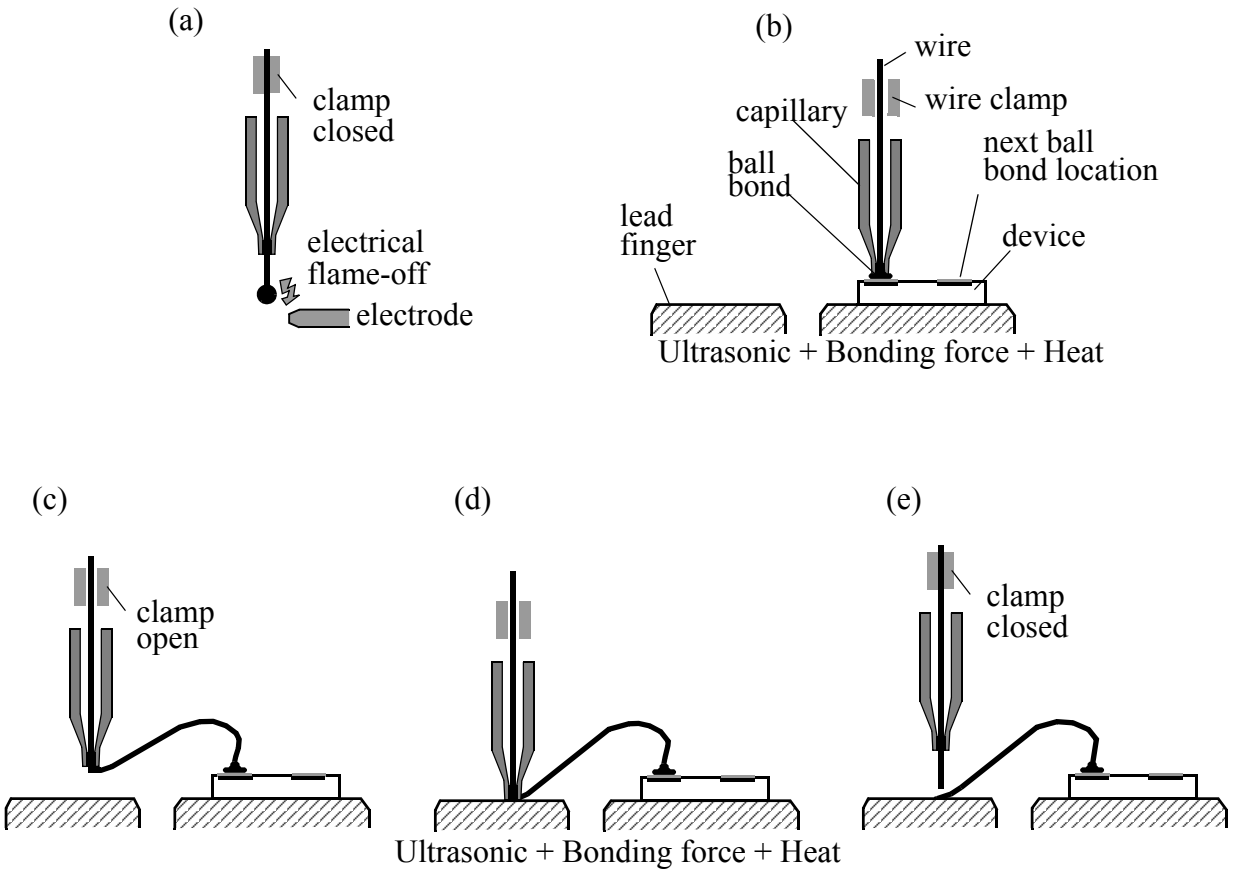

Fig. 1.1 Schematics of ball bonding process sequence.

challenges [14, 15]. In wire bonding materials, Cu and insulated Au wires instead of conventional bare Au wire are emerging in fine pitch thermosonic wire bonding.

The benefits of using Cu and insulated Au wire instead of bare Au wire in wire bonding processes are as follows. The Cu wire to Al pad bonding system (Cu/Al bonds) can have longer thermal life - time than Au/Al bonds [16]. Thinner diameter Cu wire can be used to obtain the same electrical properties compared to thicker Au wire due to the lower electrical resistivity [4]. Higher wire tensile strength and stiffness of Cu compared to Au can improve the wire sweep property [5].

The insulating capability of insulated Au wire improves the flexibility of wire bond design as the wires can touch each other without impairing the device specifications [17]. Longer wires, sagging wires, crossing wires, lower loops, wire sway, and wire sweep are no longer roadblocks to production and can be acceptable if insulated wire is used.

1.3.1 Crescent Bonding Process

Crescent and tail bonds which are separated by capillary geometry are formed as illustrated in Fig. 1.2. Figure 1.3 shows a scanning electron microscope (SEM) image of the crescent bond and the tail bond of a Au wire on a Au substrate. Challenges in wire bonding include reduction in bond pad pitch and wire size, high pin count with more than 1500 wires. A small diameter of wires causes poor crescent and tail bond quality, resulting from inconsistent pad plating thickness, surface roughness, and hardness [18].

The sequence of the crescent bond process is shown in Figs. 1.4 (a) - (f). After the ball bonding process, the capillary moves to the crescent bond position along the looping trajectory. The capillary touches down on the substrate [Fig. 1.4 (a)] and the wire is deformed between the capillary and the substrate by impact force [Fig. 1.4 (b)]. Ultrasonic oscillation together with nor-

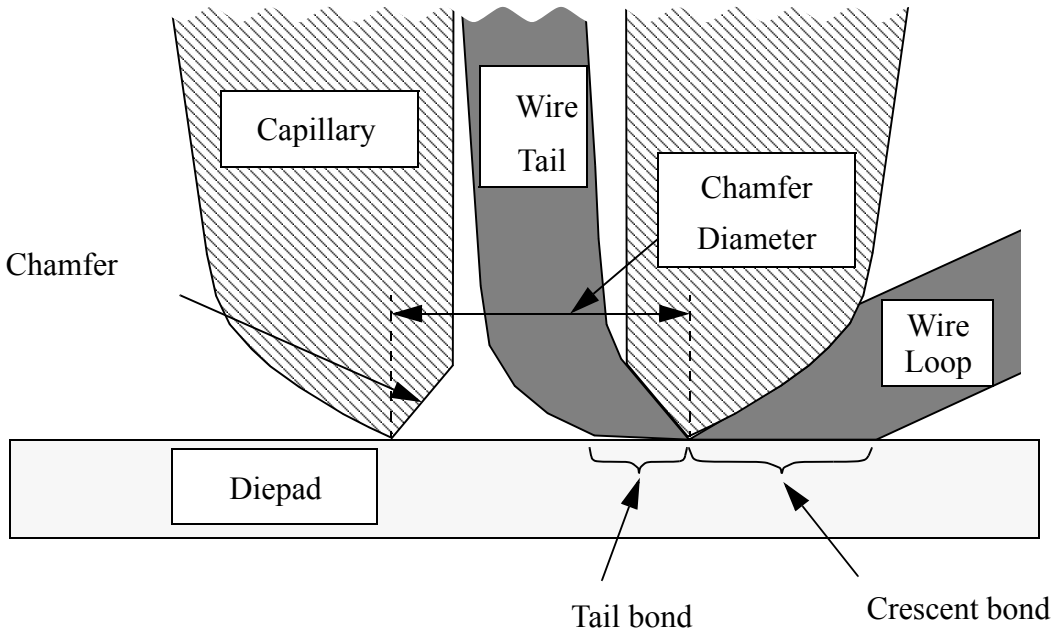

Fig. 1.2 Illustration of a cross-section of the crescent bond and the tail bond.

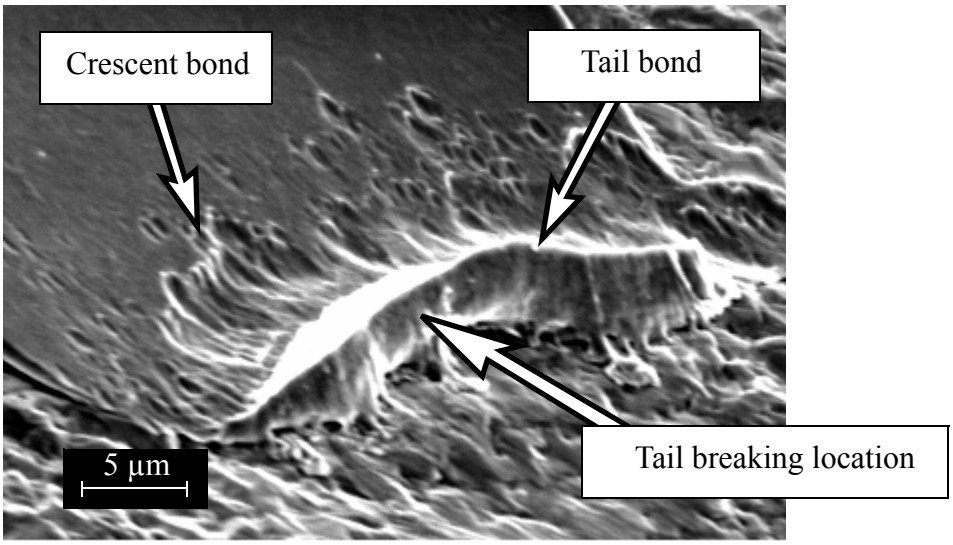

Fig. 1.3 SEM image showing the crescent bond.

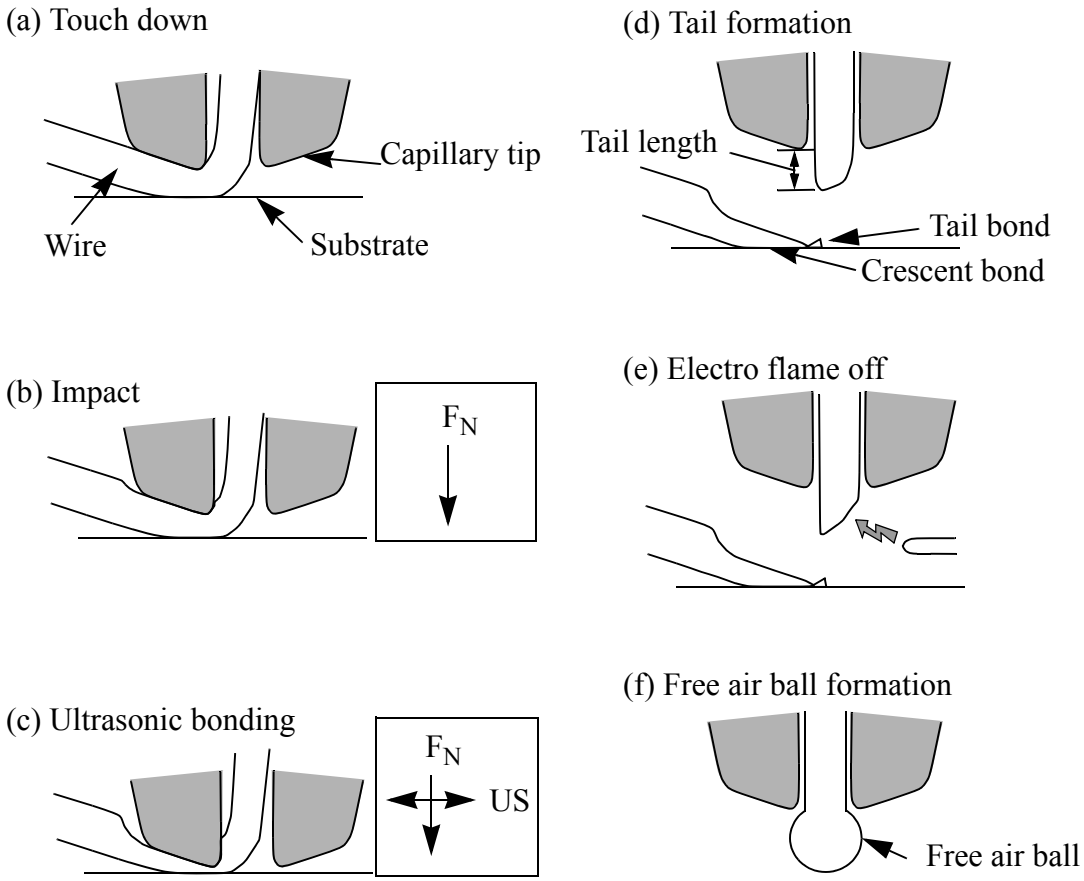

Fig. 1.4 Wedge bonding and EFO sequence.

mal bonding force are applied to enhance the bond growth [Fig. 1.4 (c)]. The capillary moves up to the predetermined height and stops to produce the wire tail. The wire clamp above the capillary is closed and the capillary moves further up to break the wire [Fig. 1.4 (d)], resulting in formation of the wire tail. The wire tail is required to form a free air ball (FAB) with EFO. The FAB is used for the subsequent ball bond [Figs. 1.4 (e) and (f)].

Crescent bond quality is influenced by input machine parameters (factors) such as impact force, ulstrasonic energy, bonding force, time, heater temperature and by substrate metallization characteristics, such as cleanness, roughness, hardness, and microstructure. Figure 1.5 illustrates the machine parameter values versus time applied during crescent bonding. The impact of the wire on the substrates or leadframes during crescent bonding produces high force, resulting in strong initial deformation of the wire. A bonding force lower than the impact force produce friction with ultrasound between the wire and the substrates. The friction energy can remove the native copper oxide and the insulation layer on the gold wire, followed by metallic bonding. A constant ac voltage is applied to a transducer as shown in Fig. 1.6 to produce the ultrasonic vibra-

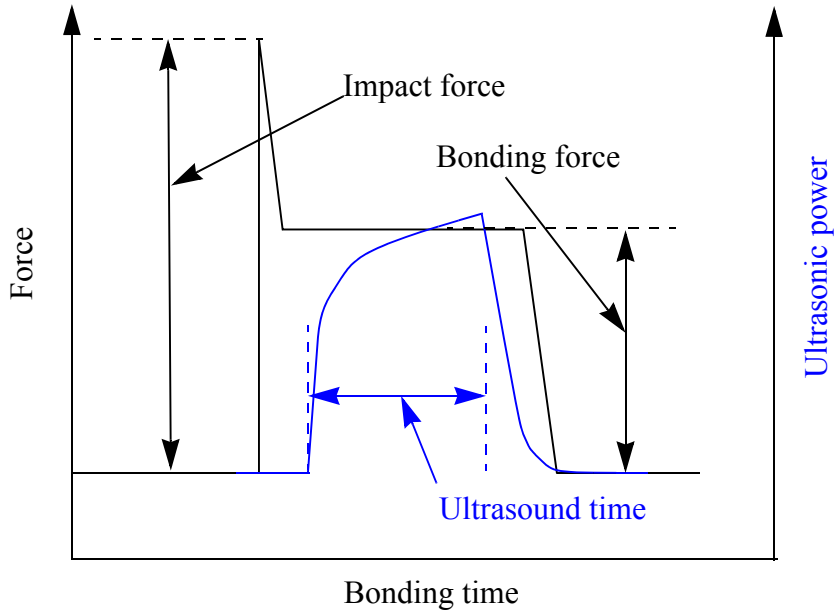

Fig. 1.5 Illustration of machine parameters applied during crescent bonding.

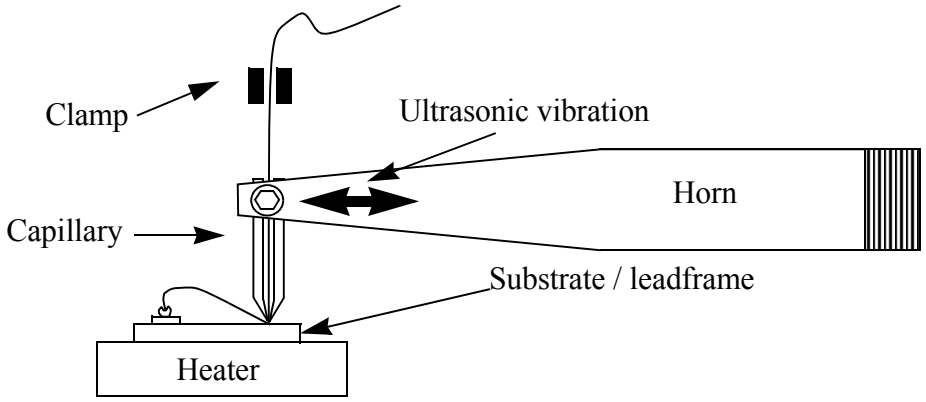

Fig. 1.6 Illustration setup for thermosonic crescent bonding.

tions. An elevated temperature on the chip reduces the impurity and oxidation levels of the Ag substrate surface, increasing the bond quality and the stability of the process.

1.3.2 Tail Bonding Process

Stable tail bond formation plays an important role in stability of the thermosonic wire bonding process. When new bonding wires are applied in fine pitch application the premature termination of the tail bond which is called short tailing, wire open, or EFO open is frequently encountered. However, there is a lack of understanding of how the tail bond forms. Therefore, Improved understanding of tail bond formation is necessary. In this chapter, an overview of tail bonding is discussed.

An illustration of the tail breaking process is given in Figs. 1.7 (a) and (b). The capillary has stopped at the tail height as shown in Fig. 1.7 (a). The clamp closes and the horn moves up to

break the wire. A typical wire residue left from tail bond and break is shown in Fig. 1.7 (b). Tail bonds should be strong enough to hold the wire before the clamp closes. After crescent bonding, the capillary moves up to the tail height where it remains until the clamp closes. It then starts pulling the wire to break it, resulting in a tail of a predefined length. The tail bond which is formed together with the crescent bond should be strong enough to sustain the formation of the wire tail. The wire tail is melted by the EFO and solidified, resulting in uniform FAB formation. However, if the tail bond is weak, it can lead to non uniform tail length and therefore non uniform free air ball (FAB) formation.

Sometimes, the bonder stops before flaming off the tail because the tail bond was weak enough to loose from the substrate before the clamp could close, resulting in the wire being blown out from the capillary. The frequent occurrence of such process stoppage requires a high operator effort and reduces the throughput of the wire bond production.

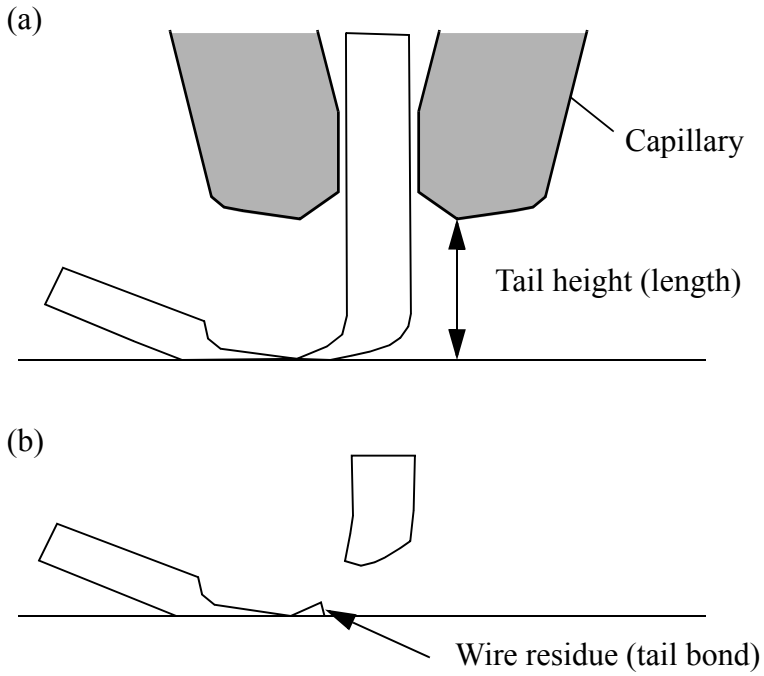

Fig. 1.7 Illustration of the tail breaking process.

1.4 Quality Assessment

1.4.1 Wire Deformation and Pull Test

The crescent bond quality is determined by the wire deformation and wire pull force measurements [19, 20, 21]. The definition of a bonded wire deformation measurement is shown in Figs. 1.8. A typical allowed bonded wire deformation is about 1.5 - 2 times the diameter of the wire [19], usually measured using an optical microscope. The wire pull force values are obtained with a pull tester as shown in Fig. 1.9. The pull hook placed under the wire loop breaks the wire by a vertical motion, and simultaneously measures the force needed. The pull test is standardized in [20]. The minimum pull force (PF) required for a 25μm wire diameter is 3 gf (1 gf = 9.8 mN). The pull force value is dependent on the location of the hook. The hook is placed at 30% away from the crescent bond as shown in Fig. 1.9. For sufficient strong crescent bond, the wire breaks at the heel of the crescent bond.

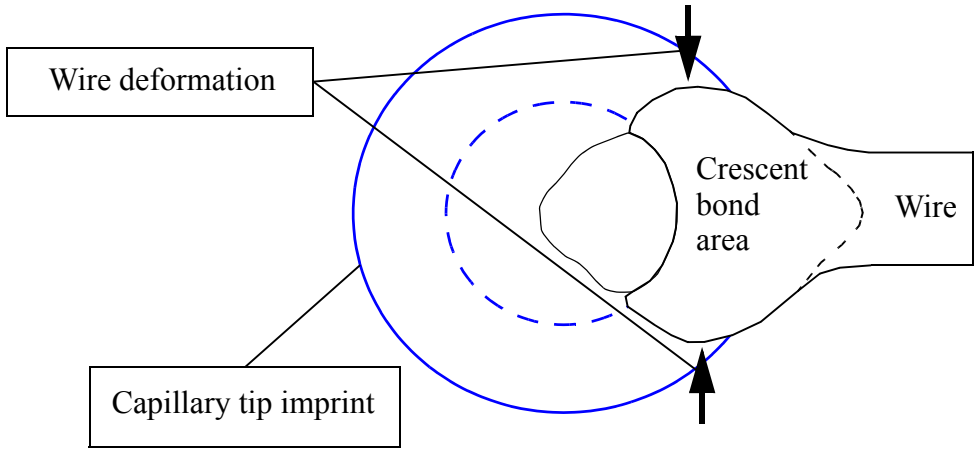

Fig. 1.8 Illustration of example crescent bond:location of deformation measurement.

The process capability index (cpk) [22] is an indication of the ability of a process to produce output within specification limits. For the present application, it is defined by Eqn (1. 1)

$$cpk = \frac{\mu - LSL}{3\sigma} \tag{1. 1}$$

where μ is the average, LSL is the lower specification limit of the PF, and σ is the standard deviation. Values of cpk are determined for PF using LSL_{PF} = 24 mN, a limit determined using a standard limit for Au wire bonds and assuming the maximum angle between wire loop and sub-strate during pulling is about 60° [21].

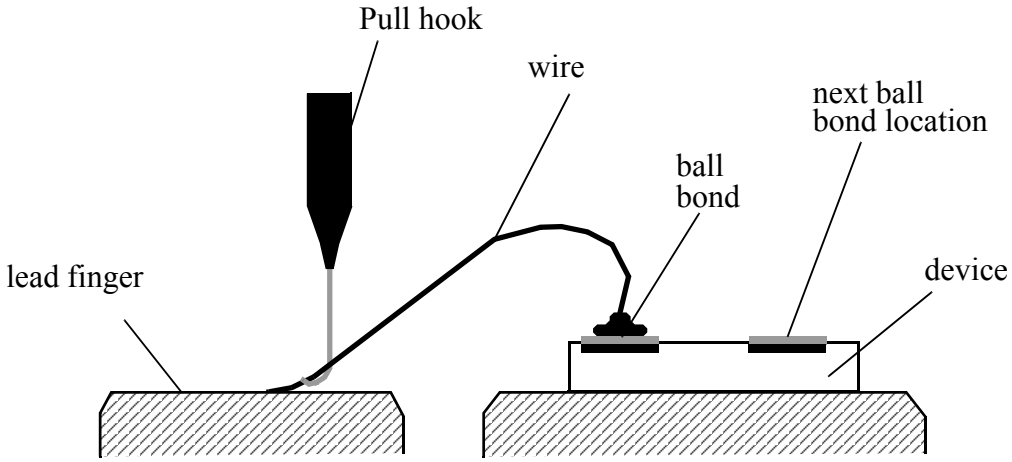

Fig. 1.9 Schematics of destructive wire pull test for crescent bond strength measurement.

1.4.2 Tail Breaking Force Measurement

Although the evaluation of the tail bond strength (tail breaking force) becomes more important, there is no standardized method to evaluate the strength of tail bond. Bonding process stoppage with short tail becomes a major challenge. In this thesis, an online method to measure the strength of the tail bond with a proximity sensor is developed and discussed in Chapter 2.

1.5 Proposed Bonding Mechanisms

Ultrasonic crescent bonding (or wedge, stitch bonding) is generally accepted to be a solid state bonding process. Evidence for this conclusion includes the bonds made in liquid nitrogen [13], thermocouple measurement at the bond interface [23] and bond interface study by transmission electron microscopy [24]. Contamination free surface is a primary requirement to form metallurgical bond. Plasma cleaning [25] of the chip and substrate/leadframe can help remove contaminants attached on the chip and substrate, resulting in increasing the crescent bond quality.

A number of studies have tried to understand the mechanism of crescent bond formation [26, 27, 28]. Harman and Alberts [26] studied the wedge -wedge bonding mechanism by studying the bond imprint after wire is lifted - off. They examined Al - Al and Au - Au systems with variation of bonding time. The substrate is flattened due to the force of the bonding tool impacting against the wire (zero bonding time). As ultrasonic friction is applied bond formation always begins around the perimeter of the bond imprint and then grows inward from the perimeter to essentially cover the entire wire - substrate interface. The crescent bond imprint study in the variation of ultrasound (US) by Zhou *et al* [28] reported that crescent bond forms at the ends of the long axis of the bond, and grows along the periphery and to the center as US increases. Therefore, it can be summarized that the crescent bond first forms at the periphery and then grows inward to the center of the bond as illustrated in Fig. 1.10 which is modified from [27].

Lum *et al* [29] reported a transition of bonding mechanism from microslip to gross sliding with an increase of US. This transition is shifted with an increase of bonding force (BF). The cleansing of the material surface is a requirement for metallic bonding which is accomplished by microslip and gross sliding phenomena causing wear of the oxide layer.

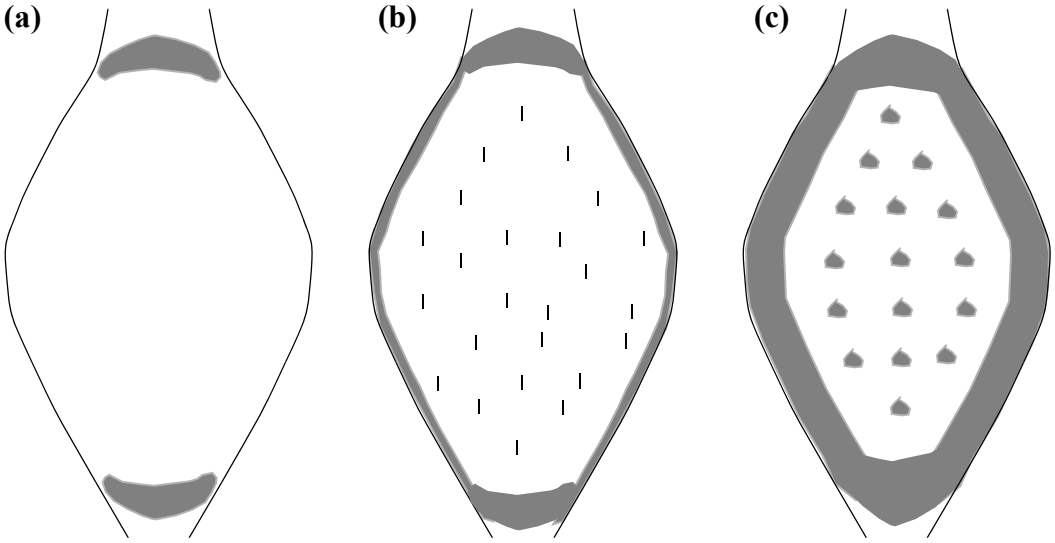

Fig. 1.10 Modified schematic from [28] showing the initiation and growth of the bonded regions as ultrasonic energy is increased. (a) bonding initiation at the ends of the long axis of the bond, (b) bonding along the periphery of the bond, and (c) growth of the bonded regions toward the center.

1.6 Effects of Ultrasound on Metals

In the crescent bonding process, ultrasonic deformation of the wire plays a vital role on the bond quality [30]. As ultrasonic power (here, ultrasound) increases the crescent bond grows, but wire itself degrades as shown in Fig. 1.11.

Langenecker [31] reported that acoustic softening takes place immediately when a metal is subjected to ultrasonic irradiation, and therefore results in easy deformation of the metals. However, applying ultrasound with sufficiently high stress amplitude acoustic hardening of the metals occurs. Hayes and Shyne [32] found that intense acoustic oscillations caused a large increase in recrystalization kinetics of copper by a factor of 100 and decrease of the activation energy for recrystallization up to 46%.

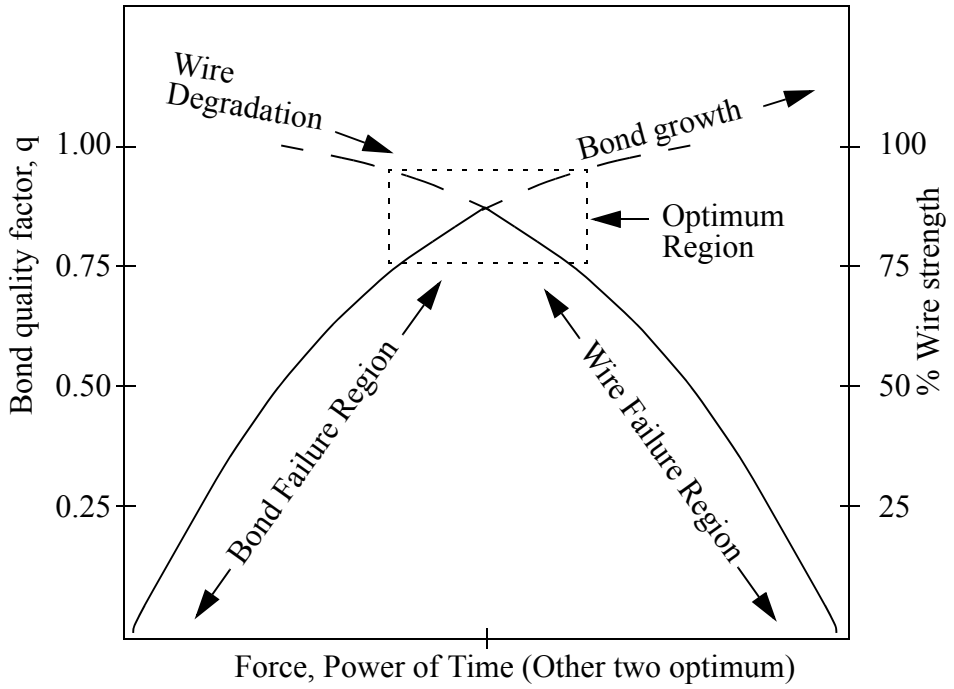

Fig. 1.11 Representation of the competing processes during ultrasonic bonding of a wire to a plat substrate. The graph is modified from [30].

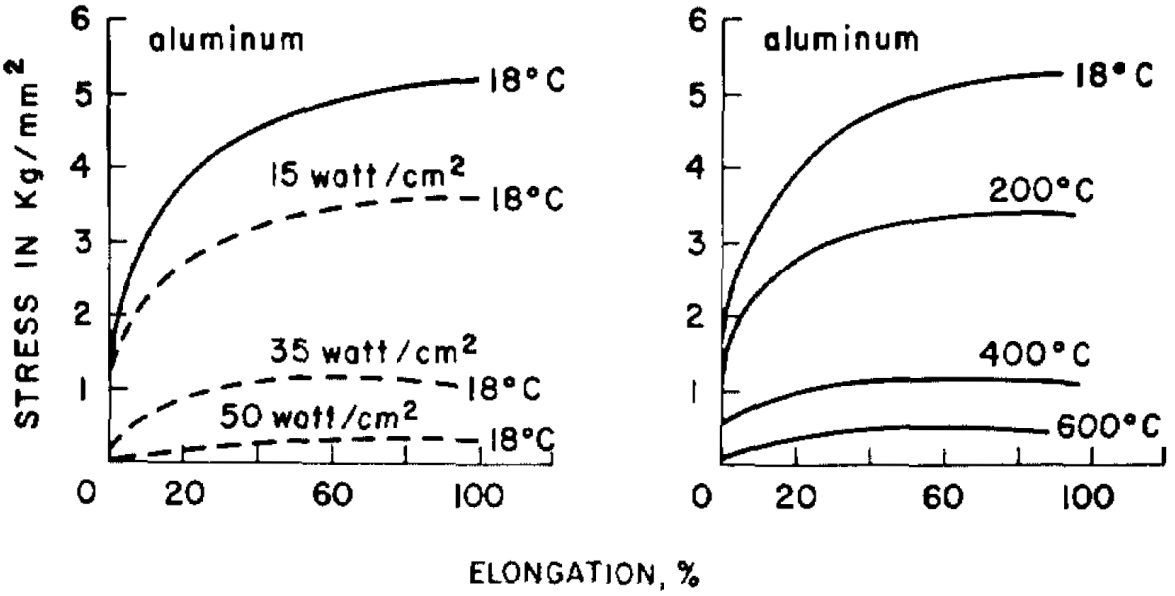

Fig. 1.12 Stress vs. elongation for aluminum single crystals; dashed curves indicate straining during ultrasonic irradiation at 20kc/s and solid curves indicate no irradiation [31].

Ultrasound and heat have similar effects on the softening of metals as shown in Fig. 1.12 [31]. However, the softening by ultrasound proceeds much more efficiently than that by heat because preferential absorption of energy takes place at dislocation or grain boundaries, unlike heat where the whole region requires thermal energy.

1.7 Recent Studies of Tail Bonding

Brunner [34] developed a tail bond strength measurement method in 1999 using a wire bonder software patch. A PC hyperterminal can measure the tensile force to break the tail bond This method was applied to study the behavior of tail bond formation with Au and Cu wires on different substrate materials [5]. It is found that the major influence of larger variation of Cu wire tail - pull force compared to that of Au wire is hypothesized as due to non - uniformity of Cu wire deformation due to a relatively large and randomized grain structure left by the annealing process. A high strain rate sensitivity and strong tendency for Cu to work-harden may accentuate the effect.

The tail breaking force (TBF) measurement using microsensors in the Au - Au system by Schwizer [36] reported that the variation of the TBF is smaller than that of crescent bond pull force. With US transducer current higher than 51 mA, TBF does not depend on impact force and wire loop direction. The tail bond formation in Au - Au system is very stable, resulting in consistent FAB formation. However, knowledge on tail bond formation when new bonding wires (Cu and insulated Au wire) are used is limited. Furthermore, there is still lack of quantitative studies describing how tail bond process characteristics depends on the input parameters, wire materials and how tail formation influence the ball bonding process.

1.8 Material Issues in Wire Bonding

Demands for cost reduction and continuing improvement in device density and performance are driving advances in microelectronic packaging technology. Cu and insulated Au bonding wires, and underlying dielectrics with low dielectric constant (k) are developed to replace conventional Au wire and silicon dioxide (SiO_2), respectively. This chapter provides an overview on issues of those new materials for wire bonding process and introduces the topics addressed in this thesis.

1.8.1 Cu Bonding Wire

Increasing demands for improved reliability, finer pitch interconnection [37], and cost reduction of IC packages encourage the wire bonding industry to implement Cu wire in the wire bonding process. The Cu wire to Al pad bonding system (Cu/Al bonds) can have a four times longer life time than Au/Al bonds [38]. Thinner diameter Cu wire can be used to obtain the same electrical properties compared to thicker Au wire due to the lower electrical resistivity [4] and higher wire tensile strength and stiffness of Cu [5].

The advantages of Cu wire bonding are offset by several drawbacks. Easy oxidation, high hardness, and strain hardening of Cu [39] reduce the quality and robustness of the crescent bond (2nd bond or stitch bond) and the tail bond which can lead to non-uniform free air ball (FAB) formation [40]. The tail bond should be strong enough to hold the wire after crescent bonding until the clamp closes so that the preset tail length is obtained. If the tail bond is too weak, it breaks

before the clamps close, resulting in EFO open or short tails responsible for frequent production stoppage encountered when applying Cu wire for fine pitch application [5]. Easy oxidation [4, 41], high hardness [3], coarse microstructure [42], and strain hardening of Cu wire [39] reduce the quality and robustness of the crescent bond and the tail bond which can lead to non-uniform free air ball (FAB) formation. Wedge bond [18] and wedge bond tailing [5] of fine and ultra fine pitch processes are severely unstable which is caused by the decrease of capillary tip diameter, leading to decrease in the size of wedge and tail bonds.

1.8.2 Insulated Au Bonding Wire

Wire loop span up to 6 mm is demanded for advanced applications such as stacked die packages [43]. The wire bond pitches for ball and wedge will be reduced to as low as 25 and 20 μm, respectively, in 2009 [37]. The major challenges of fine pitch and stacked die packaging are to reduce the wire sweep, which causes wire crossover and shorting. Fig. 1.13, shows an illustration of wire looping in a BGA package. During the molding process, molding compound flows from one side of the package to the other side. The flow causes the wire sweep as defined in Fig. 1.14. In extreme case, the wire sweep results in neighboring wire touching each other, causing short circuits. Hence, the looping capability of bonding wires is challenged in today's advanced packages.

A number of studies have been performed to improve wire deformation during the molding process. They can be categorized to three approaches in order to deal with wire sweep. The first approach is to improve the mechanical stability of the wire loops. It is found that wire sweep

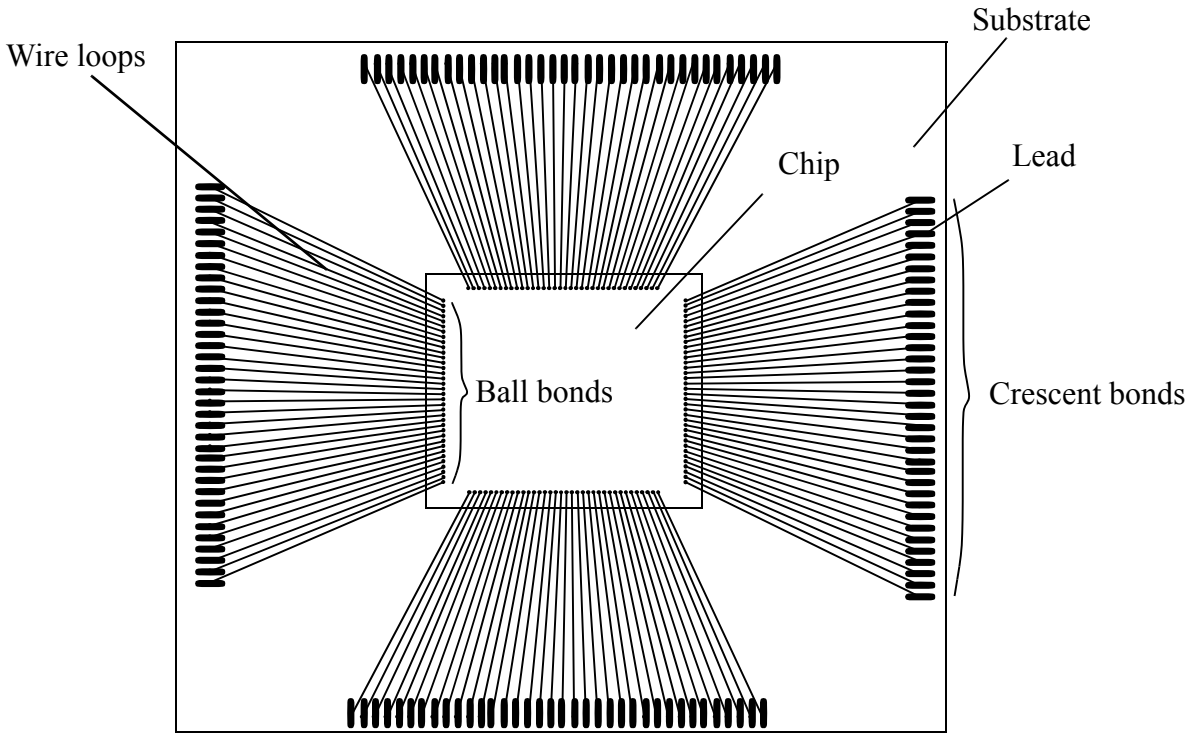

Fig. 1.13 Schematics of wire bonded package.

depends on wire diameter [44], wire span length [45] and profile [46], bond height, and mechanical properties of wire [47]. The second approach is focused on the molding process. Optimum molding processes, materials, and parameters are required [48, 49].

The third approach uses insulated bonding wires [17, 50]. Insulated bonding wire such as X - Wire^{TM} by Microbonds Inc. Markham, Canada, is a disruptive technology that is gaining more and more momentum. An insulation layer (thickness: 100 ~ 250 nm) is deposited on bare Au wire in order to prevent a wire loop from shorting with neighboring wire loops, offering improved flexibility in wire looping profile as shown in Fig. 1.15 which is a scanning electron microscope (SEM) image of a wire bonded sample using crossing wire configuration. However, due to the insulation layer deposited, the crescent bonding behavior of such wire is different from that of bare Au wire.

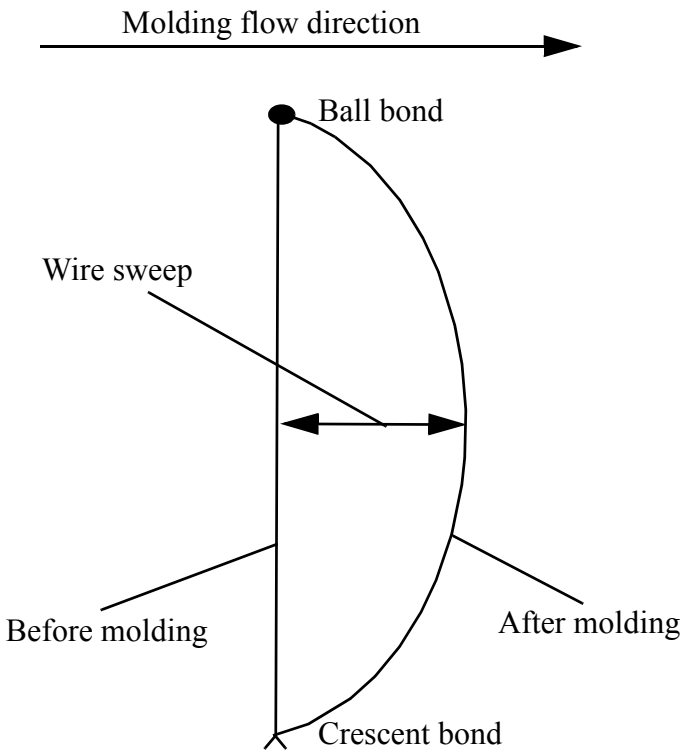

Fig. 1.14 Schematics of wire loop change before and after molding process.

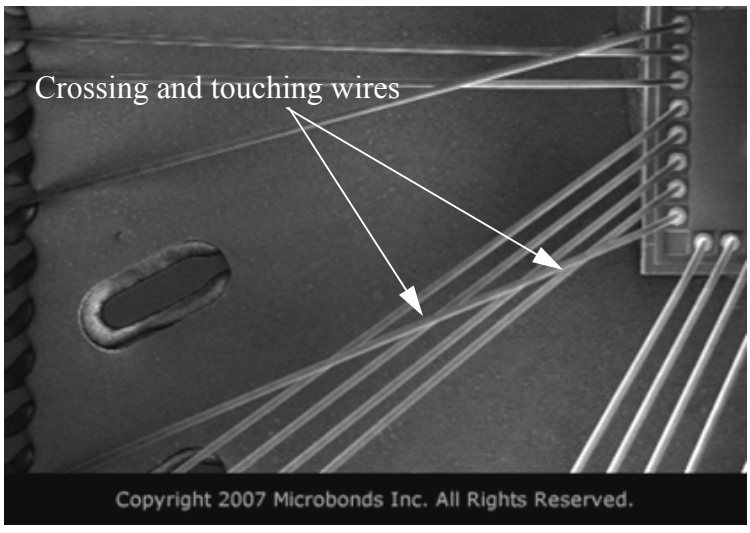

Fig. 1.15 SEM image of an advanced looping (crossing wire) using insulated Au wire.

1.8.3 Low Dielectric Constant (*k*) Materials

As the spacing of the interconnect lines on the CMOS chip decreases, the associated higher resistance and capacitive coupling causes an increasing signal delay, known as RC delay, of the circuit. Lowering the *k* value of the dielectric decreases the RC delay and lowers power consumption [51]. In order to achieve a *k* value lower than 2.5, porosity is required inside the dielectric material. Table 1 summarizes low - k materials used for microelectronics interconnections [52]. The porosities reduce the mechanical strength and cause poor adhesion, resulting in easy chip damage and cratering during wire bonding.

Wire bonding produces mechanical stress on the bond pad which creates chip damage effects such as pad peeling, cratering, or dielectric layer delamination as shown in Figs. 1.16 (a), (b), (c), respectively. These defects are often observed when copper wire and low - k materials [53] are implemented in wire bonding. Cracks frequently are not visible and the bond still may

Table 1. 1: Low - *k* materials for microelectronics interconnections. [52]

Dielectrics	Dielectric constant (k)	Modulus (Gpa)	Hardness (Gpa)	Stress (Mpa)
FSG	3.4 - 4.1	72	7.5	100
Black Diamond	2.7	7.76	0.13 - 3.6	-
SiLK	2.6	2.5 - 4.2	0.2 - 0.28	90
TEOS (SiO_2)	3.2 - 4.1	72 - 100	9.5	-
Porous SiLK	2.0	1.5 - 3.0	0.16 - 0.19	54
SiO_2	4.1	72	7.5	100

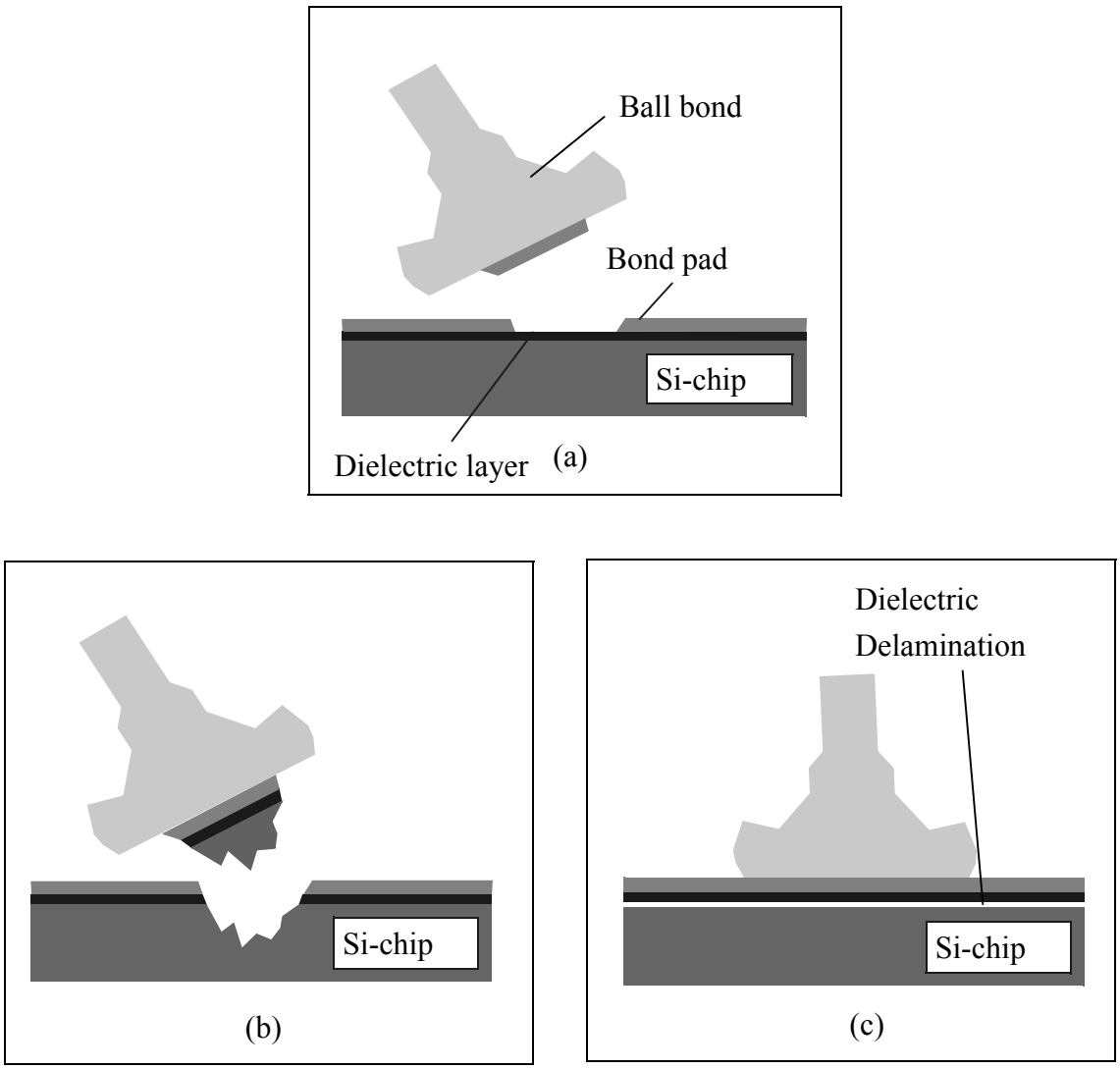

Fig. 1.16 Illustrations of wire bonding related defects. (a) pad peeling. (b) cratering. (c) dielectric layer delamination.

have good electrical performance [54] in the beginning of the chip life, which makes detection of such failures difficult.

Cu is harder than Au which increases the possibility of silicon cratering [55] as Cu needs higher ultrasound and bonding force for strong bonds. Harder and thicker bond pad metallization helps to reduce the cratering [55, 56]. The ultrasound [57] and bonding force [58] parameters

have great influences on cratering which is seldom encountered in ultrasound free thermocompression bonding [21]. Finite element analysis [59, 57] shows that stress concentration is high at the periphery of the bonded ball, where chip damage occurs. There is still lack of understanding of the chip damage effects occurring in the wire bonding process. Factors which can contribute to crating are summarized in Fig. 1.17. So far, suggestions reported to eliminate the chip damage include optimizing bonding parameters [61], or inserting structural reinforcement of dielectrics [62].

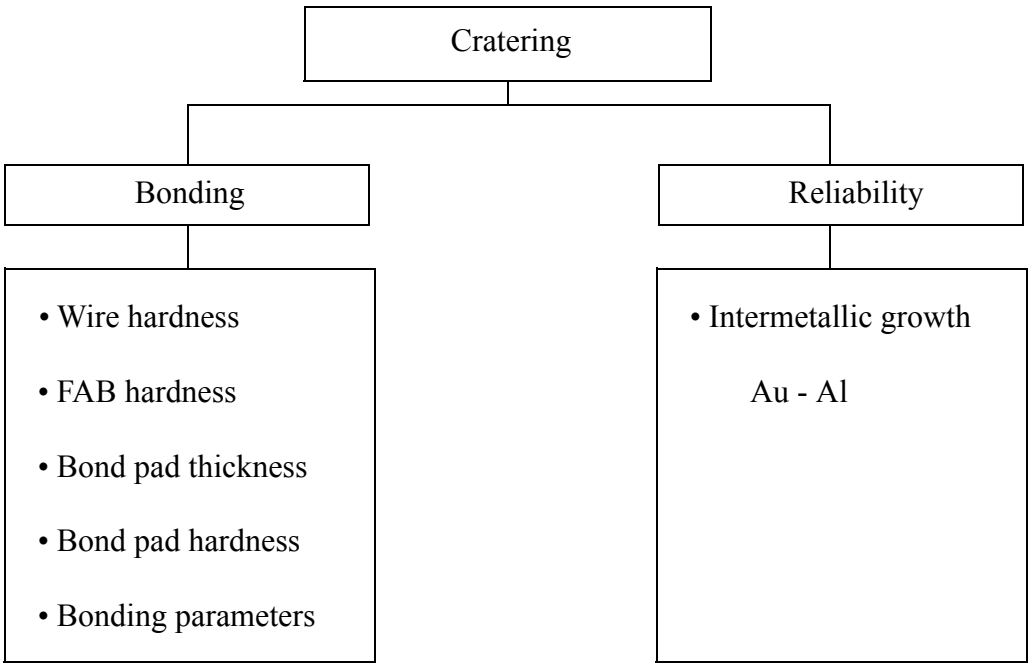

Fig. 1.17 Summary of the causes of cratering.

Chapter 2 Online Tail Breaking Force Measurement

Tail bond weakness can result in non uniform tail length and therefore non uniform free air ball (FAB) formation. Sometimes, the bonder stops before EFO process because the tail bond was weak enough to break and loose before the clamp could close, resulting in the wire being blown out from the capillary.

The frequent occurrence of such process stops reduces the throughput of the wire bond production. Even though the importance of the tail bond is increasing, unfortunately, there is no standardized method to measure the tail bond strength. The present study is undertaken to contribute to the understanding of the tail bond with a method to measure the tail bond strength during thermosonic crescent bonding process. Here, an online method for measuring tail bond strength is developed using a proximity sensor which is discussed in Chapter 2.1. The calibration of the method, process optimization by iteration, and preliminary optimization using this method are demonstrated in Chapters 2.2, 2.3 and 2.4, respectively. The influence of plasma cleaning on the tail bond strength is evaluated in Chapter 2.5.

2.1 Measurement Method Development with Proximity Sensor

A wire bonder used in this work is an ESEC 3100 auto ball bonder as produced by Oerlikon Esec, Cham, Switzerland as shown in Fig. 2.1. This is a fully automated bonder which is controlled by window based software. It performs bonding using a bonding program and without operater intervention unless a problem arises. The bonding programs include bond position, material handling, and bonding parameters. In order to use Cu wire, this wire bonder is equipped with copper kit which can provide shielding gas, usually 5 %H_2 + 95 %N_2, on the FAB formation region in order to protect the FAB from oxidation as shown in Fig. 2.2.

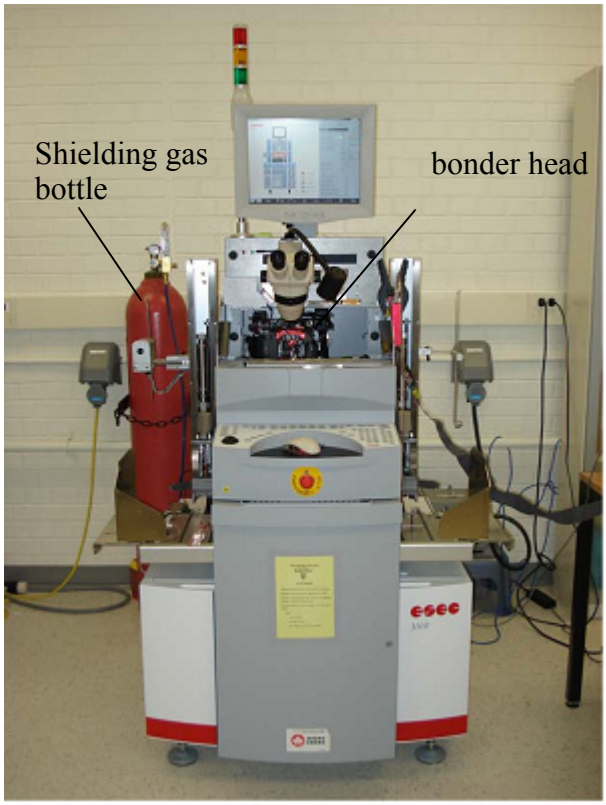

Fig. 2.1 Photograph of ESEC 3100 auto ball bonder.

A 99.99 % purity 25 μm diameter Cu and insulated Au wires from MK Electron Co. Ltd., Yongin, Korea, and Microbonds Inc. Markham, Canada, respectively, are used for bonding. A 99.99 % purity 25 μm diameter Au wire, from MK Electron Co. Ltd., Yongin, Korea, is used as a reference wire.

The capillary used is made of Zirconia composite material with a Matte finish. It has tool length (TL) and diameter (TD) of 11.10 mm/.437" and 1.587 mm/.0625", respectively as illustrated in Fig. 2.3 (a).The hole (H), tip diameter (T), chamfer diameter (CD), face angle (FA), and chamfer angle (CA) are 35 μm, 100 μm and 51 μm, 11^{o}, 90^{o}, respectively, as shown in Fig. 2.3 (b). This capillary also has bottle neck configuration for fine pitch wire bonding.

The bonding material used in this study is commercial PLCC44 leadframe strips with a metallization which is 8 μm thick Ag as shown in Figs. 2.4 (a) and (b). One strip is made of seven leaframes. Bonds are made on the diepad in the middle of the leadframe as shown in Fig. 2.4 (a). In order to keep the cleanness of the substrate/leadframe, fresh substrates stored in N_2 environ-

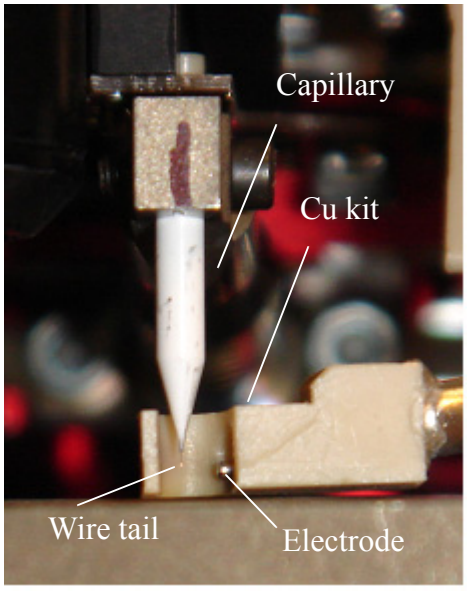

Fig. 2.2 Photograph of copper kit.

ment (storage box with N_2) are used in this study. Tail breaking forces are measured on two die-pad randomly selected from each strip. More than 5 strips are used for randomization to minimize any substrate related effect.

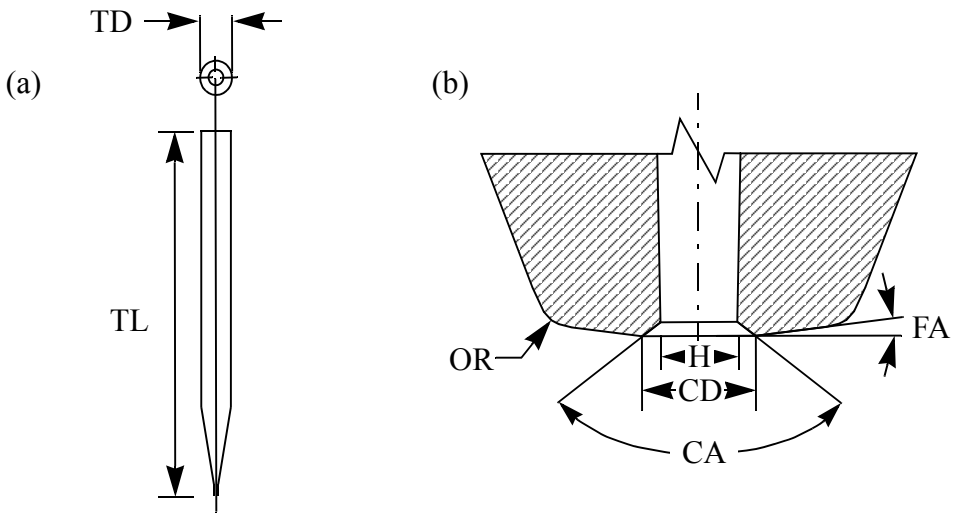

Fig. 2.3 Illustration of (a) capillary and (b) its tip detail.

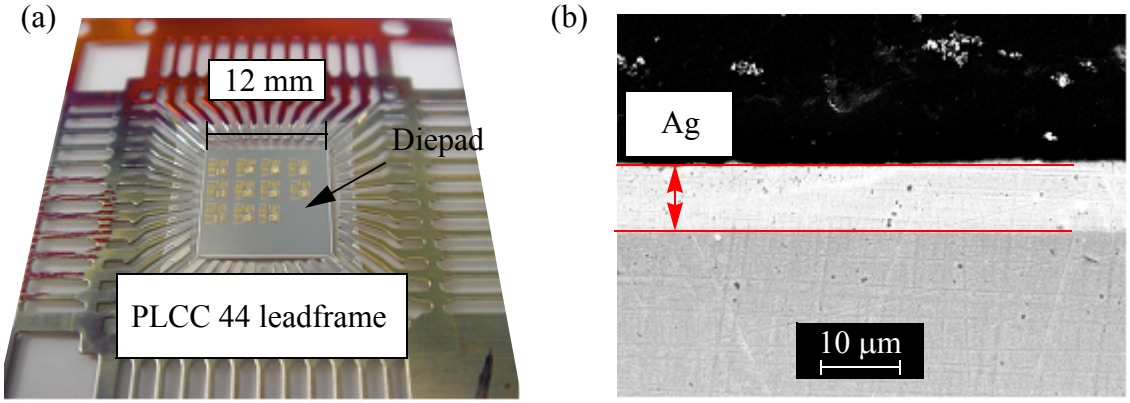

Fig. 2.4 Substrate material (a) PLCC 44 Ag metallized leadframe used as bonding material and (b) cross - section of diepad.

2.1.1 Measurement Principle

A proximity sensor is attached on the clamp to measure real-time signals corresponding to the gap between clamp and horn as shown in Fig. 2.5. The proximity sensor is a displacement sensor which works on the Eddy current principle to sense the proximity of conductive materials. The displacement measured is proportional to the force acting on the horn. Right after the crescent bonding, the capillary moves up to a certain height. The clamp closes and moves further in the z - direction in order to break the wire, resulting in the wire dragging the clamp. This reduces the gap between clamp and horn as illustrated in Fig. 2.6.

The parameters that control the breaking of the wire ("tailing") after the second bond are set to 200 μm and 2 μm/ms of z tear distance and speed, respectively. The selected speed is slow

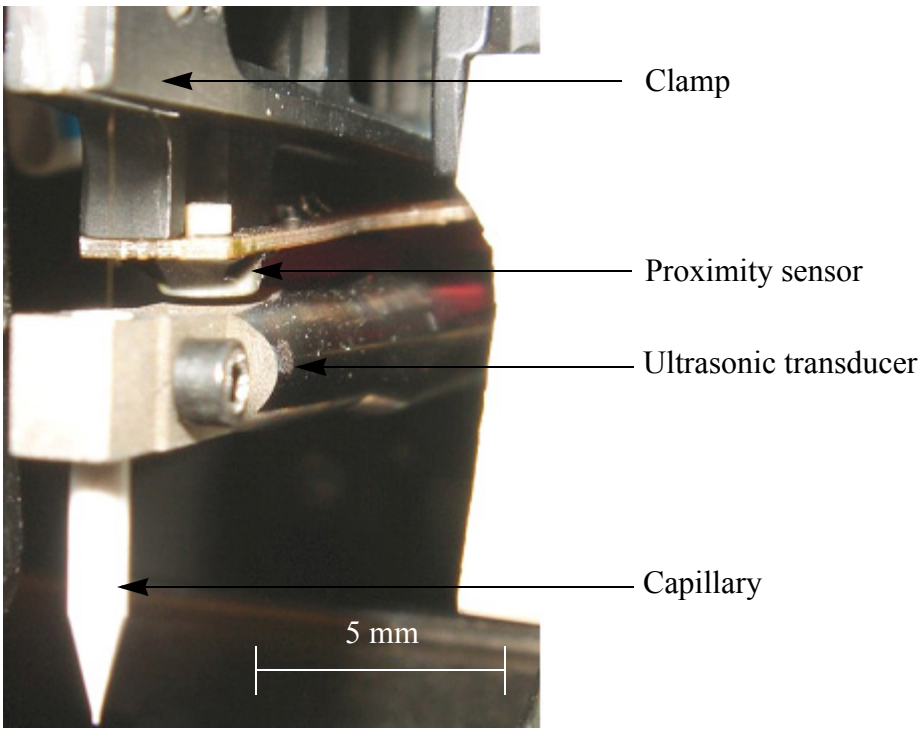

Fig. 2.5 Proximity sensor, wire clamp, ultrasonic transducer, and capillary.

enough to time-resolve the tail breaking signal. Figure 2.7 shows examples of signals measured with the proximity sensor. The process parameters, impact force (IF) and bonding force (BF) for the ball bond, are 600 mN, 200 mN, respectively and for wedge bond are 1000 mN and 800 mN, respectively. The IF parameter is similar to the contact velocity (CV) parameter available on other wire bonder types. The proximity sensor signal correspond to bond force when the capillary presses on a surface causing the horn to deform slightly. This bond force signal is calibrated before the wire bonder is delivered.

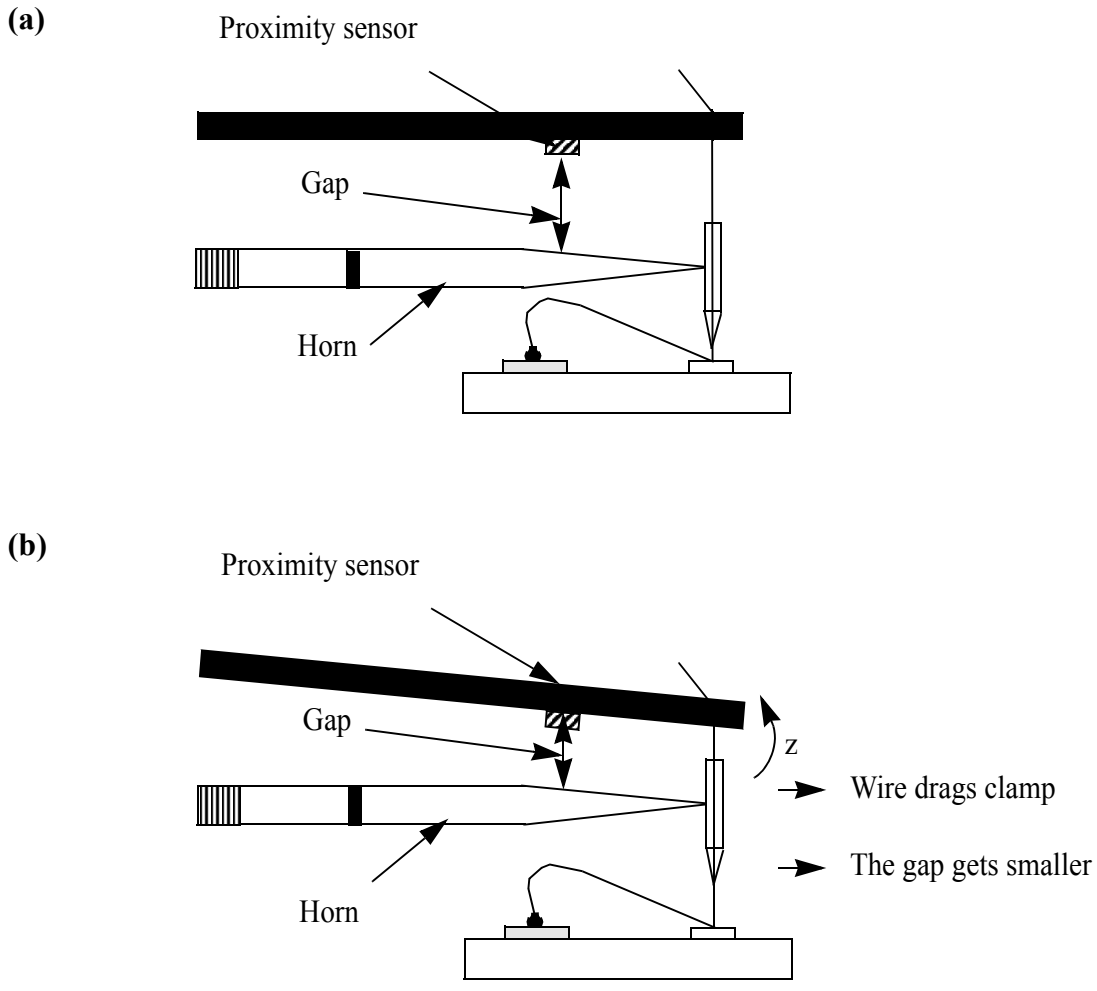

Fig. 2.6 Schematics for principle of tail breaking force (TBF) measurement. (a) Clamp position prior to tail breaking and (b) clamp position during tail breaking.

The tail breaking portion of the signal is indicated in Fig. 2.8. The bond force calibration is not valid for tail breaking force. Therefore, dedicated calibration is carried out for the tail breaking force and discussed in section 2.2. It is enlarged and shown in Fig. 2.9. The signal increases before the tail breaks as the wire tension increases. After it reaches a maximum value, the signal suddenly drops to zero indicating tail breaking. If the signal is measured without the wire, no

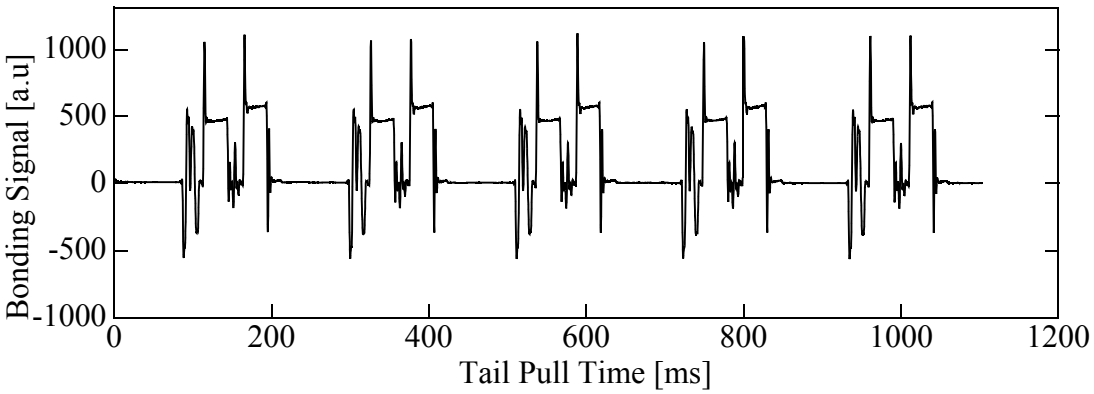

Fig. 2.7 Signals measured with proximity sensor during bonding process.

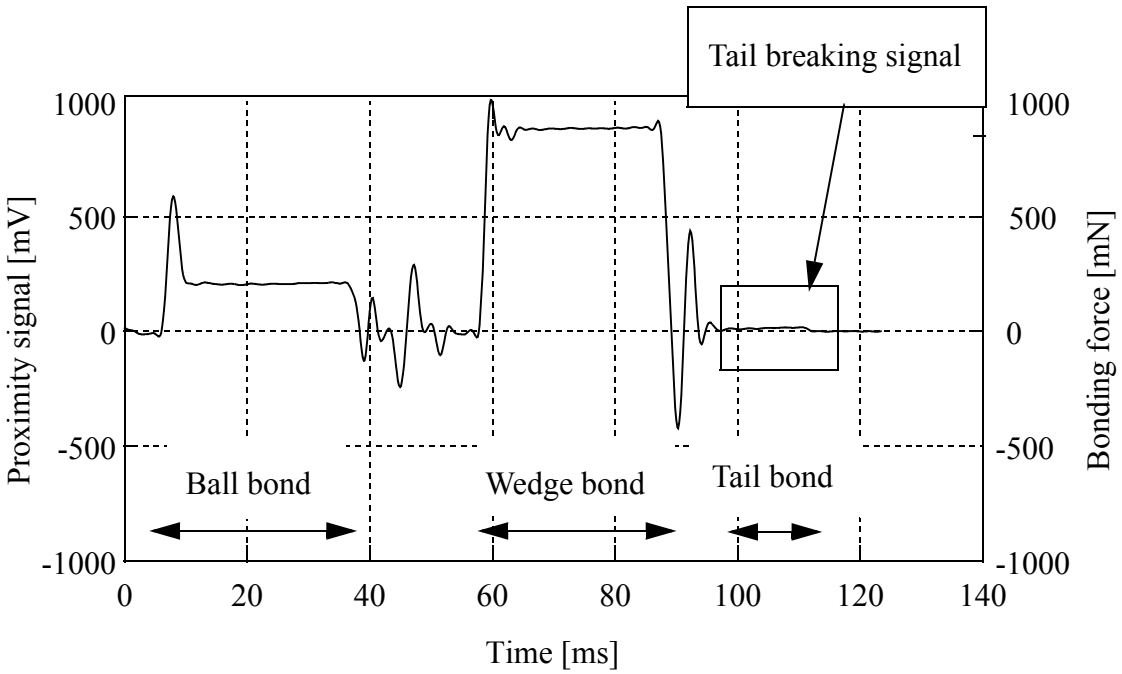

Fig. 2.8 Proximity sensor signal during one bond cycle.

change is observed in this period. In the measurement with the wire, the time point of the tail break indicated by (c) in Fig. 2.9 is found automatically by using an evaluation software that locates the time of the strongest decay (minimum derivative) of the signal. Two portions of the signals are averaged, the first before the tail break, the second after, as indicated by (a) and (b) in Fig. 2.9. The portions (a) and (b) last 3 ms and 8 ms, respectively, and are taken 1ms prior and 8ms after the time of (c), respectively. The average difference between them is defined to be the TBF force, 59.5 mN in the example. An estimation of the TBF signal resolution σ_S is obtained by first determining standard deviations of σ_a and σ_b from the signal regions (a) and (b), respectively, and then using

$$\sigma_S = \sqrt{\sigma_a^2 + \sigma_b^2} \tag{2.1}$$

The value of σ_S is found to be 5.3 mN.

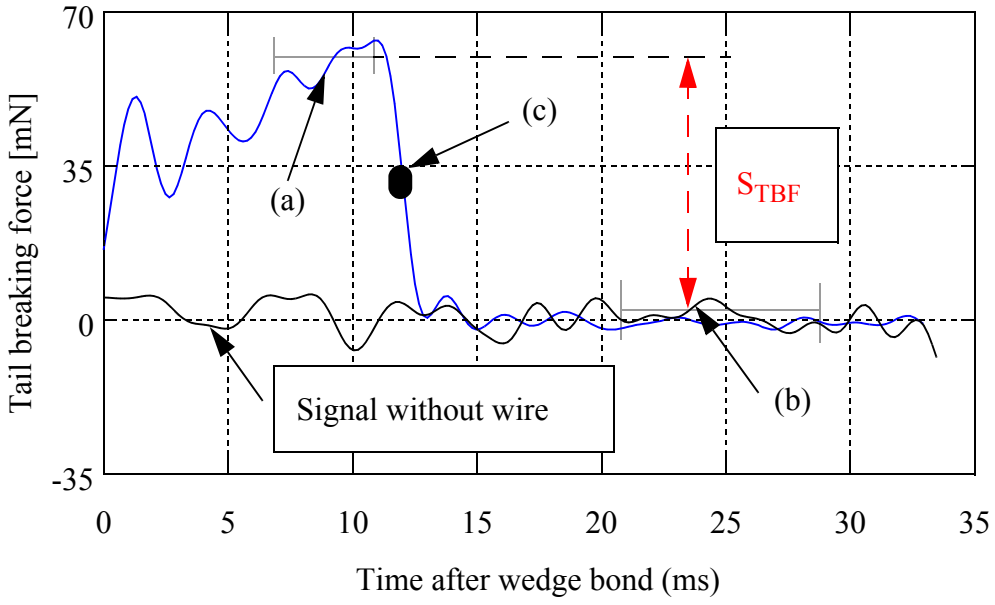

Fig. 2.9 Example measurement of TBF (a) with and (b) without wire.

2.2 Calibration

For calibration of the proximity sensor, a weight of 22.2 g is hung on the wire clamp as shown in Fig. 2.10, resulting in a force F_t = 218 mN (1 g = 9.8 mN) acting vertically downwards. The changes in online signal of the proximity sensor is recorded with an oscilloscope as shown in Fig. 2.11. In order to obtain the proximity signal with the oscilloscope, the wire bonder should be in an idle state. ESEC (Oerlikon, Cham, Switzerland) provided the special tools and technical support to get the signal while idling. A total of 10 measurements are conducted to obtain statistical values. The average signal drop, *P*, of the proximity sensor upon removal of the weight is 63.2 $\pm$ 2.12 mV.

The calibration factor (f_p) is computed using

$$f_p = \frac{P}{F_t} \tag{2.2}$$

The calibration factor (f_p) is computed to be 290 $\pm$ 10 mV/N which is, in turn, 3.45 mN/mV. The signal is divided by f_underscore_p to obtain the TBF.

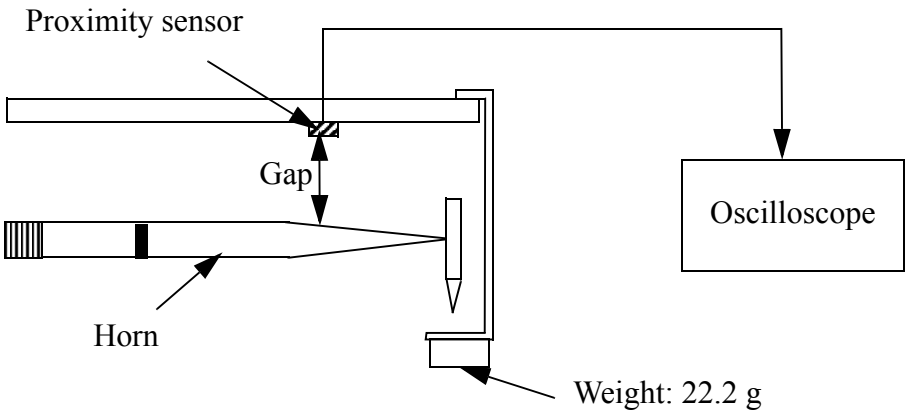

Fig. 2.10 Schematics of proximity calibration setup with weight and oscilloscope.

2.3 Optimization by Iteration

Bonding is performed on the diepad of the Ag metallized leadframe. To take into account possible leadframe variation, the same procedure is carried out as explained in chapter 2.1. Each wire has different bonding parameters. The three bonding parameters, ultrasound (US), IF, and BF, are varied. The parameters, heater temperature (T) and bonding time (BT), are fixed to 220 °C and 15 ms, respectively. The symbol "%" is used as a unit for the ultrasound parameter, where 1 % is equivalent to a peak to peak vibration amplitude of 26.6 nm measured at the center of the transducer tip.

A series of iterations is carried out each consisting of optimization runs for US, IF, and BF. Data from one example iteration are shown in Table 3.1. In this example, $IF^{(0)}$ = 1000 mN and $BF^{(0)}$ = 400 mN are the starting parameters obtained by a few initial trial and error bonding tests,

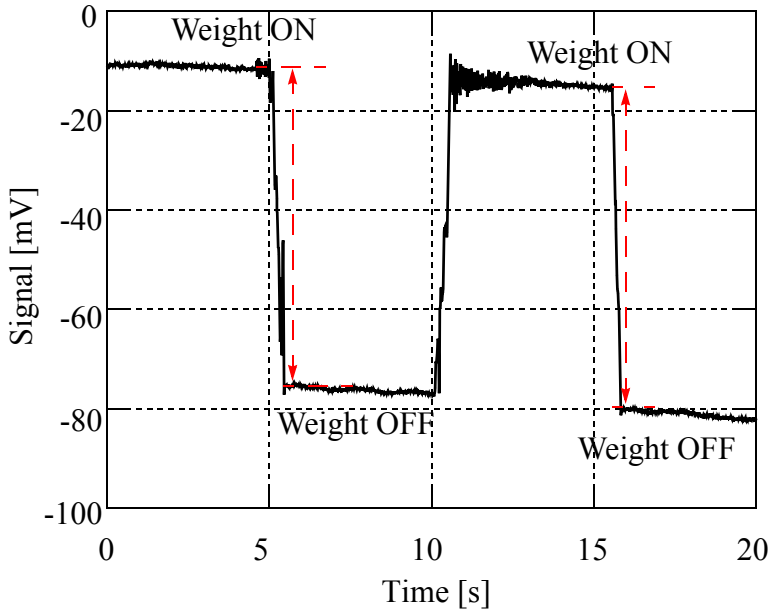

Fig. 2.11 Proximity signal with a 22.2 g weight sometimes hanging on the clamp.

and $US^{(1)}$, $IF^{(1)}$, and $BF^{(1)}$ are the optimized parameters that result from this iteration. In the 1st optimization run of the iteration, the parameters, IF = $IF^{(0)}$ and BF = $BF^{(0)}$ are fixed and US is varied in 3 % steps from 31 % to 88 %, which is the bondability range. For US values lower than 31 %, wedge lift-off occurs. For US values higher than 88 %, short tail occurs. TBF is measured for each of US parameters and that with the highest TBF is selected. This optimized value is $US^{(1)}$ = 50 %. It is used for the next run which varies IF and fixes US = $US^{(1)}$ and BF = $BF^{(0)}$. An optimized value $IF^{(1)}$ is obtained and is used for the third run for the BF optimization. Consequently, the first optimized set of the parameters is found, $US^{(1)}$= 72 %, $IF^{(1)}$ = 600mN, and $BF^{(1)}$= 400 mN, concluding the 1st iteration. The 2nd iteration uses this optimized set as starting parameters and proceeds in the same way, resulting in an optimized set of the parameters, $US^{(2)}$, $IF^{(2)}$, and $BF^{(2)}$. Subsequent iterations are carried out until the TBF values do not increase anymore. The final optimized set of the parameters is called center parameters.

Table 2. 1 Example of three runs during the first iteration.

Run		US (%)			IF (mN)			BF (mN)		
		Wire 1	Step	Wire 20	Wire 1	Step	Wire 20	Wire 1	Step	Wire 20
1st iteration	1	31	3	88	1000	0	1000	400	0	400
	2	50	0	50	300	50	1250	400	0	400
	3	50	0	50	600	0	600	300	50	1250
Optimum parameter		50			600			400		

2.4 Preliminary Optimization with Au wire

A total of 20 bonds are made with each parameter combination. From the 1st iteration to the 4rd iteration, $\overline{TBF}$ increases while s decreases. With the 4th iteration, $US^{(4)}$, $IF^{(4)}$, and $BF^{(4)}$ are found to be 72 %, 450 mN, and 950 mN, respectively. $\overline{TBF}$, standard deviation (σ), and cpk value at the optimized parameters are 62.22 mN, 2.18 mN, and 7.97, respectively. Table 3. 2 summarizes the optimized parameters, average TBF ($\overline{TBF}$), TBF standard deviation (σ), and TBF process capability index (cpk) after each iteration. To calculate the cpk value, a lower specification limit (LSL) of 10 mN is chosen. The equation for cpk value calculation is computed using

$$cpk = \frac{\overline{TBF} - LSL}{3\sigma} \tag{2.3}$$

Figures 2.12 (a) - (c) show the fourth TBF iteration results of Au wire. The grey solid lines are polynomial fits obtained with US, IF, and BF, respectively. Polynomial fitting is applied in the response surface method widely used in optimizing the wire bonding process [63, 64]. The

Table 2. 2 Optimized parameters, maximized $\overline{TBF}$, and evaluated σ and cpk for each iteration.

Iterations	Optimum parameters			$\overline{TBF}$ (mN)	σ (mN)	cpk
	US (%)	IF (mN)	BF (mN)			
1st iteration	50	600	400	50.9	5.95	2.35
2nd iteration	36	800	600	53.75	5.09	2.86
3rd iteration	72	550	1150	55.34	4.73	3.2
4th iteration	72	450	950	62.22	2.18	7.97

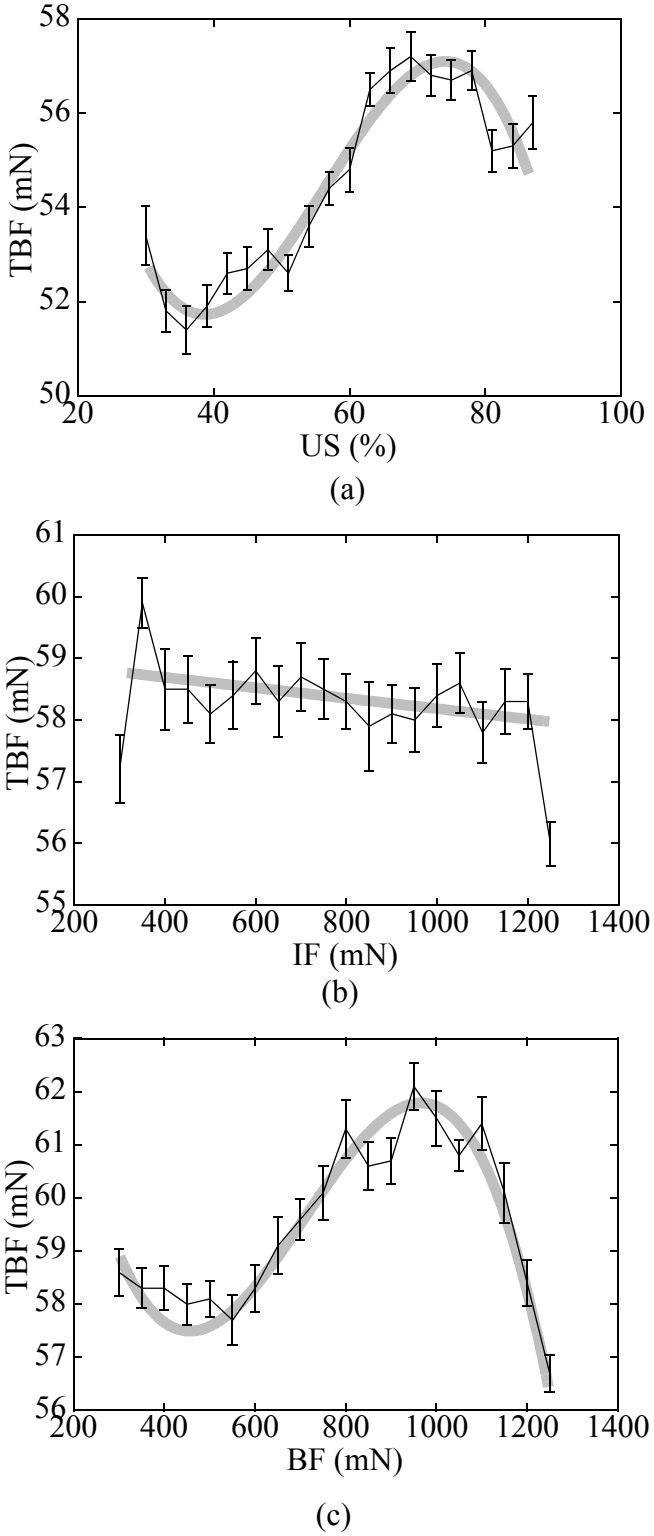

Fig. 2.12 The fourth iteration results of Au wire TBF. (a) US, (b) IF, and (c) BF. Grey lines are polynomial fits. Error bars are $\varepsilon = \sigma/\sqrt{n-1}$, n = 20.

response surface method is typically conducted with data collected from processes with parameters being varied among two or three parameter values (2^n or 3^n design of experiment). Too few parameter values can oversimplify the effect of bonding parameters on TBF. The iterative optimization method applied in this study reveals the degrees of the polynomials required to suitably fit the experimental values. In this example, the minimum degrees of polynomial suggested fits for the US, IF, and BF parameters are 3, 1, and 3, respectively. The variation of TBF with US is shown in Fig. 2.12 (a). The TBF increases gradually from 45.8 mN to 52 mN and then decreases as US is increased. The TBF decreases when IF is increased as shown in Fig. 2.12 (b). In case of rising BF as shown in Fig. 2.12 (c), the TBF increases from 400 mN to 900 mN and then decreases. In summary, the changes of US, IF, and BF parameters induce 10 %, 7 %, and 8 % of TBF change, respectively.

2.4.1 TBF Optimization of Cu and Insulated Au wires

The TBF of insulated Au wire is maximized using an iteration method the results of which are summarized in Table 2. 3. Figures 2.13 (a) - (c) show the 3rd iteration (last iteration) results at

Table 2. 3 Summary of the TBF of X-Wire^{TM} by iteration.

Iteration	US (%)	IF (mN)	BF (mN)	Av. PF (mN)	σ (mN)
1	44	900	650	60.18	5.8
2	58	750	800	61.25	5.62
3	58	800	800	62.72	5.6

various bonding parameters. The TBF is 42 mN at a US of 28 %. A sharp increase of the TBF is observed as US increases from 28 % to 38 %. After US higher than 38 %, it increases slowly and then stays constant as shown in Fig. 2.13 (a). With IF increase from 300 mN to 1150 mN, the TBF does not change. It decreases as IF increases further as shown in Fig. 2.13 (b.). The TBF does not change as BF increases from 300 mN to 700 mN. It increases as BF increases from 700 mN to 900 mN and then decreases. The maximum TBF, 60 mN, obtained with insulated Au wire is comparable to that obtained with bare Au wire. It is clear from Figs. 2.14 (a) - (c) that Au residues remain on the tail bond region after the crescent bond. The circle in the images is determined to correspond to the capillary hole. The tail bond forms not only at the area where the wire is pinched by the capillary chamfer and the die pad, but also inside the capillary hole. As US increases, the area (wire residue) pinched by the capillary chamfer and the die pad remains larger after the pull test as shown in Figs. 2.14 (b) and (c), respectively.

The TBF of the standard Cu wire bonding process is maximized with iteration, resulting in an optimized set of parameters of US = 80%, IF = 1000mN, BF = 400mN, which is summarized in Table 3. 4. Figures 2.15 (a) - (c) show the third iteration results at various bonding parameters. The TBF is increased and then decreased as US increases. The IF less affects the TBF compared to the other parameters (US and BF). The TBF is increased, decreased, and then constant as BF increases. The errors of the TBF become larger with BF higher than 700 mN, resulting in low cpk

Table 2. 4 Summary of Cu wire optimization by iteration.

	US (%)	IF (mN)	BF (mN)	TBF (mN)	σ (mN)
1st iteration	80	1000	500	57.86	7.6
2nd iteration	80	1100	450	58.12	7.5
3rd iteration	80	1000	400	58.08	7.7

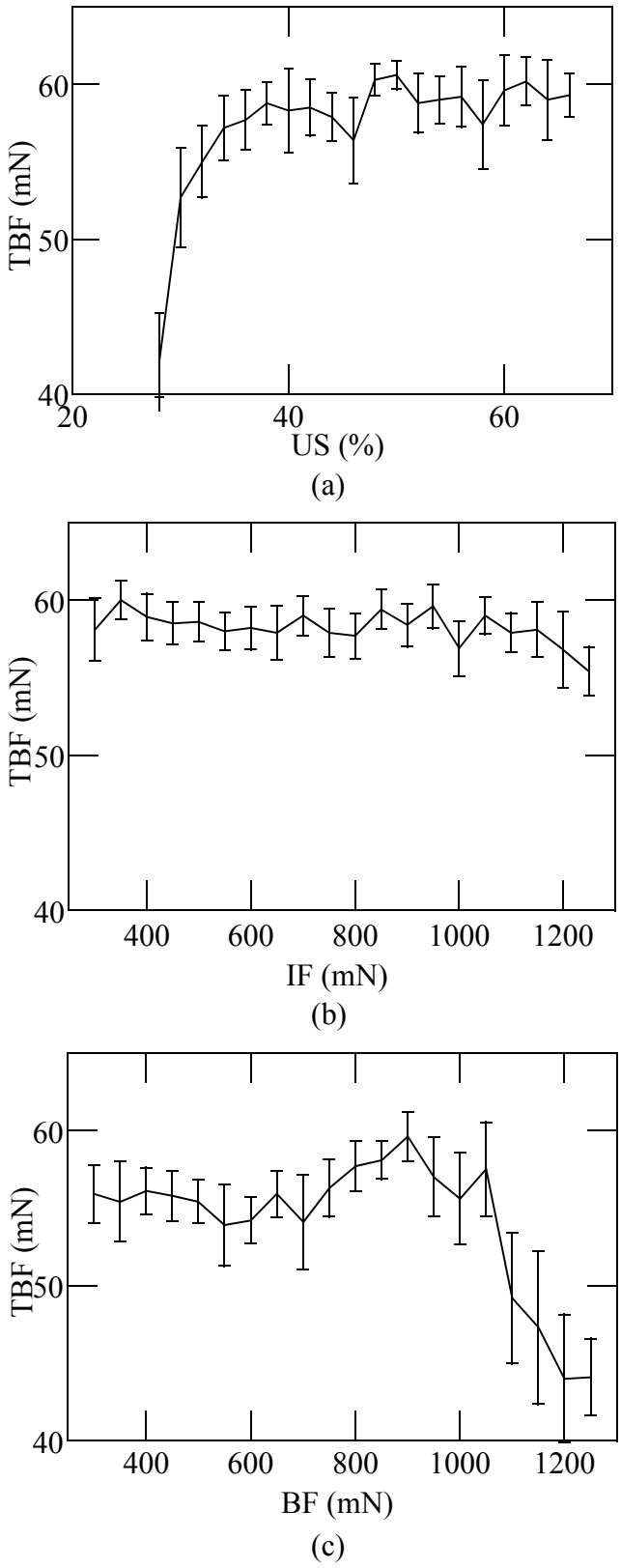

Fig. 2.13 TBF results of 3rd iteration of X-Wire^{TM}. (a) US, (b) IF, and (c) BF.

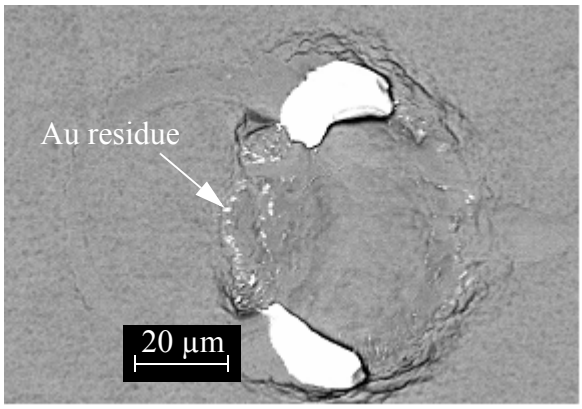

(a)

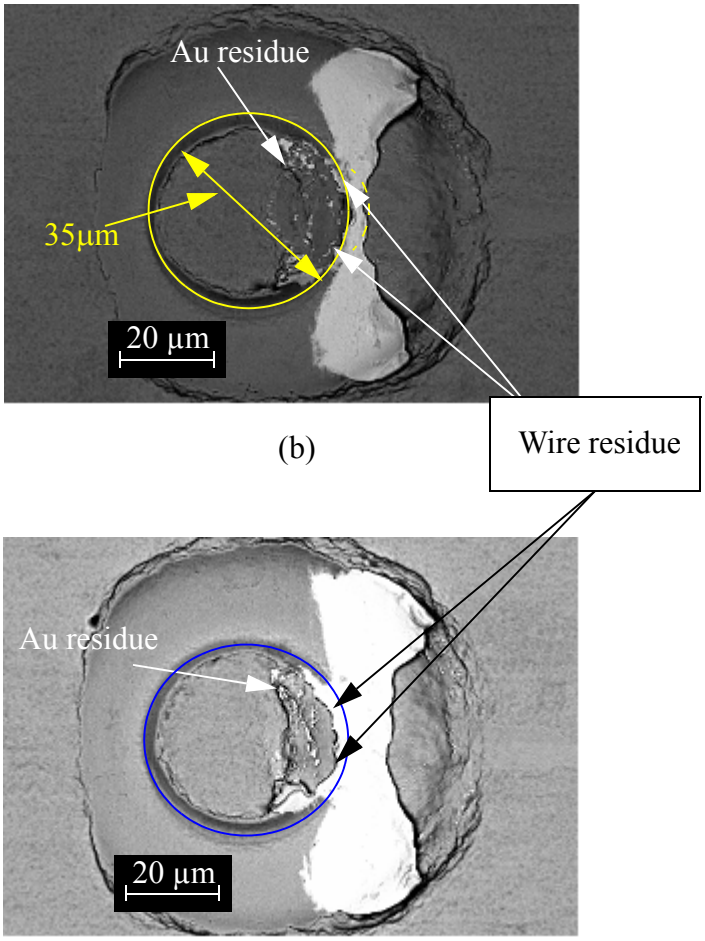

(b)

(c)

Fig. 2.14 BSE images of fracture surface on the die at various USP. (a) 50 %, (b) 52 %, and (c) 60 %.

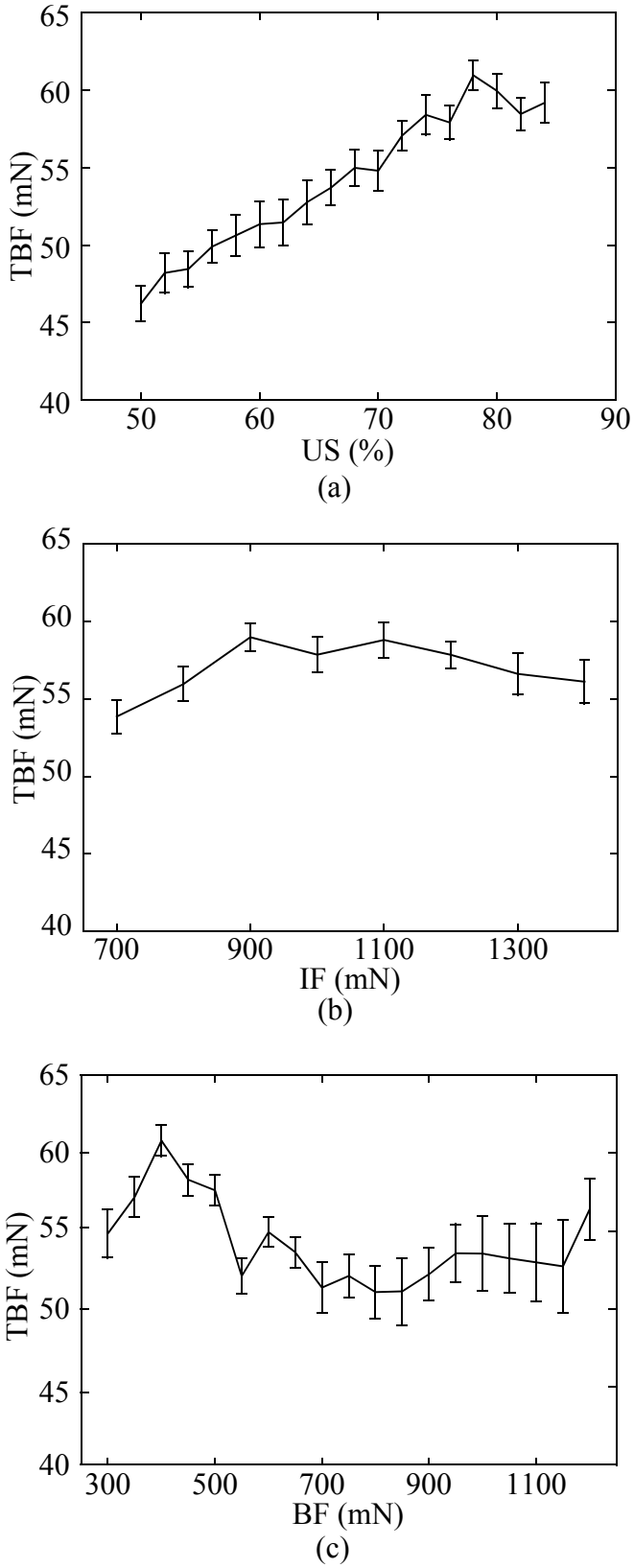

Fig. 2.15 TBF results of 3rd iteration of Cu wire. (a) US, (b) IF, and (c) BF.

value. With the 3rd iteration parameters, a confirmation run of 200 bonds made is performed. The TBF, σ, cpk of 58.54 mN, 7.1 mN, and 2.28, respectively, are obtained.

2.4.2 Comparison of TBF

A total of 160 TBF measurements are made at each center parameters and the results are compared as shown in Fig. 2.16. The distribution of TBF with Au wire is in the range between 50 mN and 60 mN as shown in Fig. 2.16 (a). With insulated Au wire, as shown in Fig. 2.16 (b), it can be seen that most of the TBF is in the range between 50 mN and 65 mN which is similar to the results obtained with Au wire. However, low TBF values indicated by the square box are also observed. These are due to the presence of insulation material on the area where the tail breaking occurs. The TBF of Cu is largely distributed as shown in Fig. 2.16 (c) which is in the range between 40 mN and 70 mN.

With the data shown in Figs. 2.16 (a) - (c), the average and cpk for each wire type are calculated as shown in Fig. 2.18 and 2.17, respectively. The average TBF values of insulated Au and Cu wires are higher than those of Au wire. However, the cpk value of Au wire is the highest, followed by insulated Au wire and Cu wire. The cpk values of Cu and insulated Au wires are about 2 and 3, respectively, which are higher than standard cpk value (2). However, the minimum error of the cpk of Cu wire is close to 2 which is calculated using [65]

$$\sigma_{cpk} = z_{1-\alpha}\sqrt{\frac{1}{9n} + \frac{cpk^2}{2(n-1)}} \tag{2.4}$$

where $Z_{1-\alpha}$ is 1.96 at a 95 % confidence level, and n = 160 is the sample size.

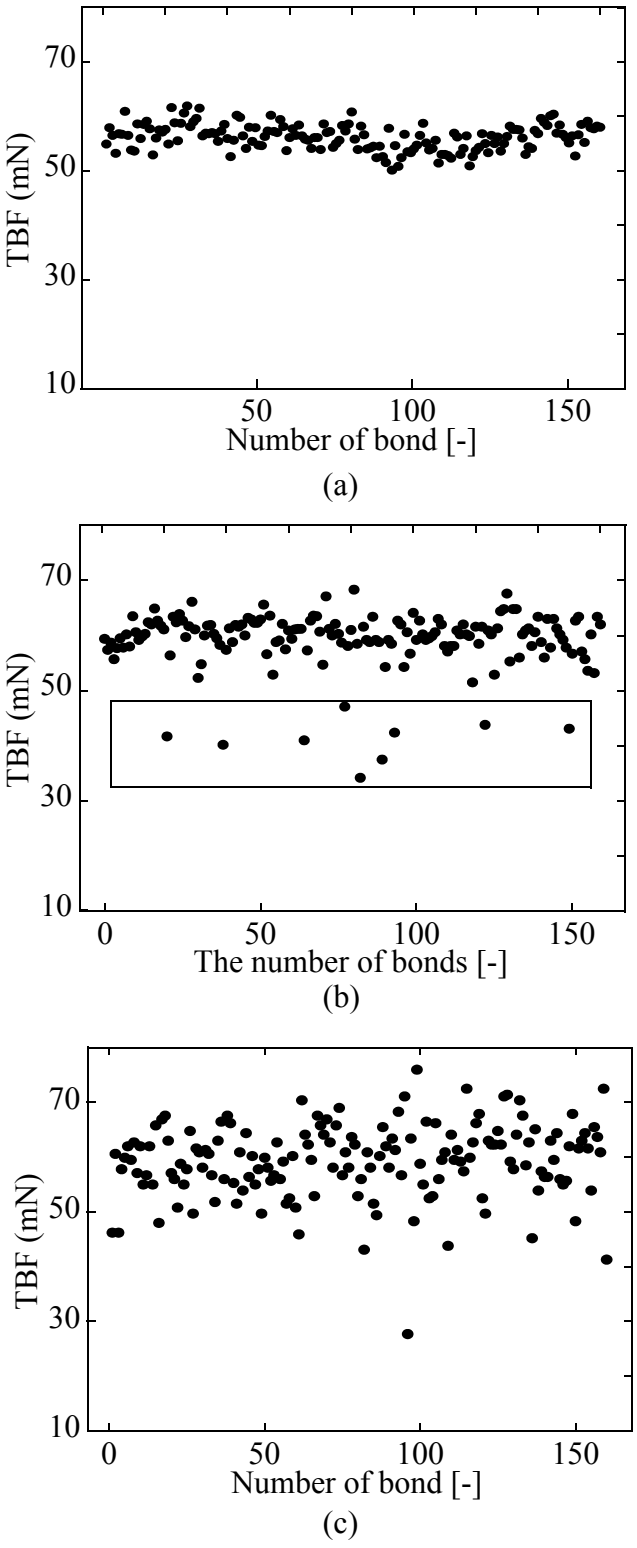

Fig. 2.16 TBF distributions at the center parameters. (a) Au, (b) Insulated Au, and (c) Cu wires.

The probability of cpk value to be lower than 2 with Cu wire is higher compared to those with Au and insulated Au wires. Increase of the TBF cpk value with Cu wire is required to improve the Cu wire bonding process. Detailed investigation of the TBF with Cu wire will be discussed in chapter 4.

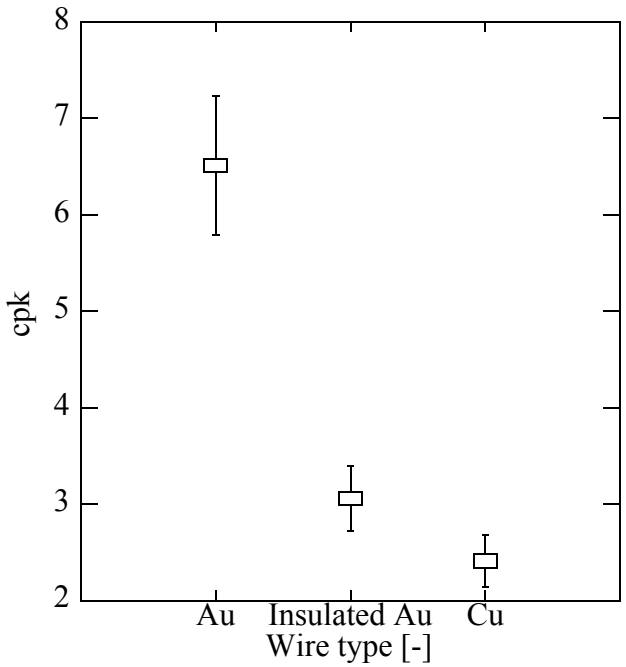

Fig. 2.17 cpk values with Au, Insulated Au, and Cu wires at the center parameters. n = 160.

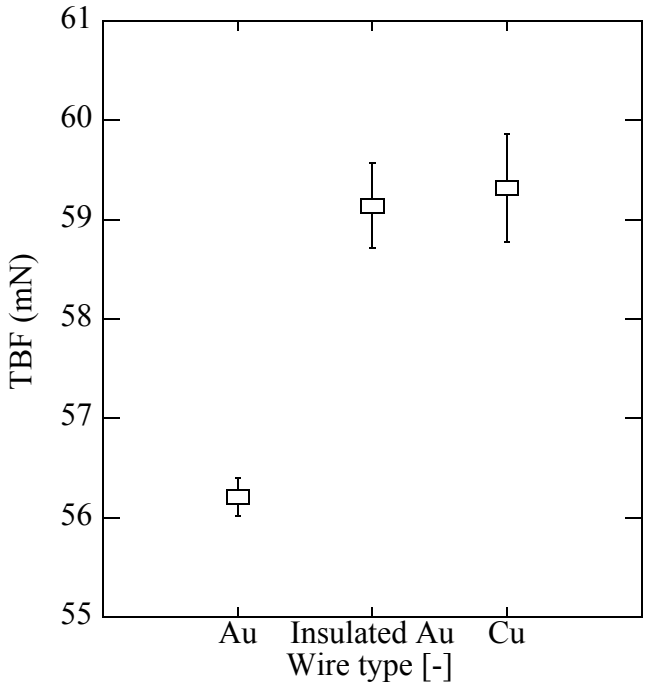

Fig. 2.18 Average TBF values with Au, Insulated Au, and Cu wires at the center parameters. Error bars are $\varepsilon = \sigma/\sqrt{n-1}$ n = 160.

2.5 Influence of plasma cleaning on the TBF

Besides the bonding parameters, other factors such as pad metallization and cleanliness affect the TBF. Since many variables are to be considered in metal plating [66, 67], the thickness and surface quality can vary over the surface and from sample to sample [68]. Therefore, the die-pad induced TBF variation and the diepad cleanliness are investigated. TBF measurements are carried out on 5 diepads fresh from the box but not plasma cleaned, and on 5 diepads plasma cleaned with 100 % Ar for 5 min. Before and after plasma cleaning, the diepad to diepad variation of the TBF obtained with Au and Cu wires is compared. The results are shown in Figs. 2.19 and 2.20, respectively. Before plasma cleaning, the Cu wire TBF is between 48.5 mN and 60.1 mN, a

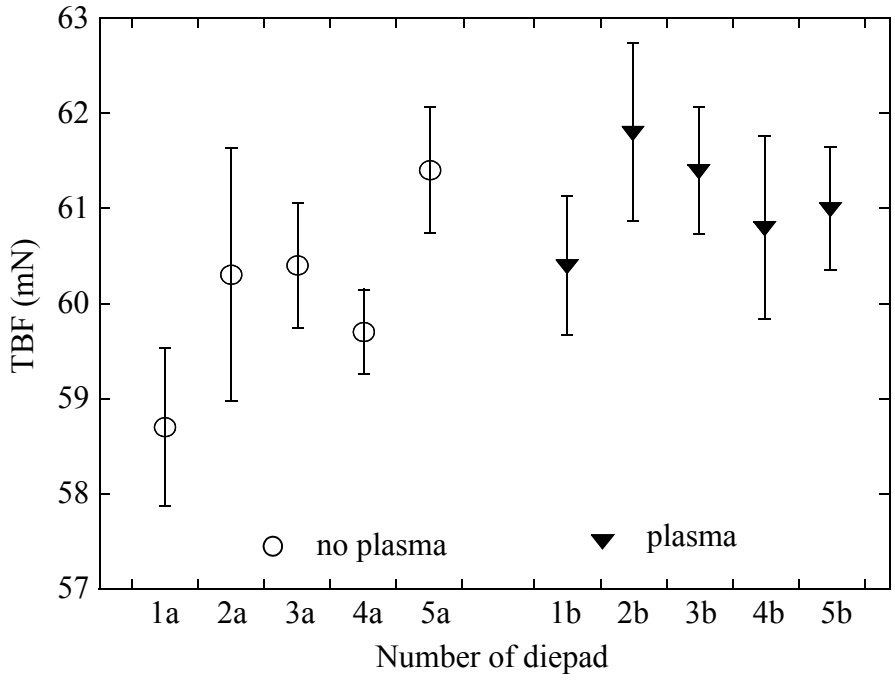

Fig. 2.19 Comparison of diepad induced Au wire TBF variation with and without plasma cleaning. Error bars are $\varepsilon = \sigma/\sqrt{n-1}$, n = 80.

range 4 times larger than that of Au wire. After plasma cleaning, the diepad induced TBF variation of both Au and Cu wires become as small as 1.4 mN and 4.2 mN, respectively.

To further study the influence of plasma cleaning and the TBF process is carried out with the US parameter varied from 46 % to 84 % in steps of 4 %. The BF, IF, BT, and T parameters are fixed to 500 mN, 1000 mN, 25 ms, and 220 °C, respectively. They are the optimized parameters for the Cu wire TBF process. The TBF comparison results are shown in Fig.2.21. Each point is the average of 40 measurements from bonds distributed over 8 diepad samples. Similar to the wedge bondability of Au wire on the bonding pads [76, 77], the TBF is increased after plasma cleaning on the diepad. This increase is larger with Cu wire than with Au wire. The errors are in the range of 0.79 to 1.11 mN for the Cu TBFs obtained without plasma cleaning and they decreases to a range of 0.48 to 0.95 mN with plasma cleaning.

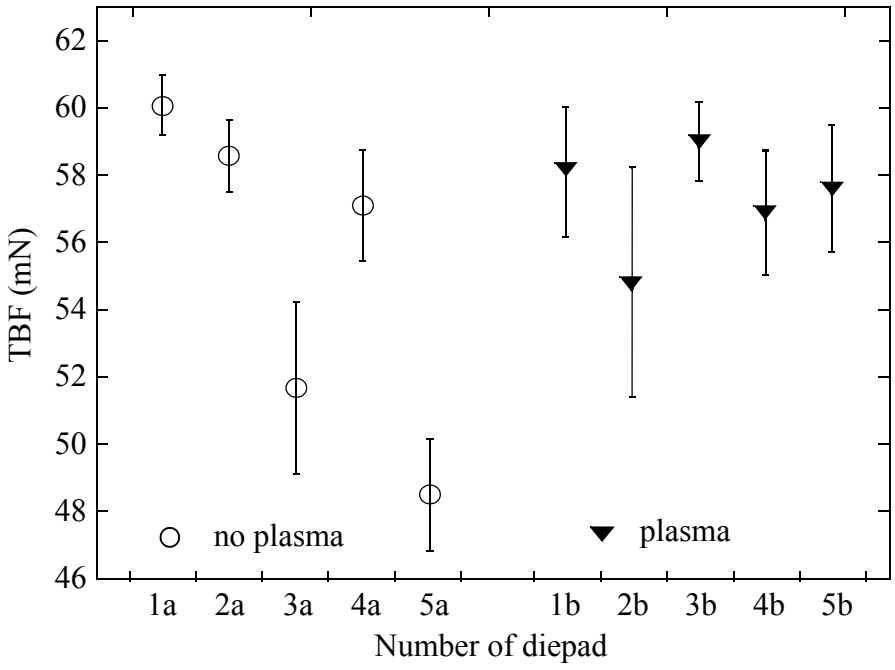

Fig. 2.20 Comparison of diepad induced Cu wire TBF variation with and without plasma cleaning. Error bars are $\varepsilon = \sigma/\sqrt{n-1}$, n = 80.

These higher $\overline{TBF}$ and lower error values obtained after plasma cleaning result in higher cpk values, which means that the process is more stable after plasma cleaning as shown for Au wire in Figs.2.22 and 2.23. The error of cpk as expressed with the error bars in Figs. 2.22 and 2.23 is calculated with Eqn (2.3) [78].

With Au wire, a cpk above 9 is obtained with 46 % to 62 % of US. It decreases to about 6 as US increases above 62 %. Not much difference is shown in the cpk values before and after plasma cleaning. With Cu wire without plasma cleaning, the highest cpk values are 2.45 and 2.36 and are obtained with 58 % and 70 % of US, respectively. After plasma cleaning, the highest cpk of 4.61 with Cu wire is obtained with 62 % of US. Therefore, it is concluded that plasma cleaning of an Ag plated bonding surface increases the tail bonding quality of a Cu wire bonding process significantly.

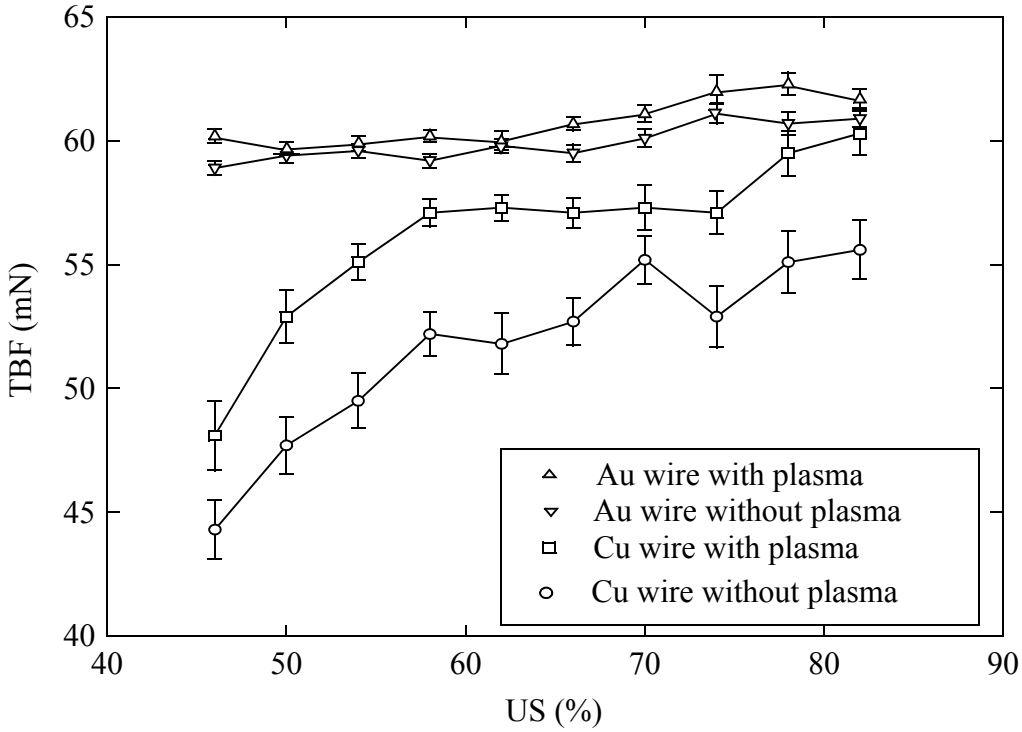

Fig. 2.21 Effect of diepad cleanliness on Au and Cu wire TBF. Error bars are $\varepsilon = \sigma/\sqrt{n-1}$, n = 40.

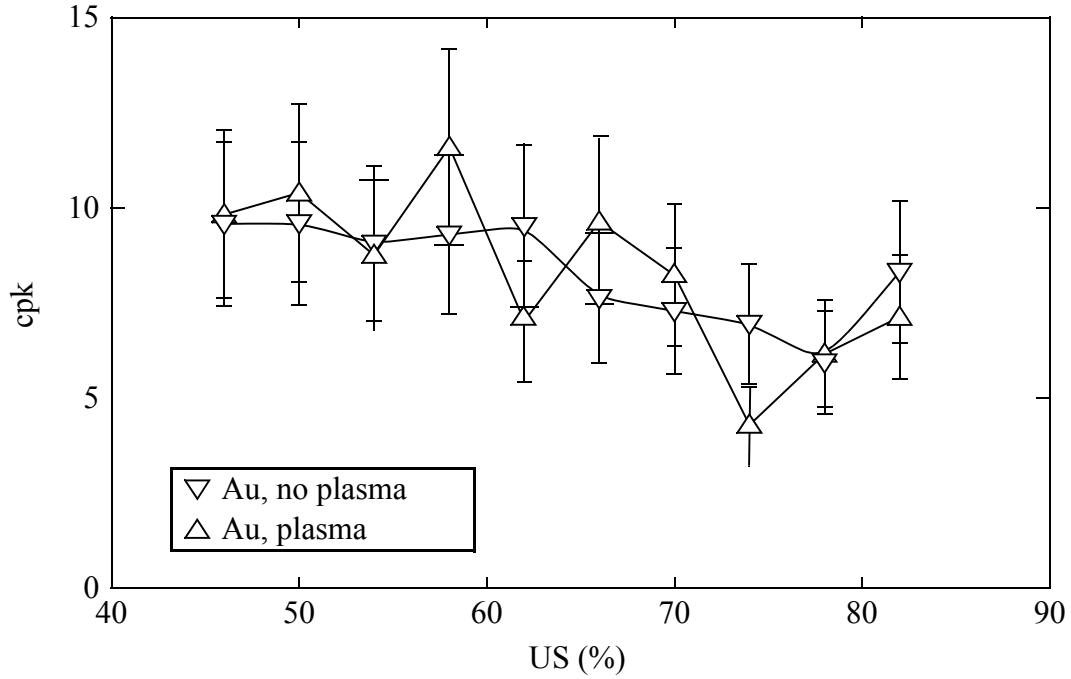

Fig. 2.22 Comparison of Au wire cpk values before and after plasma cleaning. Sample size, n,= 40.

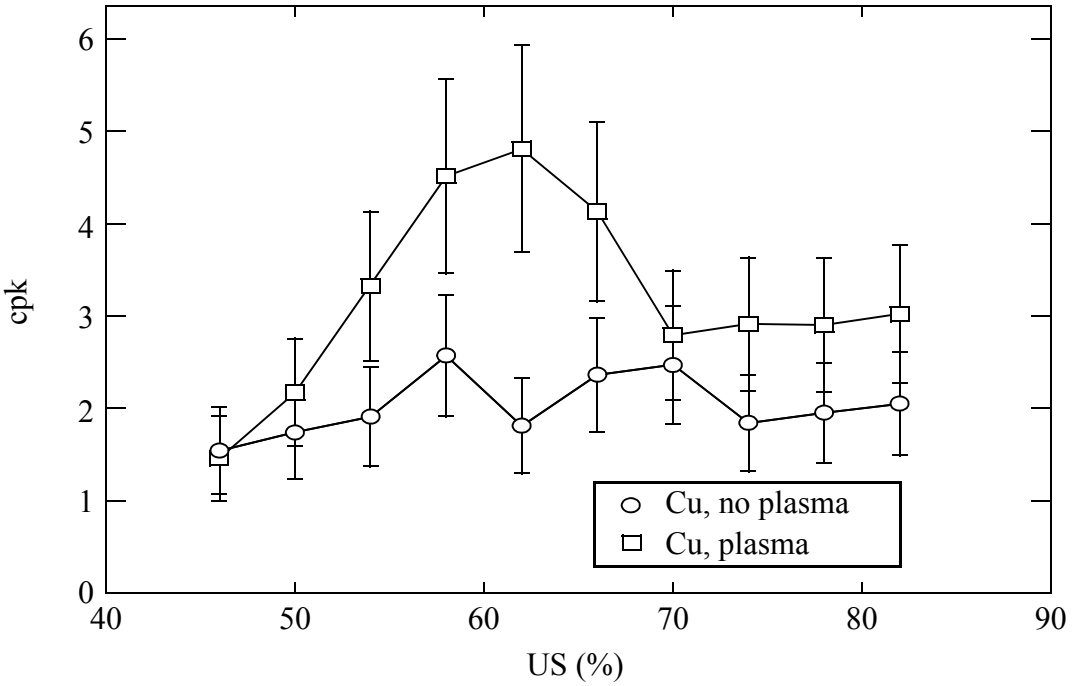

Fig. 2.23 Comparison of Cu wire cpk values before and after plasma cleaning. Sample size, n,= 40.

2.6 Summary

For measurement of tail bond strength, an online tail breaking force (TBF) measurement method is developed with proximity sensor attached on the horn, and is calibrated with a dead weight. The TBF is optimized by iteration over a range of bonding parameters of ultrasound, impact force, and bonding force. The major findings from this study are summarized as follows:

- With a sensor measuring the distance between wire clamp and horn, the TBF can be measured with a resolution better than 5.2 mN.

- The TBF depends on the bonding parameter combination. The highest TBF of 62.22 $\pm$ 2.18 mN with Au wire is obtained at 72 %, 450 mN, and 950 mN of US, IF, and BF, respectively. The Cpk is 7.97.

- Fitting polynomials to TBF values obtained with various parameters, as used for surface response optimization methods, shows that the minimum degrees of a polynomial to fit well are 3, 1, and 3, for the parameters, ultrasound, impact force, and bonding force, respectively.

- The TBF depends on the wire materials. The average TBFs of Cu and Insulated Au wires are comparable to those of Au wire. The stability of the tail breaking force is highest with Au wire, followed by Insulated Au and standard Cu wires.

- Using plasma cleaning prior to bonding, the tail breaking stability of the Cu wire process increases significantly.

Chapter 3 Influence of Insulation Layer on Crescent Bond Pull Force

As the semiconductor industry moves to shrinking die and pad pitch and 3-D packaging solutions [37] to meet the demands of low cost, higher I/O interconnection, and more electrical power for electronic devices, new and disruptive technologies are needed to meet the many challenges.

The challenge associated with thinner or longer wire is to prevent wire sweep and shorts which can occur during molding of wire bonded packages [69, 70]. In the molding process the forces caused by resin flow can displace the fine wire loops. This flow-induced deformation of the wire loop can result in wire shorting and the failure of the device.

Insulated bonding wire is a disruptive technology that is gaining more and more momentum [37]. Its insulating capability improves the flexibility of wire bond design as the wires can touch each other without impairing the device specifications. Longer wires, sagging wires, crossing wires, lower loops, wire sway, and wire sweep are no roadblocks to production anymore and can be acceptable if insulated wire is used.

The main drawback of insulated Au wire is associated with the insulation layer which is deposited on bare Au wire. The insulation layer needs to be locally pushed aside so that consistent wire to substrate contact can be made in order to obtain stable quality of crescent bonds. If insulation on material becomes incorporated in the bonding interface, it significantly reduces the friction between the bonding materials [33]. This can lower the crescent bond strength. The

morphology modification of a capillary tip [35] is previously studied in order to improve the wire pull strength of the crescent bond. The unique surface characteristic which has relatively deep lines with no fixed directions, can have less slipping between the wire and the capillary tip surface in contact and provides better ultrasonic transfer from the capillary to the bond interface, resulting in improvement of the bondability of the crescent bond. In this thesis, however, the focus is on fundamental characteristics of insulation layer removal from insulated Au wire and how the layer interacts with the substrate. A new bonding process is introduced in order to improve the quality of the crescent bond. The cpk value of the TBF with insulated Au wire is 3 which is stable as reported in Chapter 2.4.2 so that no further investigation is carried out on the TBF.

This chapter is focused on the crescent bond (2nd bond, or wedge bond) with insulated wire The limitation of pull force of insulated Au wire will be presented in Chapter 3.2. Cleaning stage (CS) process in order to increase the pull force of insulated Au wire will be introduced in Chapter 3.3. An effort is made to understand the insulation cleaning effect on bonding parameters in Chapter 3.4.

3.1 Experimental

The wire bonder used is an ESEC 3088 auto ball bonder as produced by Oerlikon Esec, Cham, Switzerland as shown in Fig.3.1. This is a fully automated bonder which is computer controlled. This bonder has a moving electrode which moves toward the wire tail during the EFO process, then the EFO forms the FAB. It performs automated bonding with a bonding program without operater intervention unless a problem arises. The bonding programs include bond position, material handling, and bonding parameters. This bonder is equipped with a kit for Cu wire bonding.

Fig. 3.1 Photograph of ESEC 3088 auto bonder.

Standard Au wire and insulated Au wire available from Microbonds, Markham, Canada, (X-Wire^{TM}), all with 25 μm diameter, are used for bonding. Insulated Au wire has a nano - scale (100 - 250 nm in thickness) insulation layer covering the Au wire surface as shown in Fig. 3.2.

The "ball-wedge-wedge" (BWW) function is used to produce double wire loops for this study. These loops have a middle bond between the first and the last bond as shown in Fig. 3.3 and illustrated in Figs. 3.4 (a), (b), and (c). The BWW function does not break the wire after a first

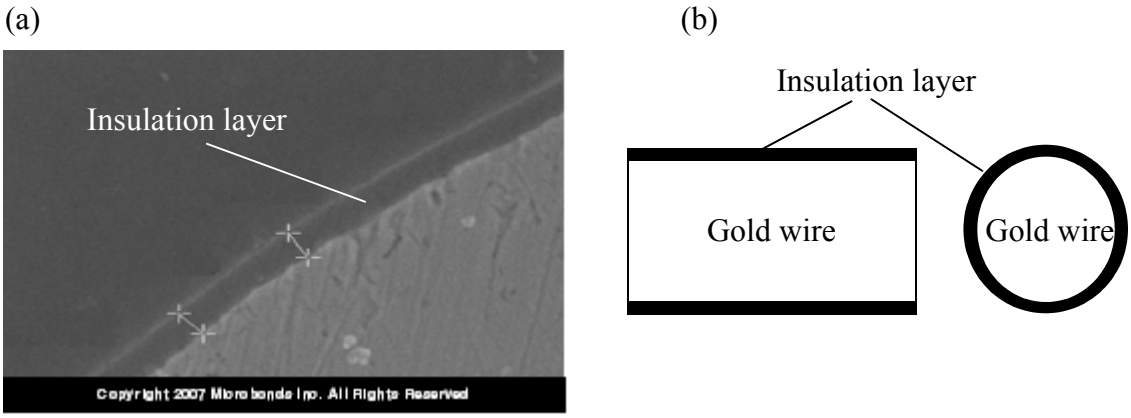

Fig. 3.2 SEM image of (a) cross-section of insulated Au wire and (b) its illustration.

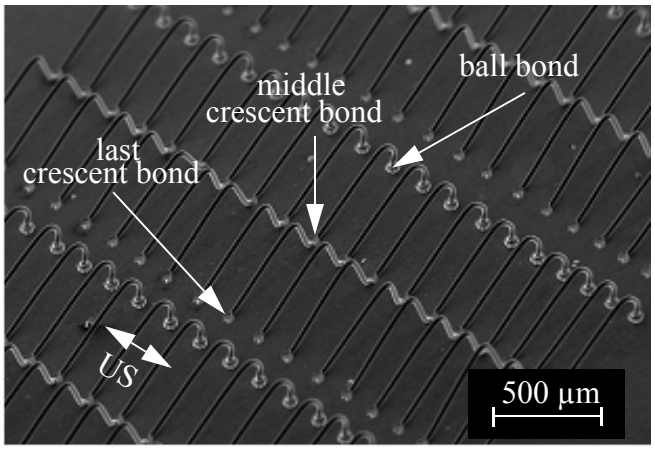

Fig. 3.3 BWW bonds used to optimize PF of middle crescent bonds.

wire loop but adds a second wire loop before generating a new tail. The second bond of the first loop is also the first bond of the second loop. The second looping trajectory does not have a reverse motion in order to not weaken or break the middle bond. Therefore, the second loop turns out to be flatter than the first. The first and last bonds are made with parameters optimized for strength and always stick well. The middle bond is made with varying parameters for this study and sometimes does not stick ("lift-off"). However, the second loop can be formed even if the middle bond is weak or lifts off, still allowing for continuous BWW bonding without the need to

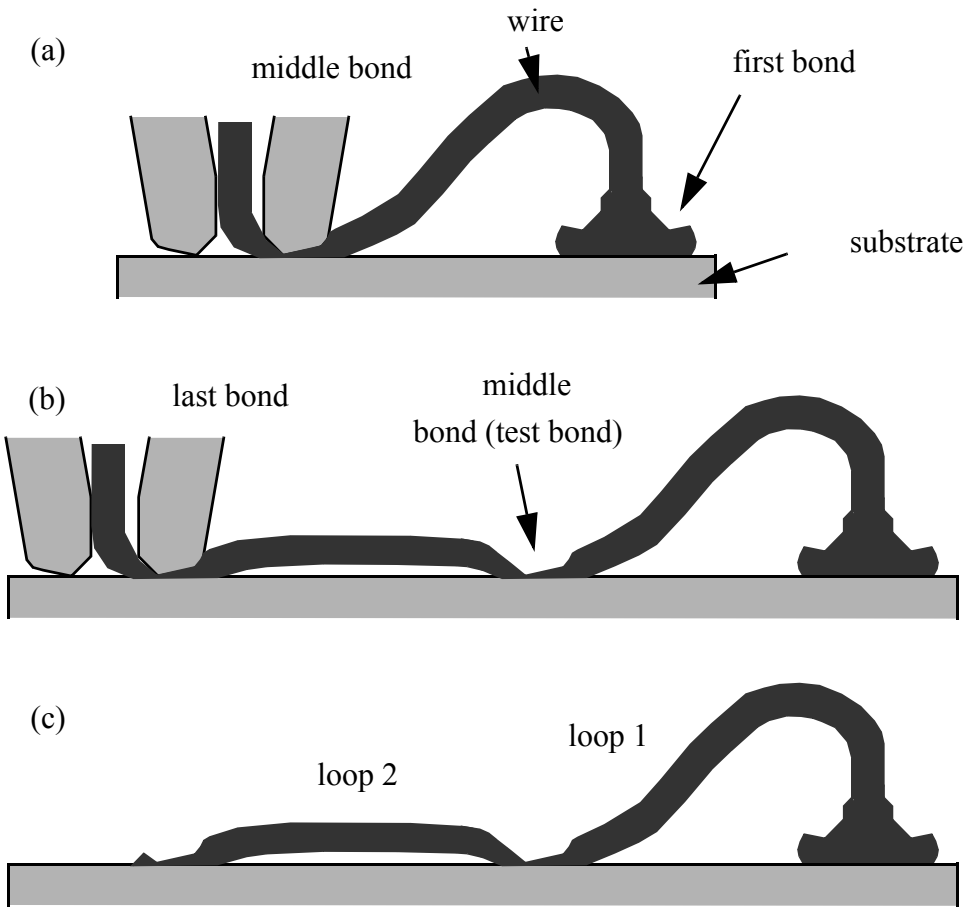

Fig. 3.4 Concept of BWW bonding. (a) first (ball) and middle bond (crescent/wedge), (b) last bond (crescent/wedge), (c) final two loops.

attend to the machine. The use of the BWW middle bond as test bond therefore greatly accelerates the data collection for this study.

Crescent bonds are made with bare and insulated wires using a basic and a modified process. For simplicity, all wire loops are directed perpendicular to the ultrasonic direction in this study. The quality of the bonds is determined using the pull force (PF) as measured by the standard pull test. During the test, the pull speed is 200 μm/s. The hook location is on the first loop at about 30% of the loop width away from the crescent bond.

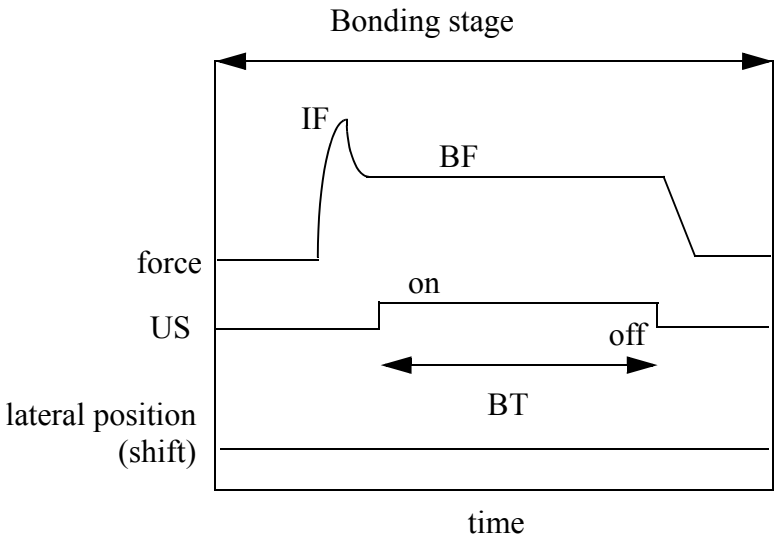

Fig. 3.5 Basic process type. Illustration of crescent bond parameter profiles. Signals not to scale.

3.2 Bonding with Standard Process Type

The standard process is characterized by the shape of its parameter profiles as illustrated in Fig. 3.5. The machine settings are impact force (IF), bonding force (BF), ultrasound (US), ultrasound time (BT), and shift distance. The starting parameters for the crescent bond PF optimization by iteration as described in Chapter 2 are IF = 750 mN and BF = 350 mN with insulated wire. After the optimization of the US, the IF and the BF are optimized in the same way, concluding the first iteration. With the third iteration no significant PF improvement is found in this case.

The iteration results are summarized in Table 1. The maximum PF is obtained with US, IF, and BF of 15 %, 500 mN, and 500 mN, respectively. The iteration results obtained with bare wire

are listed in Table 2 for comparison. The optimized parameters in that case are similar to those shown in Table 1 except for 10 % lower IF and BF values.

The results of PF confirmation runs with insulated and bare Au wire are shown in Fig. 3.6. The PF differs from those obtained in previous optimization runs possibly due to the equipment having been run in during a longer time during confirmation.

The average PF obtained with the insulated Au wire is 71.5 $\pm$ 8.0 mN which is 81% of that obtained with bare Au wire, 87.7 $\pm$ 6.2 mN. The PF of insulated Au wire is affected by the insulation material remaining at the interface after bonding as shown in Fig. 3.7. The figure shows a bond footprint observed after the bonded wire is peeled off with a tweezer. The black areas are insulation material that remained on the substrate. Such residues reduce the total metallic bonded area resulting in a smaller PF value.

Table 3. 1: Optimization of crescent bond PF of insulated Au wire process.

Iteration #	US (%)	IF (mN)	BF (mN)	Av. PF (mN)	σ (mN)
1	30	700	400	61.6	9.51
2	15	500	500	65.16	7.40
3	15	500	500	64.74	7.30

Table 3. 2: Optimization of crescent bond PF of bare Au wire process.

Iteration #	US (%)	IF (mN)	BF (mN)	Av. PF (mN)	σ (mN)
1	13	450	400	85.58	4.81
2	15	450	450	86.16	6.02
3	15	450	450	85.83	8.38

As PF with insulated wire comparable with that of bare wire is not achieved with this basic process type, a modified process type improving the PF with insulated wire is studied in the next section.

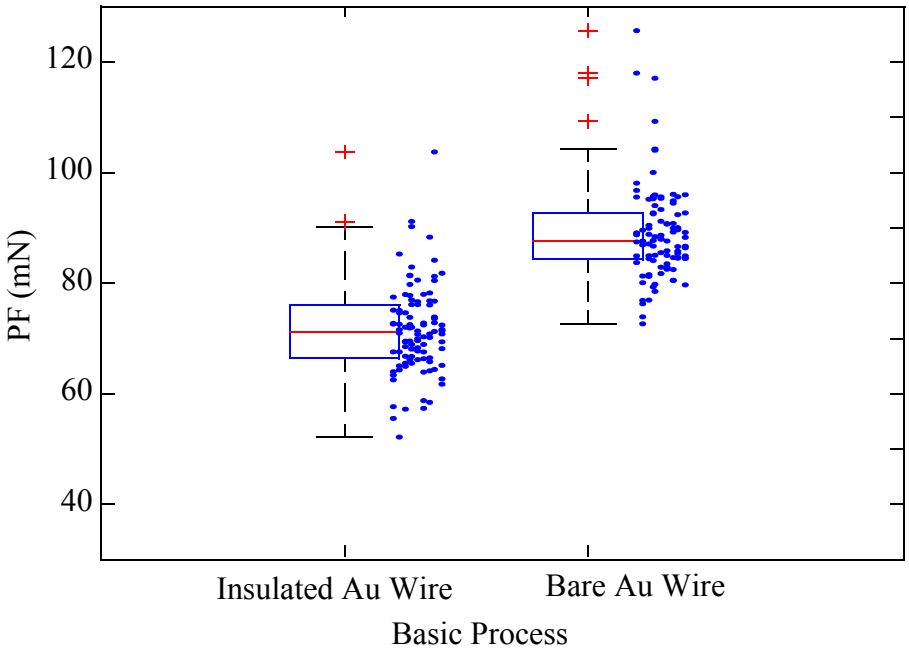

Fig. 3.6 Comparison of optimized pull force of crescent bonds with insulated Au wire and bare Au wire using basic bonding procedure.

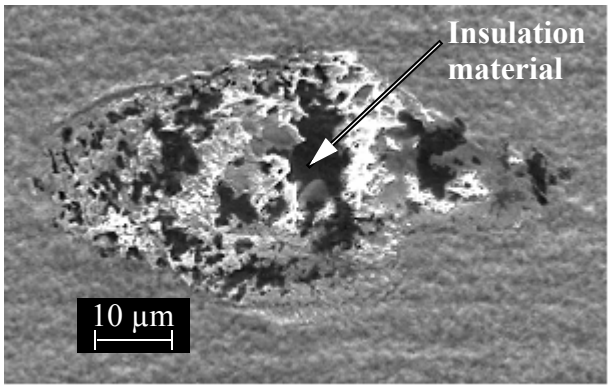

Fig. 3.7 SEM of fracture surface after peeling off crescent bond. US = 15%, IF = 500 mN, BF = 250 mN.

3.3 Bonding with cleaning stage (CS)

A cleaning stage (CS) is inserted before the basic bonding stage. The parameter profiles of this “CS process” are illustrated in Fig. 3.8. Ultrasonic friction can clean a bonding interface from oxide layers and various other impurities during a thermosonic wire bonding process [73, 74]. The CS process relies on ultrasonic friction to clean away the insulation and improve the PF of the bond.

First, an IF is applied to produce an initial deformation of the wire. It is followed by the CS in which a shift combined with ultrasonic friction is applied to remove the insulation layer. The shift is directed towards the ball bond. The maximum shift distance offered by the equipment is 20 µm. This value is chosen for all trials of this study. The CS is followed by a bonding stage with the previously optimized process parameters BF and US. The process parameters during cleaning are the force BF_C, ultrasound US_C, ultrasound duration BT_C, and shift distance. These parameters

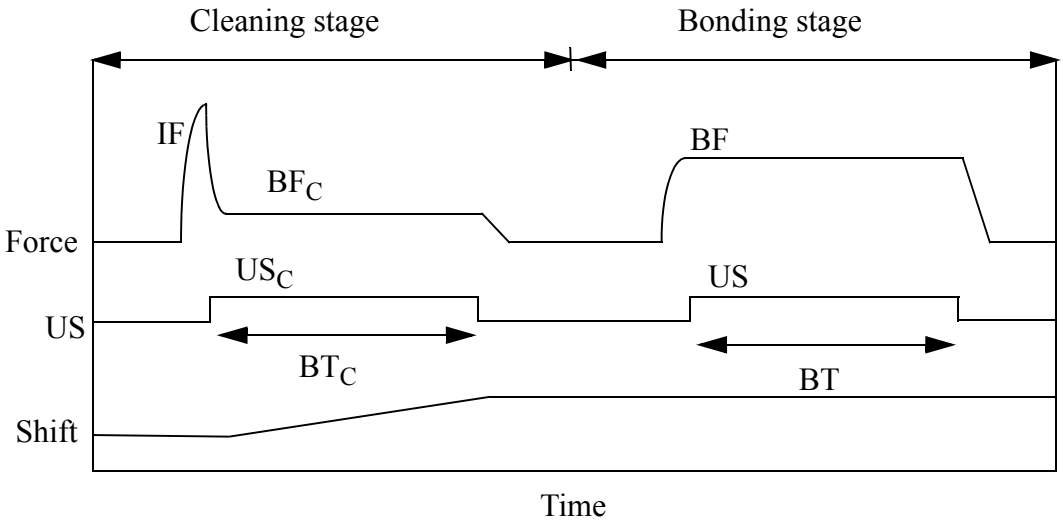

Fig. 3.8 Modified process type with cleaning stage (CS process). Illustration of crescent bond parameter profiles. Signals not to scale.

are chosen from a “non-stick window” in order to avoid any sticking or wire cut and so to facilitate the shifting motion and avoid premature tail breaking. Non-stick windows for various IF values are experimentally determined and shown in Fig. 3.9.

The efficiency of the CS is investigated by measuring the amount of insulation layer removal. For this, test middle bonds are produced without bonding stage and are rolled over with the pull hook of the commercial pull tester as illustrated in Figs. 3.10 (a) and (b). The result of this sample preparation procedure is shown by the optical micrograph in Fig. 3.11. While the middle bond is already loose, the last bond is broken or peeled off during this procedure.

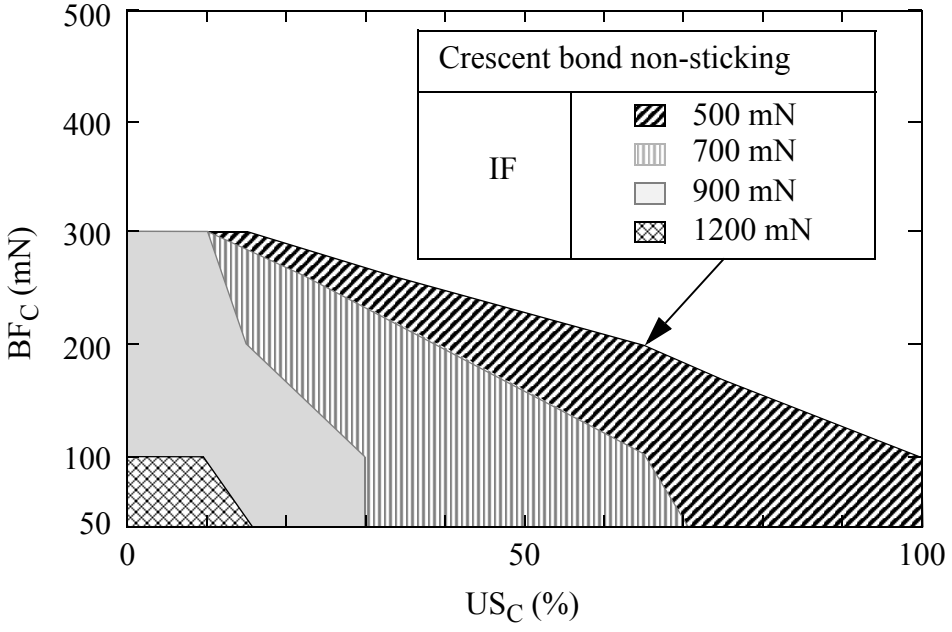

Fig. 3.9 Crescent bond non-sticking parameter regions (windows) for various IF. Non-stick windows obtained with higher IF contain those obtained with lower IF.

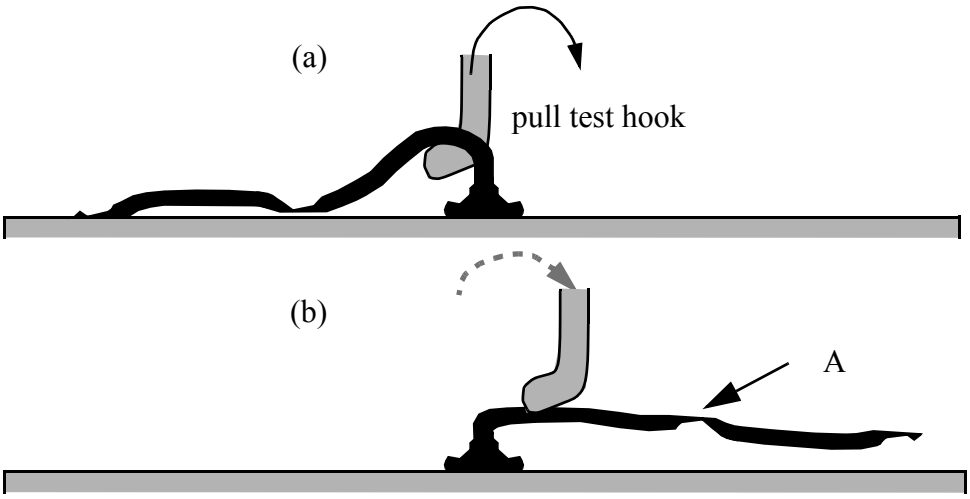

Fig. 3.10 "Rolling over" of BWW loops. (a) hook placed under first loop. (b) final position after breaking (middle and) last bond and subsequent bending. Bond interface (contact area) of middle bond (A) exposed.

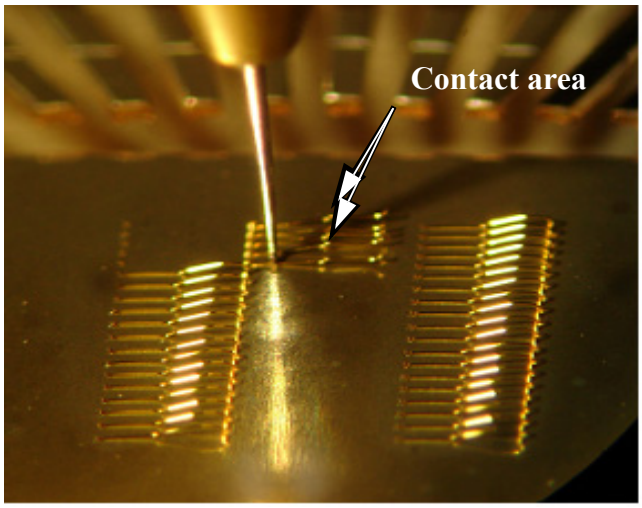

Fig. 3.11 Rolling over method to prepare samples to investigate contact area of middle crescent bonds.

3.4 Influence of IF/US on Insulation Layer Removal

In the basic parametrical study reported in this section, IF and US_C values are varied while BF_C = 50 mN, BT_C = 25 ms, and shift = 20 µm. To allow for a clear visual characterization of the insulation removal in these tests, no bonding stage is used after the CS. The middle bonds lift off and their wire contact areas are readily visible after rolling over the loops.

The effects of IF values of 500 mN, 700 mN, 800 mN, and 1200 mN on the insulation layer removal are shown in Figs. 3.12 (a), (b), (c), and (d), respectively. With the lowest values,

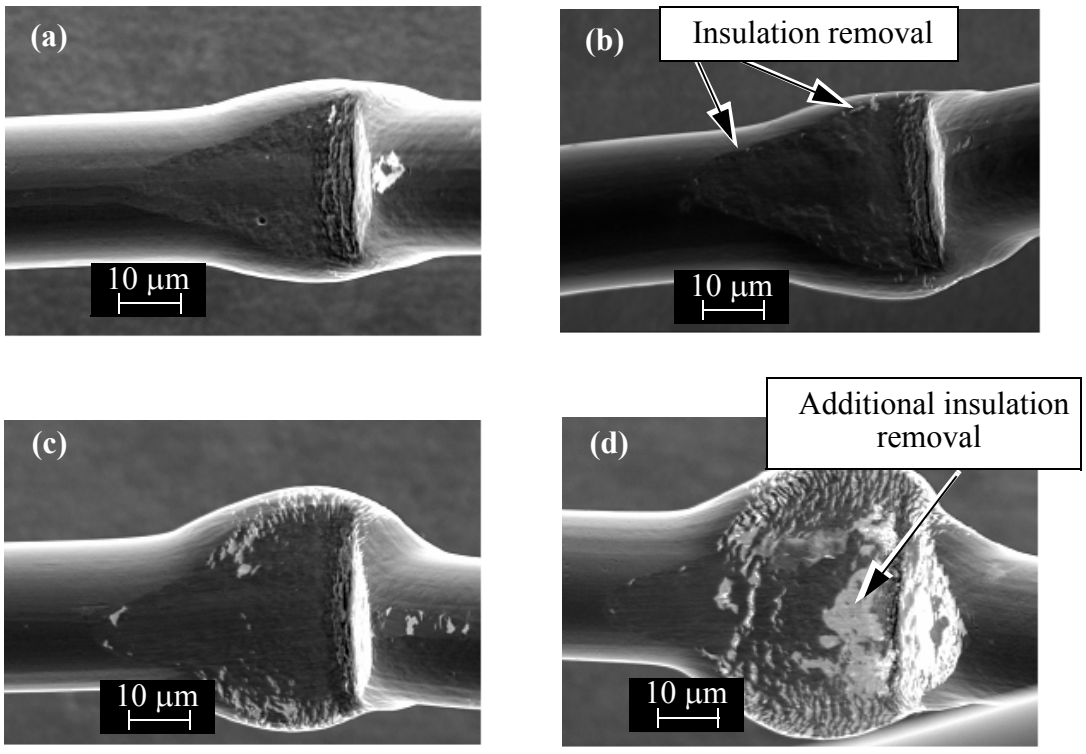

Fig. 3.12 SEM images of contact area of wires deformed with IF (a) 500 mN, (b) 700 mN, (c) 800 mN, (d) 1200 mN. US_C = 0 %, BF_C = 50 mN, BT_C = 25 ms, T = 220 °C, shift = 0 µm. No bonding stage.

IF = 500 mN [Fi.g 3.12 (a)], plastic deformation of the crescent bond but no removal of the insulation layer is observed. With IF = 700 mN as shown in Fig. 3.12 (b), limited insulation layer removal indicated by white areas is observed at the periphery of the bottom of the crescent bond. This is consistent with the amount of plastic deformation and contact pressure being largest at the periphery [75].

With IF = 800 mN, more insulation is removed towards the center of the contact zone as shown in Fig. 3.12 (c). Increased plastic deformation of the wire caused by the increased IF leads to more insulation cracks. The possible reason is the difference in ductility between the Au wire and the insulation material. With IF = 1200 mN, an additional type of insulation layer removal in the center is observed in Fig. 3.12 (d). The insulation layer is partly detached from the wire and is left on the diepad as shown in Fig. 3.13. The insulation parts are found both on the tail and crescent bond areas.

The effects of US_C on insulation removal of processes with IFs of 500 mN and 1200 mN are studied. The bottom surfaces of the deformed wires observed with IF of 500 mN and US_C of 0 %, 15 %, and 50 % are shown in Figs. 3.12 (a), 3.14 (a), and 3.14 (b), respectively. No insulation layer removal is observed with US_C of 0 %. As US_C is increased to a moderate 15 %, about 38 % of insulation layer is removed at the contact zone periphery. About 75 % of insulation layer is removed with US_C of 50 % everywhere on the contact zone.

With US_C of 50 % a major portion of the interfacial insulation layer is transferred to the substrate as shown in Fig. 3.15. With application of the shift of 20 µm toward to the ball as described in Fig. 3.8, a bare wire portion of the insulated wire is now available to be bonded to a fresh portion of the substrate.

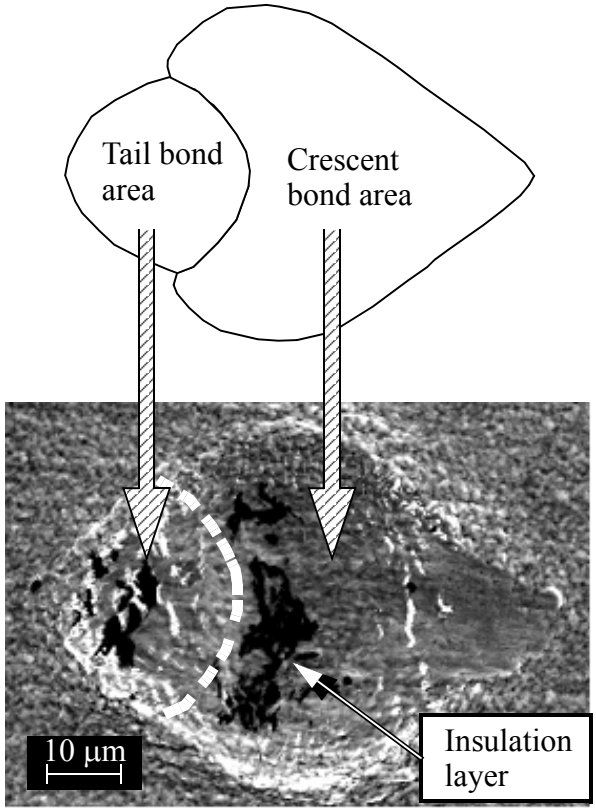

Fig. 3.13 SEM image of primary bonding site. Insulation layer transferred to substrate.

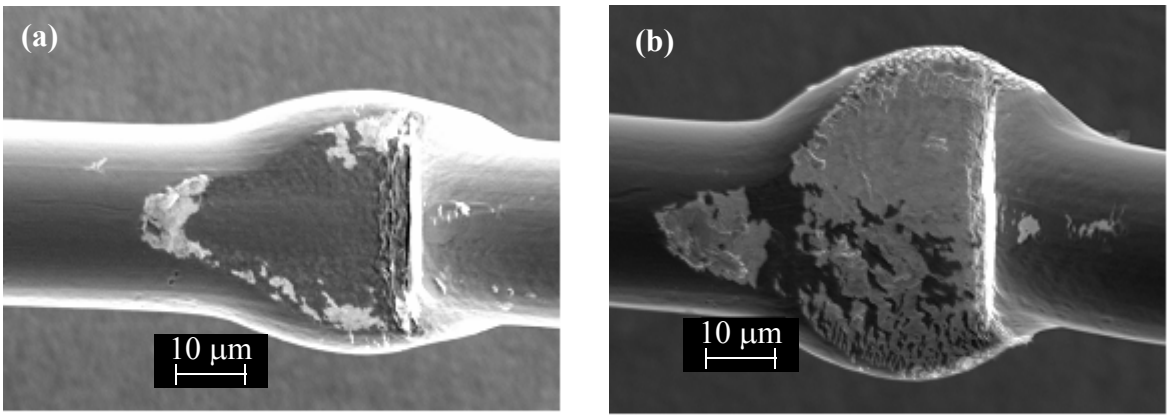

Fig. 3.14 SEM images of bottom of wire deformed with IF = 500 mN, US_C (a) 15%, (b) 50%. BF_C = 50 mN, BT_C = 25 ms, T = 220°C, shift = 0 µm. No bonding stage.

Comparing Fig. 3.14 (a) with Fig. 3.16 (a), it is obvious that the insulation layer is mostly broken by high IF at the periphery as shown in the SEM images of the bottoms of samples made with IF of 1200 mN and US_C of 15 % and 0 %, respectively. As US_C is increased to 50 %, the ultrasonic vibration enlarges the wire deformation and frictional wear as shown in Fig. 3.16 (b).

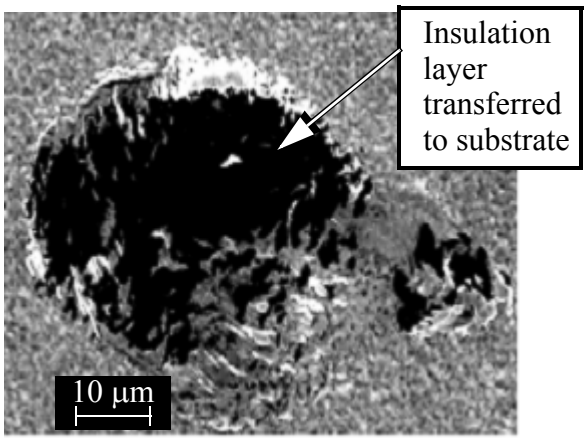

Fig. 3.15 SEM image of primary bonding site. IF = 500 mN, US_C = 50%, BF_C = 50 mN, BT_C = 25 ms, T = 220°C, shift = 0 µm. No bonding stage.

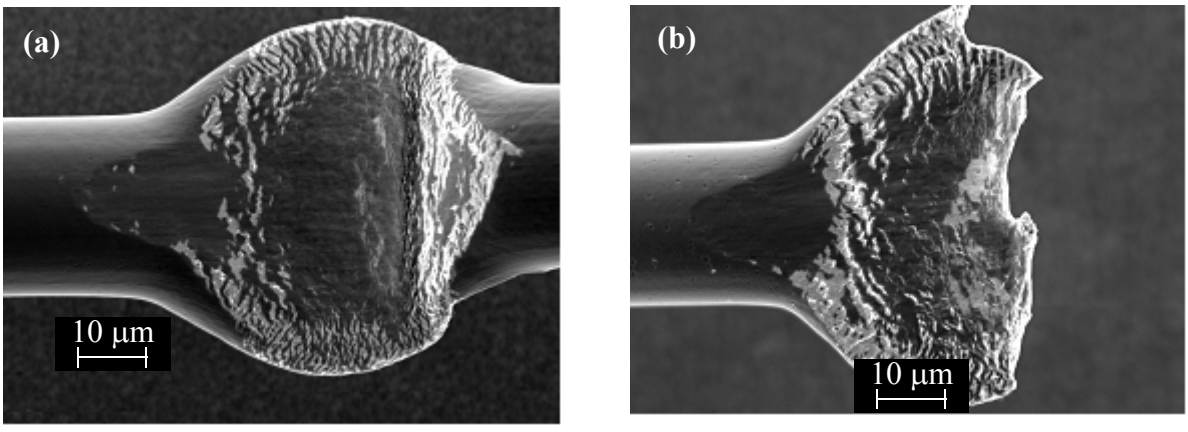

Fig. 3.16 SEM images of bottom of wire deformed with IF = 1200 mN and US_C (a) 15 % and (b) 50 %. BF_C = 50 mN, BT_C = 25 ms, T = 220 °C, shift = 0 µm. No bonding stage.

However, only little insulation transfer to the substrate is observed after using high IF, as shown on the primary bond location in Fig. 3.17.

Even with the shift of 20 µm, the bare wire portion of the insulated wire which will be bonded to the fresh substrate during the bonding stage is limited which may reduce the PF. Furthermore, the portion of tail bond which is the second loop of the BWW is already broken with US_C of 50 % as shown in Fig. 3.16 (b), which may result in premature tail breaking (short tail) during the bonding stage. It is concluded that US_C of 50 % with IF of 500 mN is a suitable set of process variables for the CS process.

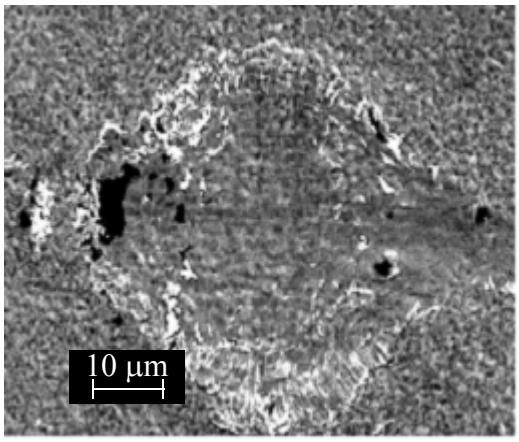

Fig. 3.17 SEM image of primary bonding site. IF = 900 mN, US_C = 50 %, BF_C = 50 mN, BT_C = 25 ms, T = 220 °C, shift = 0 µm. No bonding stage.

3.5 PF Results with CS

Results of confirmation runs with insulated Au wire with CS process and bare Au wire with the basic process are shown in Fig. 3.18. The parameters used are summarized in Table 3. The average ± standard deviation (σ) PF obtained with insulated wire and the CS process is 90.11 ± 7.87 mN, which is 2.4 ± 2.0 mN larger (95 % confidence level) than that obtained previously with bare wire and the basic process. The CS process PF improvement compared to the basic process with insulated wire is 26% ± 3%. Standard PF quality can be obtained with the CS process and insulated wire.

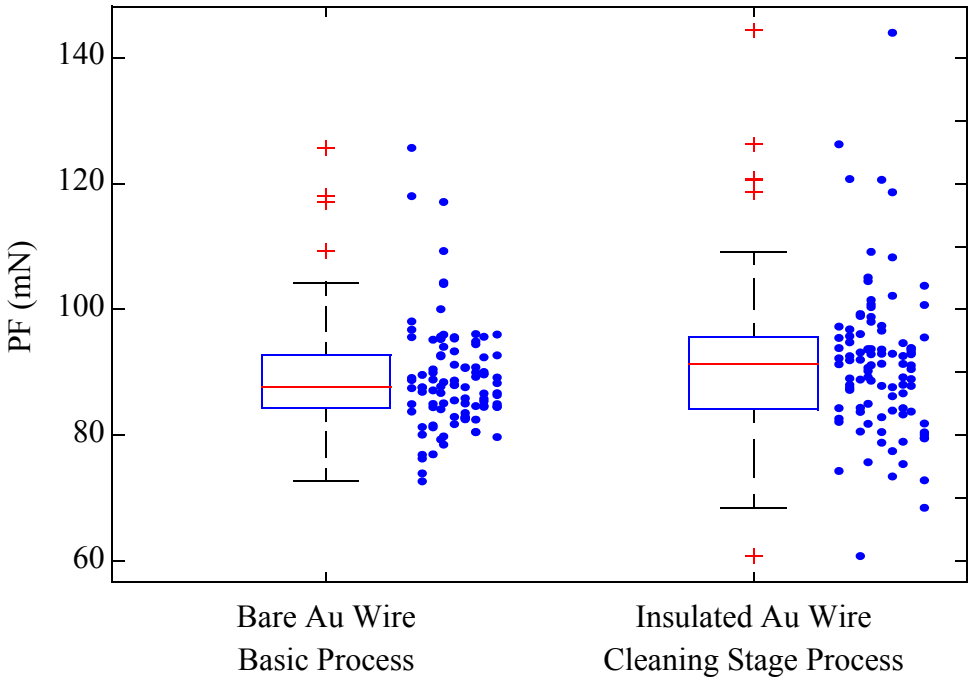

Fig. 3.18 Pull force comparison of crescent bonds with insulated Au wire bonded using basic process, and bare Au wire bonded using CS process.

Table 3. 3: Process Parameters for Comparison Experiment.

	Parameter Name	Value for modified process	Value for basic process
Impact	IF	500 mN	450 mN
Cleaning Stage	BF_C	50 mN	n/a
	US_C	50%	
	BT_C	25 ms	
	Shift	20 μm	
Bonding Stage	BF	500 mN	450 mN
	US	15%	15%
	BT	25 ms	25 ms

3.6 Tail Pull Force

3.6.1 Premature Tail Break

During the optimization process by iteration, EFO errors (or short tail) are observed as shown in Fig. 3.19. This is due to premature tail break. This may lead to a decrease in the stability of the crescent bonding process. Thus, the tail pull force (TPF) is measured at various US to investigate the effect of US on the TPF. During the TPF measurement, the tail bond made at the first crescent bond breaks as shown in Fig. 3.20. Figure 3.21 shows the tail pull force results at the third iteration of the crescent bond optimization. The TPF increases as the US increases from 10% to 20 %. It remains constant up to US of 45 % and then decreases. The maximum TPF obtained is 46.71 mN at US of 45 %. The TPF at the optimized parameter is 30.95 mN.

The TPF test with commercial pull tester is time consuming. Furthermore, during wire looping to the second crescent, the tail bond may be weaken due to the friction between the capillary and the wire and the bonding during the second looping process.

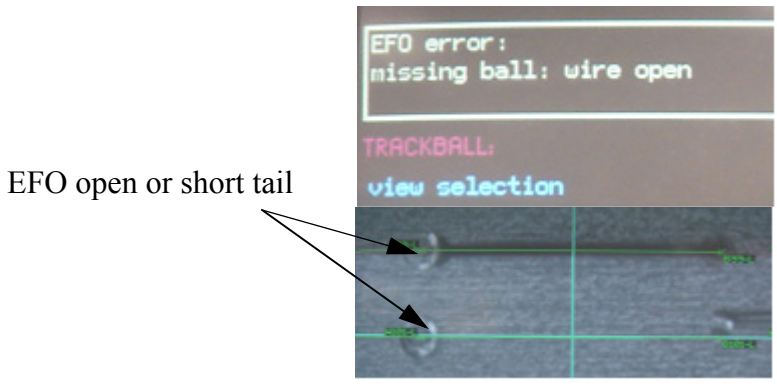

Fig. 3.19 Short tail error message displayed in the ESEC 3088 bonding machine.

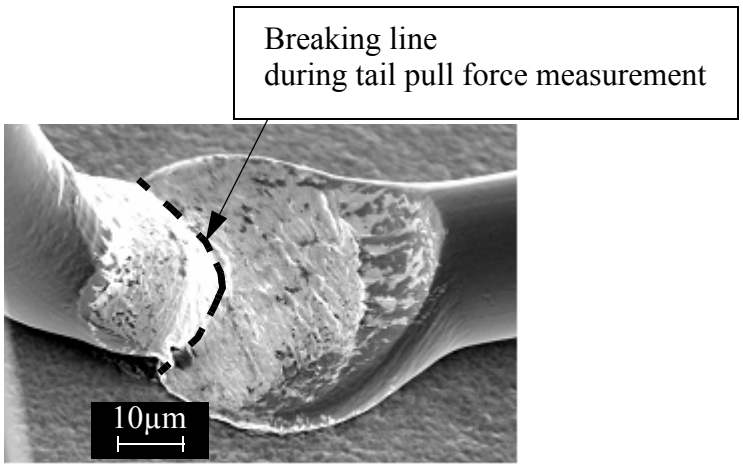

Fig. 3.20 SEM image showing the first (middle) crescent bond made during BWW bonding process.

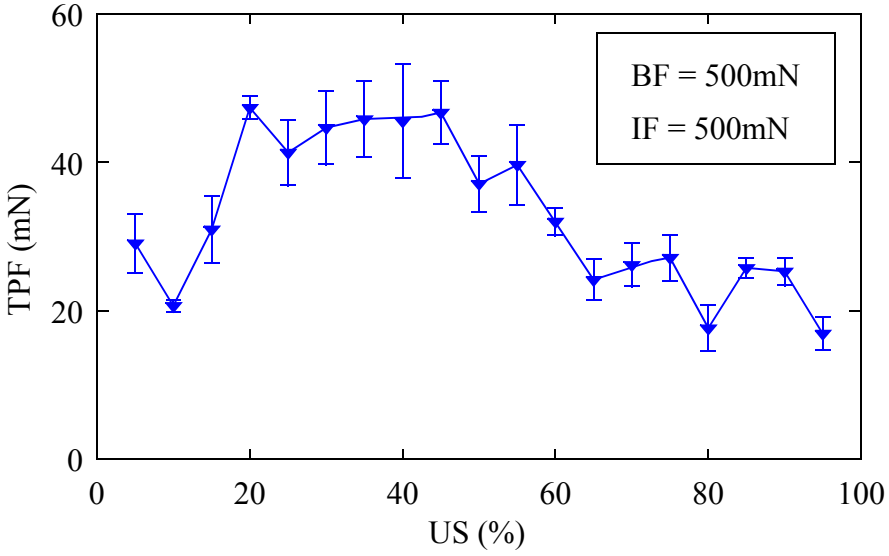

Fig. 3.21 Tail pull forces measured at third iteration of the crescent bond optimization at various US.

3.7 Summary

The feasibility of a modified bonding process is investigated in order to improve the crescent bond quality. The evolution of the crescent bond imprint morphologies left on the Ag leadframes is studied in detail with SEM to understand the effects of the bonding parameters on the insulation layer removal. The major findings from this study are summarized as follows:

- A basic bonding process used to bond bare Au wire on wire bonders, typically equipped with ultrasonic transducers operating at frequencies of 120 kHz and greater, is not sufficient to bond insulated Au wire yielding equivalent pull strengths.

- In a modified process with a cleaning stage, a combination of low impact force, ultrasound, and 20 μm shift can play a significant role in crescent bond formation and initiating the insulation removal of insulated Au wire.

- The average pull force with the cleaning stage before the basic bonding process is comparable to that obtained with bare Au wire.

Chapter 4 Cu Crescent Bonding Process Optimization and Understanding of Tail Bond Formation

In conventional wire bonding process optimization the crescent bond is tested by destructively pulling the loop and measuring the pull force (PF) required to break the bond. While this method assures the final quality, it does not necessarily minimize production stoppages which can reduce manufacturing throughput significantly. Many stoppages are caused by short-tail and tail-lift errors, caused by a reduced tail bond strength. A consistent tail breaking operation is needed for robust Cu wire bond production with little operator assistance required to restart stopped machines.

This chapter discusses an experimental study performed to understand tail bond formation in thermosonic Cu ball bonding process and its effect on the FAB formation. Using the TBF measurement method described in Chapter 2, a new concept to concurrently optimize the Cu crescent and tail bonding process is described in Chapter 4.1. In Chapter 4.2, tail bond formation with tail bond imprint is discussed.

4.1 Concurrent Optimization of Crescent and Tail Bonding Process

4.1.1 Experimental

An optimization process is developed in order to increase the robustness of tail bond with acceptable crescent bond strength, in which for simplicity all wire loops are made perpendicular to the ultrasound direction. The bonding parameters US, BF, and IF, BT, and T are varied to conduct a series of crescent bond optimization steps.

The second step is carried out to confirm the BT and T parameters which have been preselected earlier. Values for T are varied from 120 °C to 260 °C in 20 °C steps, and values for BF are varied from 7 ms to 41 ms in 2 ms steps. For each setting, 25 measurements are made. T is controlled using a thermocouple located inside the oven. On the heater, there is an about 1 cm thick heater plate adapted to the type of leadframes used. Thus, the bonding surface of the leadframes on the heater plate is an about 2 to 3 cm above the heater thermocouple. To estimate the ΔT between the bonding surface and T, temperature measurements with a thermocouple pressed to the centers of the heater plate and the heater (oven) without the heater plate show that the actual temperature of the diepad surface is approximately 20 K lower than T.

Third, process windows (PWs) for several responses are quantified and compared. To this end, 1800 loops are bonded distributed over more than 11 diepads. Figure 4.1. shows the bonding profile used for TBF measurement in order to minimize the diepad variations. A total of 200 bonds are made on a diepad. All five US levels and all 20 BF levels were used on each diepad,

resulting in all 1000 parameter combinations used on each diepad. Subsequently, responses are averages of data obtained from several diepads to minimize diepad-to-diepad variations.

During bonding of the rows, the occurrences of non-sticks are noted and the TBFs are measured. After bonding, the samples remain at high temperature on the bonder for three minutes. The bonded wire shape symmetry is evaluated using scanning electron microscopy (SEM). Top view micrographs are taken using the back scattered electron (BSE) method to obtain a clear contrast between wire and substrate metals as shown in Fig. 4.2 (a). A typical bonded wire deforma-

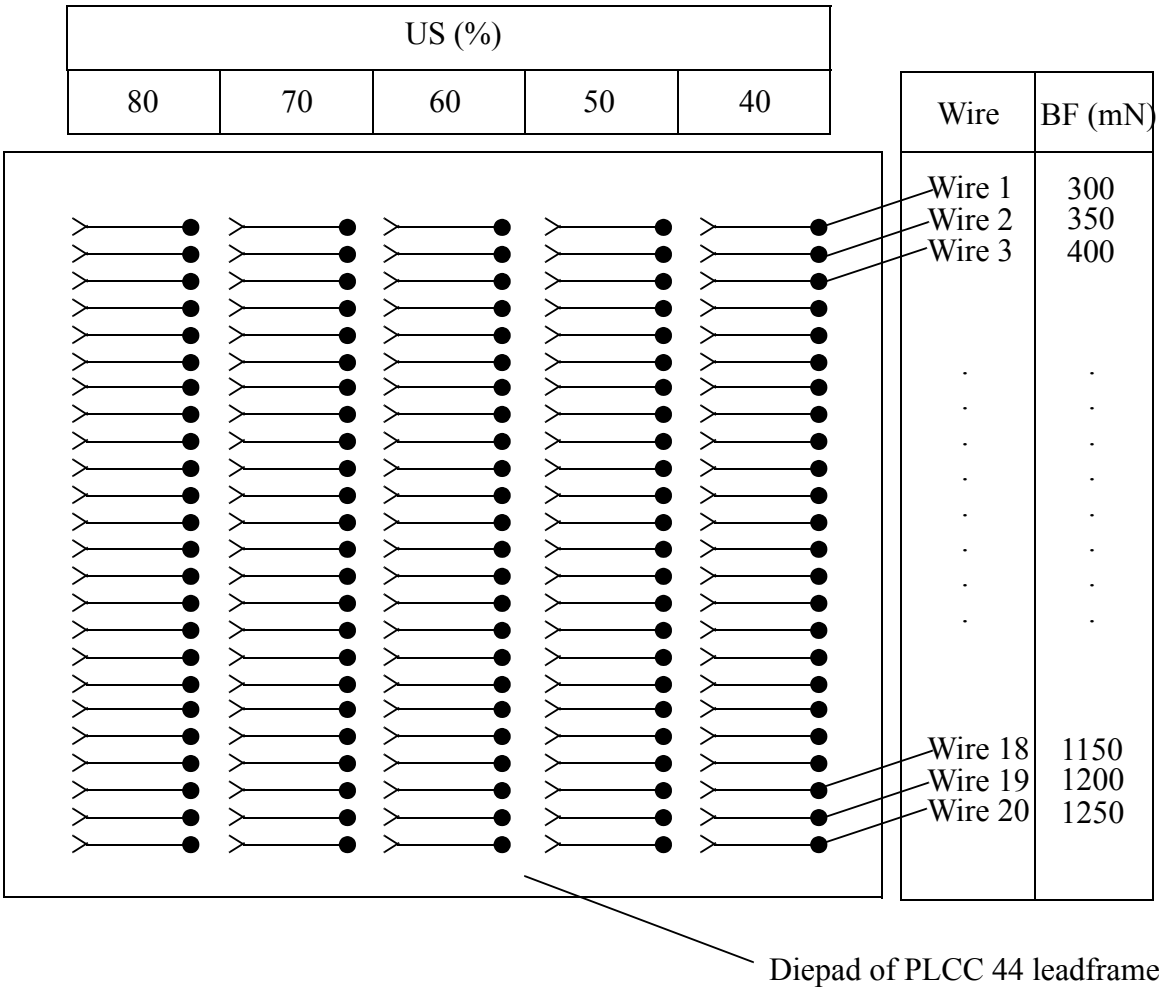

Fig. 4.1 Illustration of bonding profile used for concurrent optimization.

tion as measured at the location indicated by "α" is two wire diameters. To evaluate the PF, the bonded wires were pulled with a commercial tester. The pull speed was 200 µm/s. The pull hook was positioned at a location between first and second bond sites which is about 30% of the distance closer to the crescent bond. This assures the pull force value from the crescent bond is obtained. A total of 15 bonds for each setting are pulled.

The process capability index (cpk) [22] is an indication of the ability of a process to produce output with specification limits. For the present application, it is defined using

$$cpk = \frac{\overline{PF} - LSL}{3\sigma} \tag{4.1}$$

where $\overline{PF}$ is the average PF, LSL is the lower specification limit, and σ is the standard deviation. Values of cpk are determined for PF using LSL_{PF} = 24 mN, a limit determined using a standard limit for Au wire bonds and assuming the maximum angle between wire loop and substrate during pulling is about 60° [20]. For TBF, the cpk values are calculated using LSL_{TBF} = 10 mN, a limit below which the tail might not hold firmly.

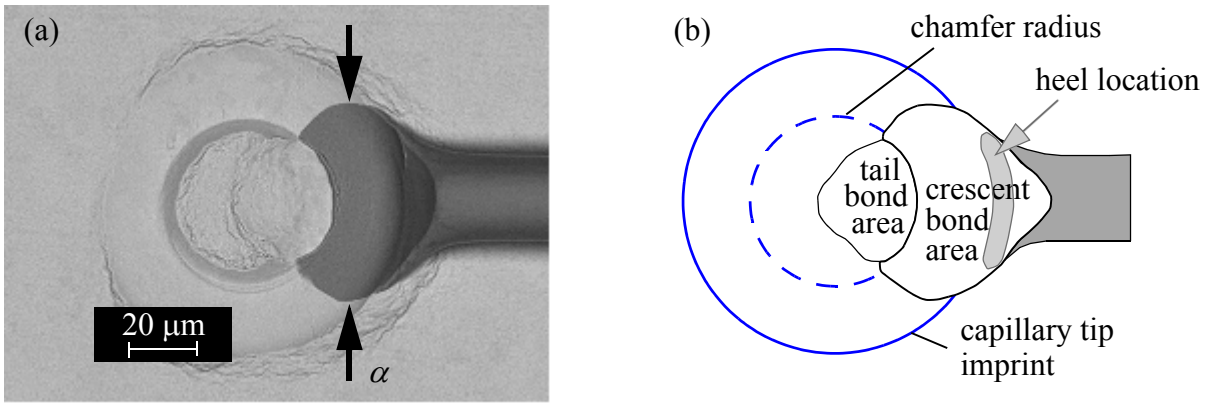

Fig. 4.2 Example crescent bond. (a) BSE-SEM micrograph and location of deformation measurement. (b) Area definitions for tail and crescent bonds.

4.1.2 Results and Discussion

4.1.2.1 T and BT effect on PF and TBF

The effects of BT on TBF and PF are shown in Fig. 4.3. It is observed that the longer the BT, the higher TBF, but the lower PF. Hence, a trade-off between TBF and PF quality is required when choosing BT while keeping in mind a shorter BT means higher throughput. In this study, a BT of 25 ms is selected.

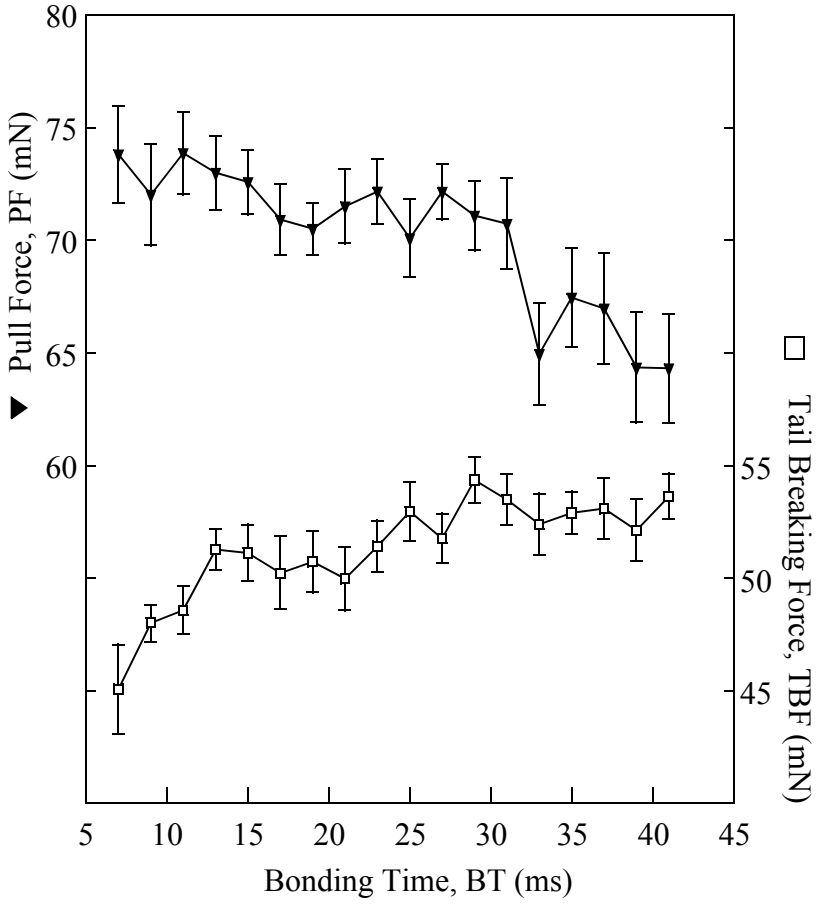

Fig. 4.3 PF and TBF measured for various ultrasonic bonding times. T = 220 °C. IF = 1000 mN. US = 63%. BF = 450 mN.

The effects of T on TBF and PF are shown in Fig. 4.4. Both TBF and PF mainly increase with T with a rate that is highest between 200 °C and 220 °C. A reason for this high rate is the fact that AgO decomposes at temperatures of 200 °C and higher [82]. The highest values of PF and TBF occur with T values of 220 °C and higher, ie. temperatures on the diepad are expected in the range in which Ag oxide decomposes. A value of 220 °C is selected for the other experiments in this study.

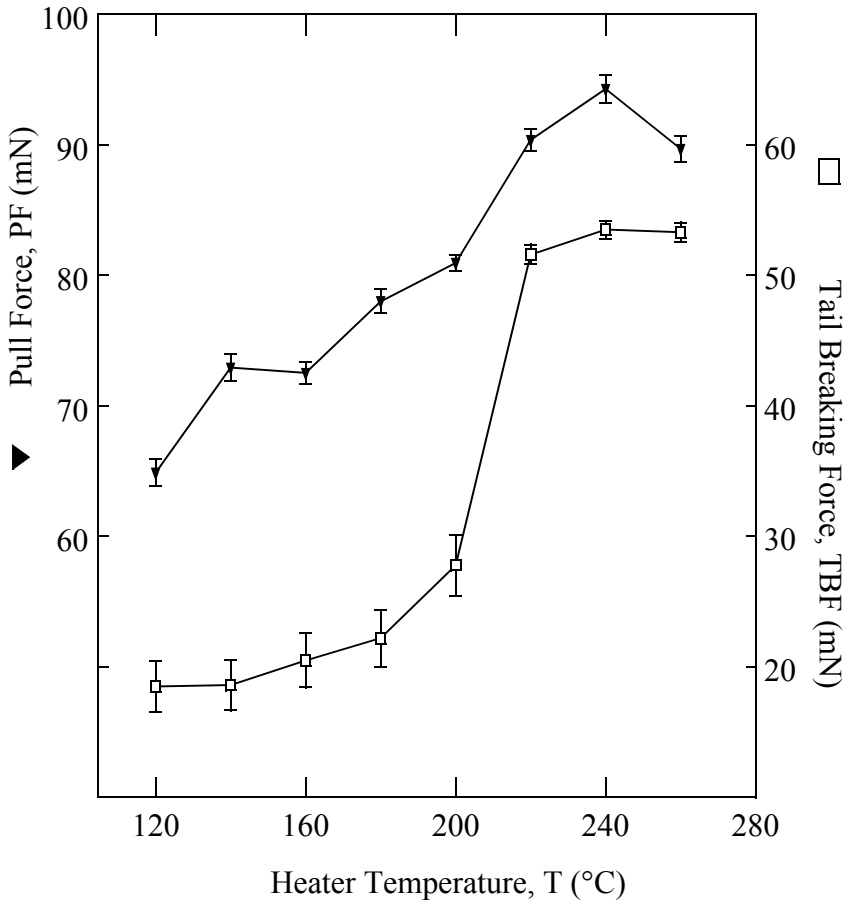

Fig. 4.4 PF and TBF measured for various values of the heater temperature (T). BT = 25 ms. IF = 1000 mN. US = 63%. BF = 450 mN.

4.1.2.2 US/BF Process Windows

The occurrence of non-sticks and the symmetry of the bonded wire shape are considered basic process quality indicators. The US/BF parameter combinations for which these indicators are found acceptable are shown as shaded area in Fig. 4.5. The open squares indicate the settings tested as indicated in Fig. 4.1.

Non-sticks are crescent bonds lifted off if US is too low, eg. from region A in Fig. 4.5. Examples of wires that did not stick are shown in Fig. 4.6 (a), indicating wires broken away from the second bond site and bent upwards. The formation of such shapes is illustrated in Figs. 4.7 (a), (b), and (c). After bonding the crescent bond as illustrated in Fig. 4.7 (a), the open wire clamp moves up together with the capillary to thread out the length of wire required as a tail. Then, the

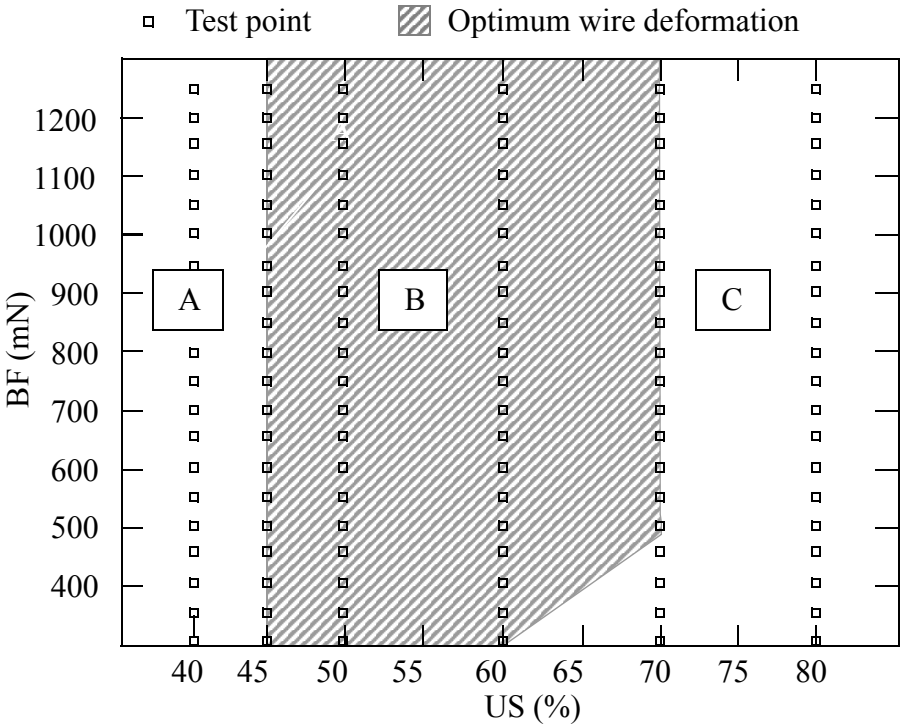

Fig. 4.5 US/BF process window for wire deformation. IF: 1000 mN; BT: 25 ms; T: 220 °C.

movement stops for a moment to allow for the wire clamp to close. The movement resumes upwards intended to break the tail bond only but fails due to the crescent bond lift off as shown in Fig. 4.7 (b). The electronic lift-off detection system has been disabled for this study, so the movement continues up to the EFO position. Figure 4.7 (c) illustrates how the wire is stretched until it breaks at the location where it has been weakened during crescent bonding. The bonded wire springs back to a shape shown in gray resulting from the looping and crescent bond operations. The remaining tail is bent away from the capillary axis as shown in Fig. 4.7 (d). EFO produces a ball and then the clamp opens, but the bend in the wire prevents the wire from being completely pulled up as illustrated in Fig. 4.7 (e), so the ball is not properly placed at the capillary tip. Therefore, the subsequent ball bond operation squeezes the bent wire sideways while the FAB hangs out of the bonding zone as illustrated in Fig. 4.7 (f).

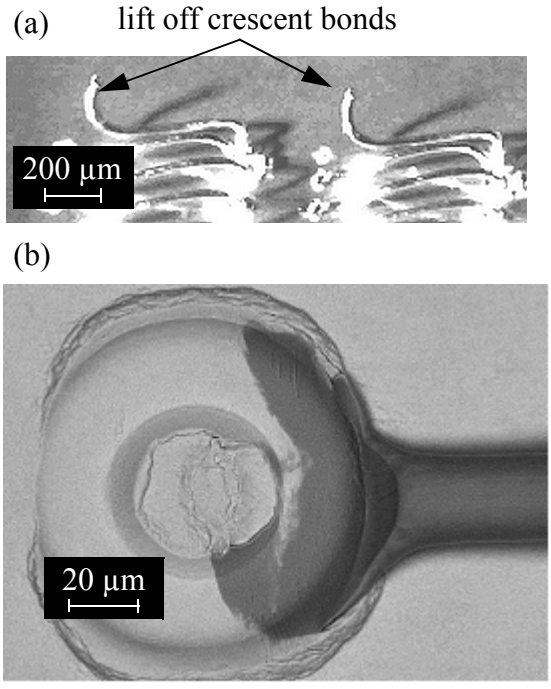

Fig. 4.6 Defective crescent bonds: (a) Lift off. (b) Excessive wire deformation.

An acceptable deformation which is 1.5 that of an acceptable shape. Such bonds are obtained with settings from region C in Fig. 4.5. In Fig. 4.6 (b), tail residue remains within the chamfer area which can indicate a high TBF. However, such bonds have suboptimal PF and distort the wire loop.

Advanced process quality indicators are PF and TBF. Figure 4.8 (a) shows the contour plot of the average PF obtained for the settings tested. For high values of US the PF decreases, possibly caused by ultrasonic fatigue, indicated by all bonds breaking at the heel as defined in Fig. 4.2 (b). The highest PF is 89.1 mN, obtained with 50 % and 500 mN of US and BF, respec-

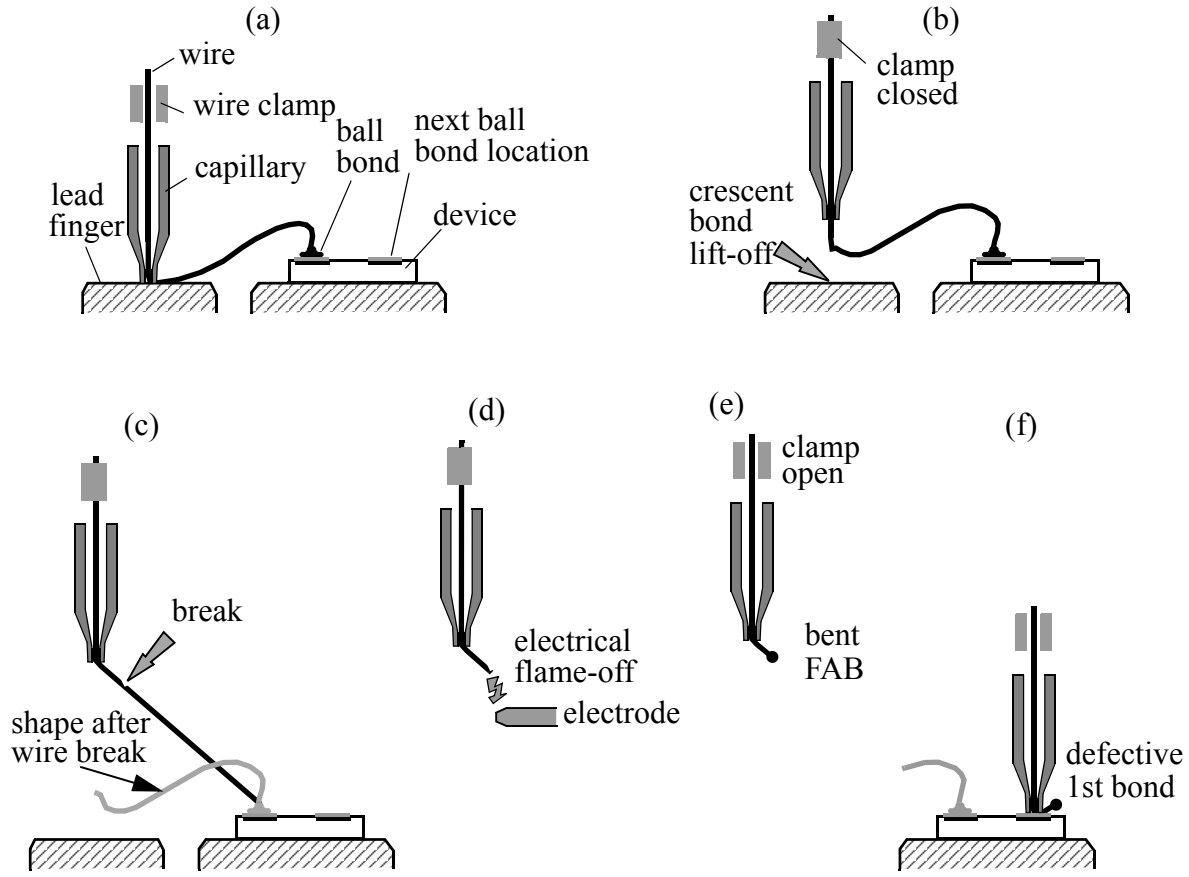

Fig. 4.7 Illustrations of non-stick event. (a) crescent bonding deforms wire, (b) tail breaking also breaks crescent bond, (c) tail extends and breaks where deformed, (d) tail end bent sideways, (e) ball formed and (f) first bond defect.

(a)

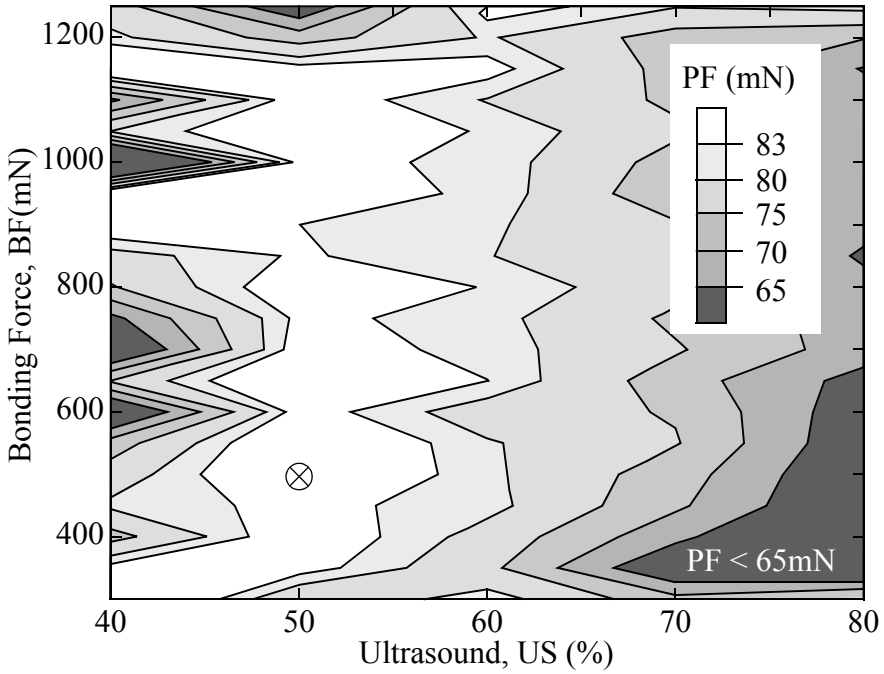

(b)

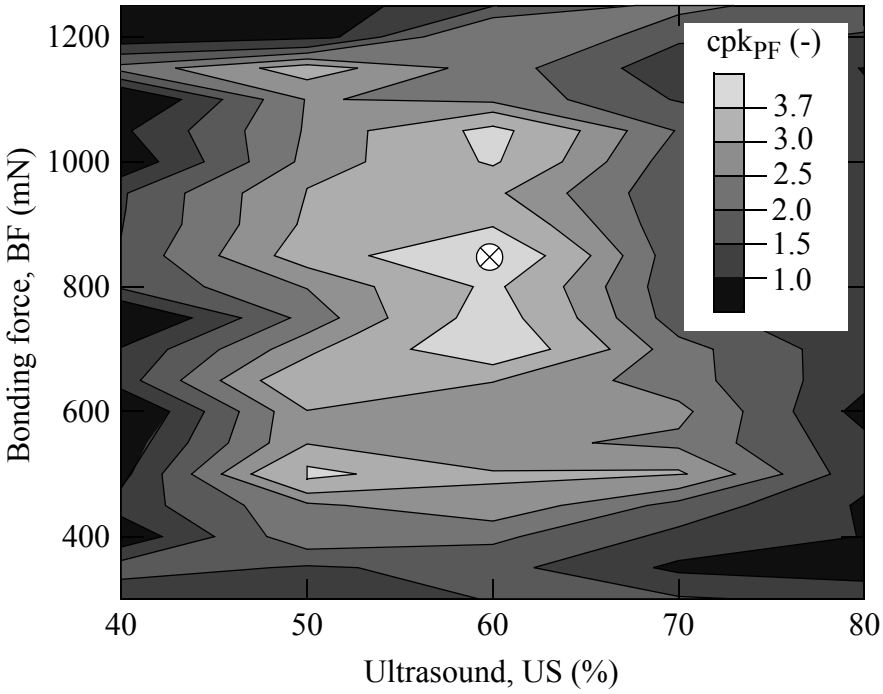

Fig. 4.8 Contour plot of (a) PF and (b) cpk$_{PF}$. IF: 1000 mN; BT: 25 ms; T: 220 °C. Highest value marked by cross ⊗.

tively. Figure 4.8 (b) shows the cpk_{PF} contour plot obtained with the PF data. The highest cpk_{PF} is 4.51, obtained with 60 % and 850 mN of US and BF, respectively.

Figure 4.9 (a) shows the contour plot of the average TBF. The highest average TBF is 55.5 mN, obtained with 500 mN and 70 % of BF and US, respectively. Figure 4.9 (b) shows the contour plot of cpk_{TBF}. The highest value of cpk_{TBF} found is 3.94, obtained with 400 mN and 60 % of BF and US, respectively.

4.1.2.3 Combined PWs

To propose settings for production, we require cpk = 2 for both, PF and TBF in this example process. The optimized settings are found in a combined PW, defined by the intersections shown in Fig. 4.11. The largest of these intersections can be found at relatively low levels of BF. Smaller intersection are in the top left corner. The largest possible ellipse fitted inside this combined PW covers a bit less than 100 mN in the BF dimension, but more than 10 % in the US dimension. The suggested working point in the ellipse center is US = 57 % and BF = 430 mN.

For this concurrent optimization, the BF parameter turns out to be more sensitive than in a conventional PF only optimization. For a detailed analysis, the PF & TBF cpk data is shown for US = 60% in Figs. 4.10 (a) and (b), respectively. The cpk errorbars are calculated using Eqn. (2.3) [65]. Only for BF = 450 mN, both the PF and the TBF cpk are well above 2.

It is suggested to repeat the described procedure with different samples of capillaries and on different wire bonder to validate these results, as well as to obtain optimized parameters for wire loops oriented in and opposed to the horn direction.

(a)

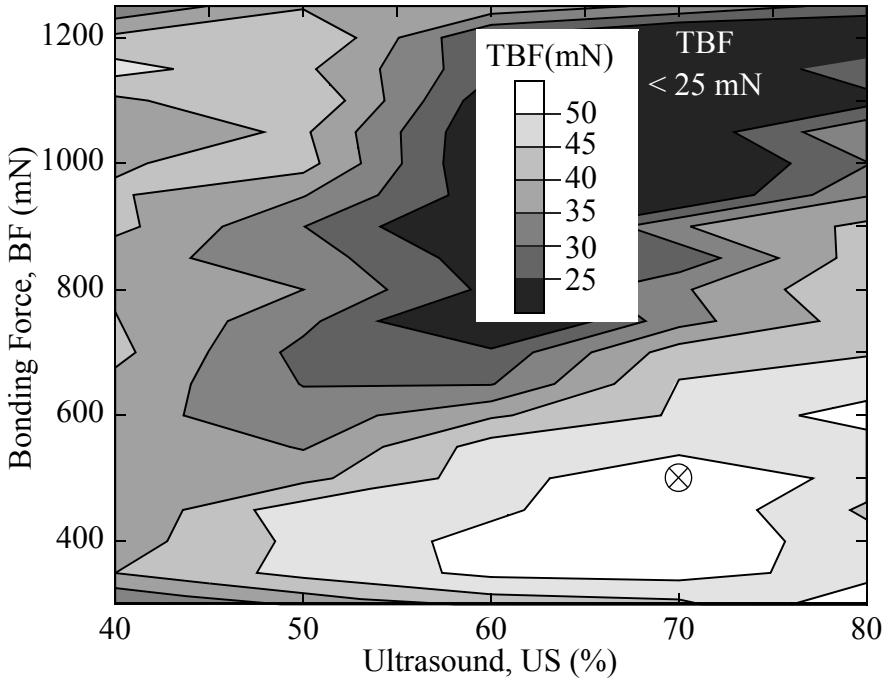

(b)

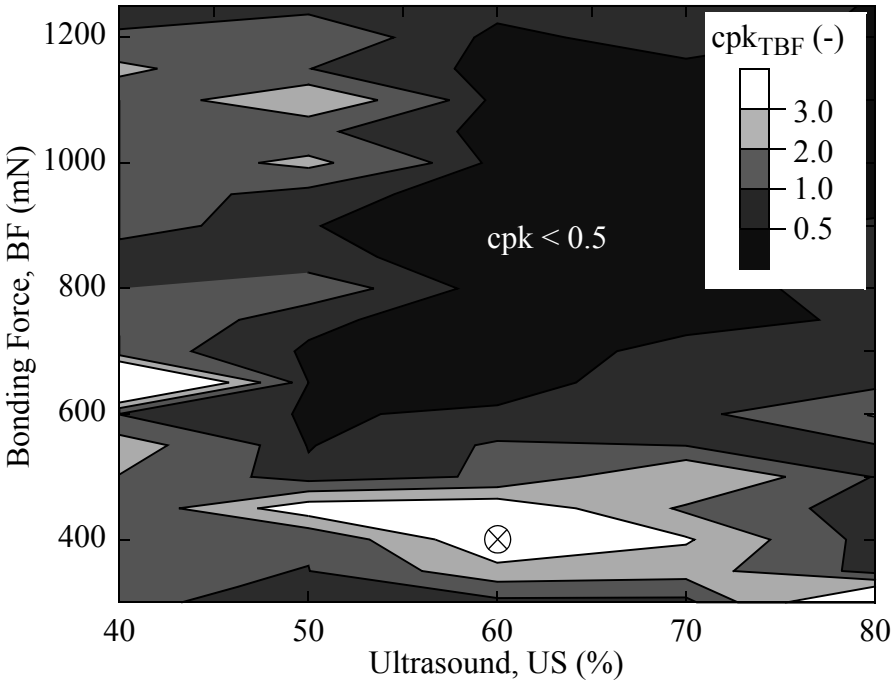

Fig. 4.9 Contour plot of (a) TBF and (b) cpk$_{TBF}$. IF: 1000 mN; BT: 25 ms; T: 220 °C. Highest value marked by cross ⊗.

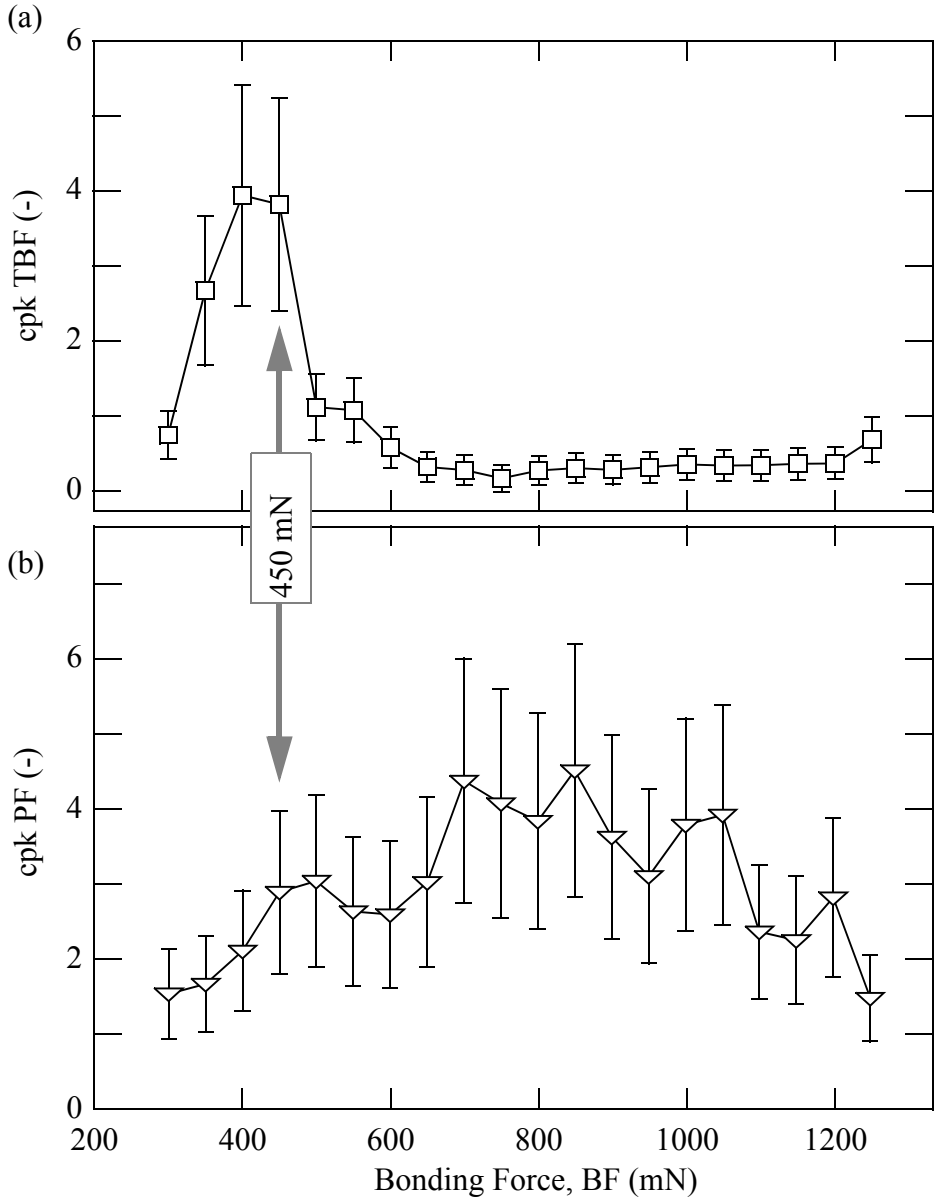

Fig. 4.10 Cpk values measured with US = 60% vs. BF for (a) TBF and (b) PF.

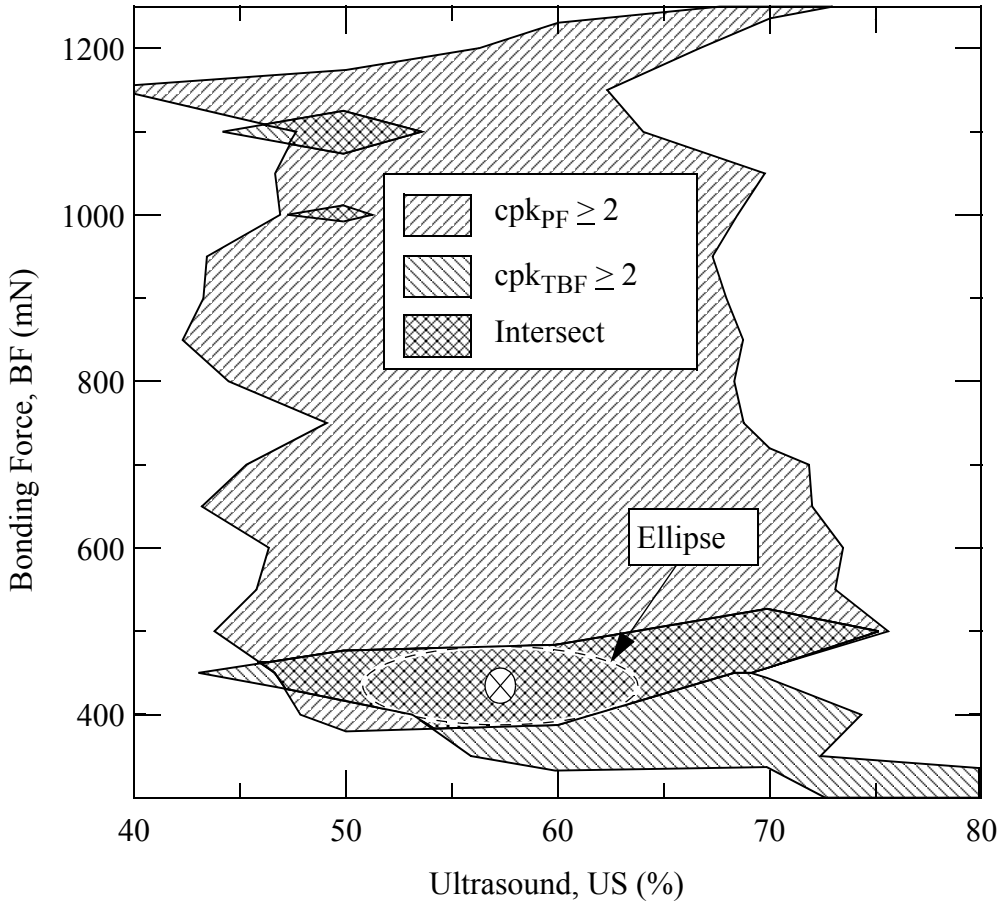

Fig. 4.11 PWs intersection. ($cpk_{PF} > 2.0$, $cpk_{TBF} > 2.0$). Suggested working point marked by a cross ⊗.

4.2 Tail Bond Imprint Study

4.2.1 Experimental

In order to obtain uniform FABs for stable ball bonding, a forming gas mixed with 5 %H_2 + 95 %N_2 at the gas flow rate of 0.5 l/m is used. The tail bond strength is optimized with the online TBF measurement described in Chapter 2. The bonding parameters varied for the iteration are US, IF, and BF, while BT and T are 25 ms and 220 °C, respectively. The maximized TBF is obtained with US, IF, and BF of 80 %, 1100 mN, 500 mN, respectively. These parameters are called *optimized parameters* in the following.

Figure 4.12 shows an illustration of the study carried out. Two type of responses, (1) tail bond imprint structure and (2) TBF, are obtained with various process settings and their correlations are

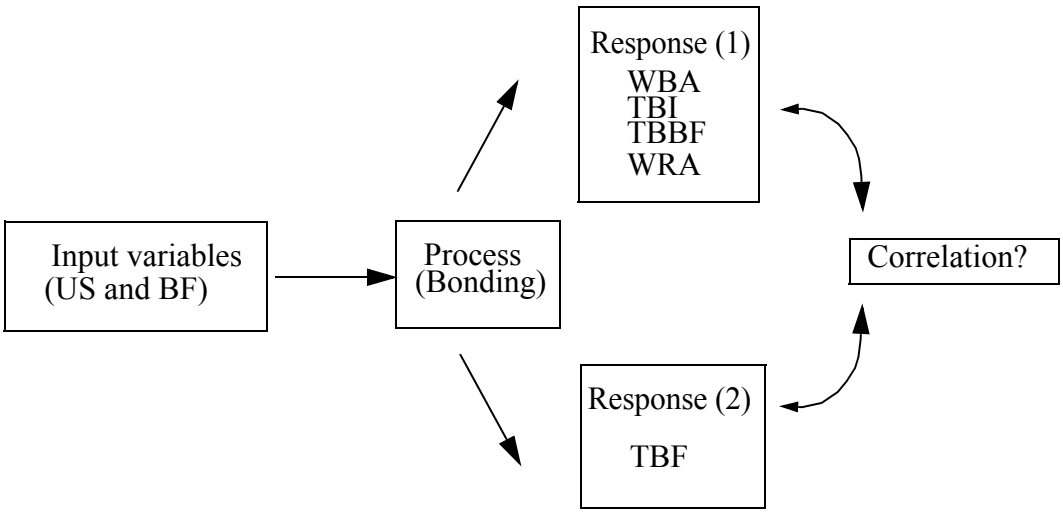

Fig. 4.12 Schematic overview of the investigation.

investigated. The effect of IF on TBF with Au wire is less than that of the parameters US and BF as shown in Fig. 2.12. Therefore, US and BF are chosen to be investigated in this study.

Wire bonds are made on the diepad. To remove the diepad variation previously reported in Fig. 2.19, five different diepads from five different strips are selected for each bonding. A total of 20 TBFs are measured to obtain reliable results. Each sample size for WBA, TBI and TBBF is 10. Backscattered electron (BSE) and energy dispersive X-ray (EDX) are used to distinguish the element distribution and quantify the content of Cu, respectively, on the tail bond imprint.

4.2.2 Tail bond imprint structure defined by distinct areas

Several areas in the imprint of the tail bond are identified and described in this section. A typical imprint of the tail bond is shown in Fig. 4.13 (a). Four different tail bond areas (TBAs) are observed as indicated by the numbers 1, 2, 3, and 4. These areas are defined as

1. wire residue area (WRA),
2. wire breaking area (WBA),
3. area characterized by increase surface wear, formed by the combined action of ultrasound (US), bonding force (BF), and impact force (IF), resulting in a relatively strong bond contributing to the *breaking force* (TBBF), and
4. tail bond imprint area formed with impact force (TBI), respectively.

The areas are illustrated in Fig. 4.13 (b). The TBI area includes TBBF, WBA, and WRA. The TBBF area includes WBA and WRA. The WBA and WRA areas are not overlapping. The outer circle in Fig. 4.13 (b) reflects the chamfer diameter, 51 μm, and the inner circle (marked by B) indicates surface mark formed by the chamfer during the process.

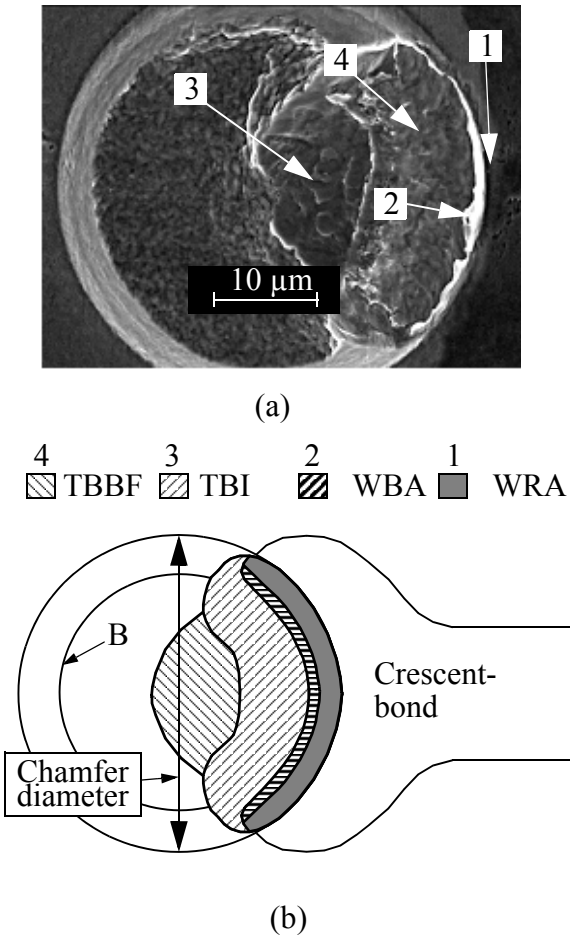

Fig. 4.13 (a) SEM image of a typical tail bond imprint and (b) schematic of tail bonded area definition.

4.2.3 Results

4.2.3.1 Influence of Bonding Parameters on Tail Bond Areas

The tail bond imprint structure is expected to depend on process parameters such as US and BF, as do the bond strengths of Au ball bonds [83, 84] and Au crescent bonds [28, 27]. Figure 4.14 shows that US does not influence TBI much as it remains in the range of 650 μm^2 to 750 μm^2. Figure 4.15 similarly shows that the TBI remains within an even tighter range for various BF values. However, TBBF depends strongly on BF for parts of the range shown. The values of TBBF depend much less on US, remaining in the range of 350 μm^2 to 480 μm^2.

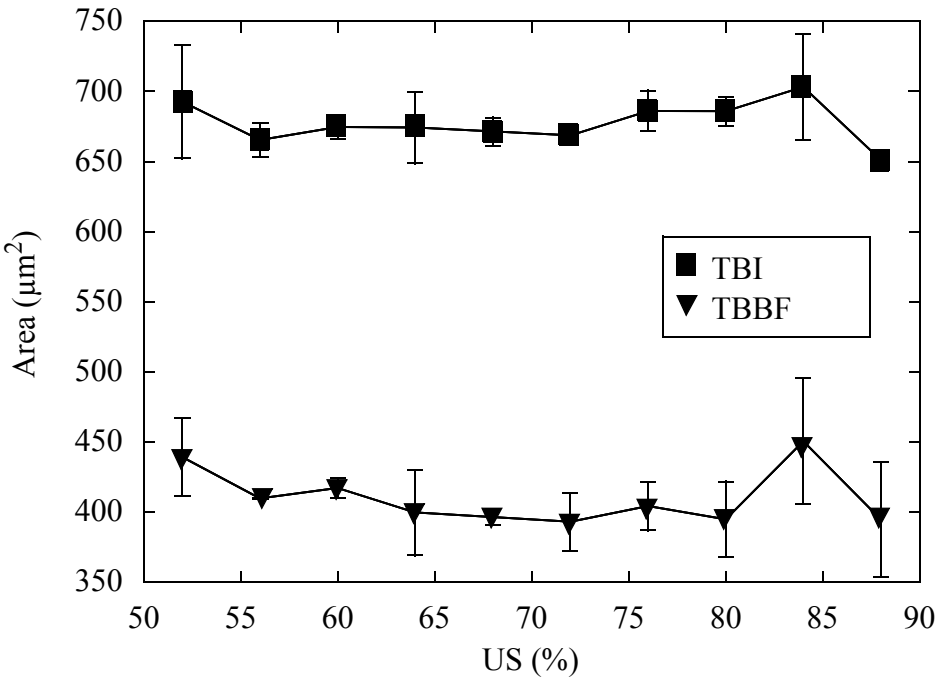

Fig. 4.14 TBI and TBBF vs. US. IF = 1000 mN, BF = 500 mN, BT = 25 ms, T = 220 °C.

In the case of various BF values, the TBBF shows two different stages, A and B as indicated in Fig. 4.15. The increase of TBBF is as large as 1.07 μm^2/mN in stage A (300 mN to 500 mN) and 0.09 μm^2/mN in stage B. To find an explanation for the transition between the stages, two SEM images of imprints with BF of 300 mN and 500 mN are shown in Fig. 4.16 (a) and (b), respectively. The TBBF does not reach to the edge of TBI with BF of 300 mN as shown in Fig. 4.16 (a) while it does with BF of 500 mN as shown in Fig. 4.16 (b) and with all other imprints made with higher BFs.

An explanation for stage A is not fully known. More ultrasound enhanced wire deformation [60] can take place with BF = 500 mN compared to BF = 300 mN, resulting in the TBBF reaching to the edge of TBI. For BF > 500 mN, no further deformation occurs, resulting in slowing the TBBF growth with BF in stage B.

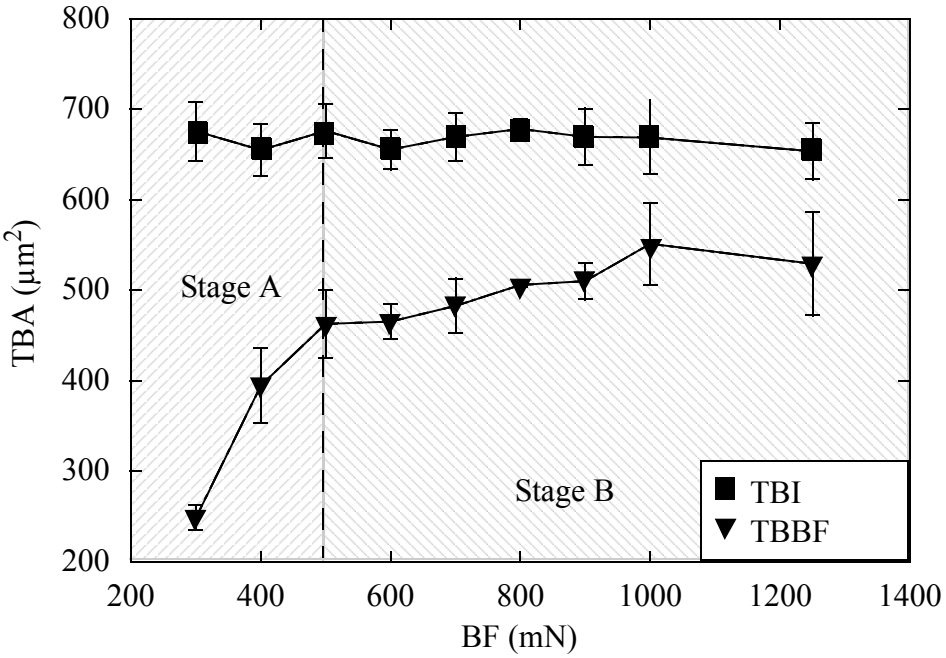

Fig. 4.15 TBI and TBBF vs. BF. IF = 1000 mN, US = 72 %, BT = 25 ms, T = 220 °C.

4.2.3.2 TBF and Tail Bond Areas

The comparisons of TBF, WBA, and WRA obtained with various US and BF are shown in Fig. 4.17 and Fig. 4.18, respectively. With US variations as shown in Fig. 4.17, the TBF, the WBA, and the WRA increase as US increases up to 80%. With US further increasing, WBA and WRA continues to increase while TBF decreases. In case of BF, the change of the TBF is similar

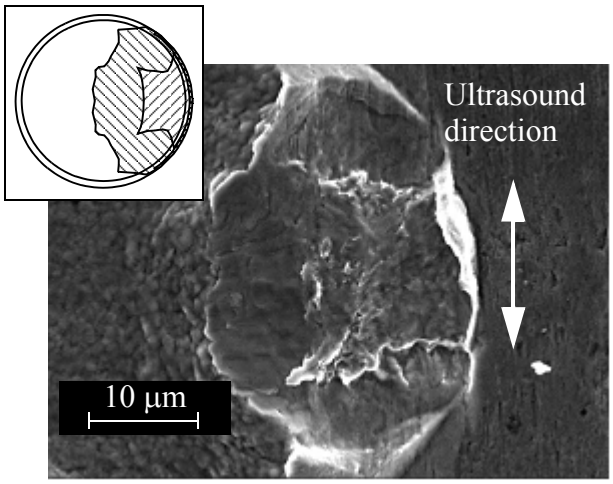

(a)

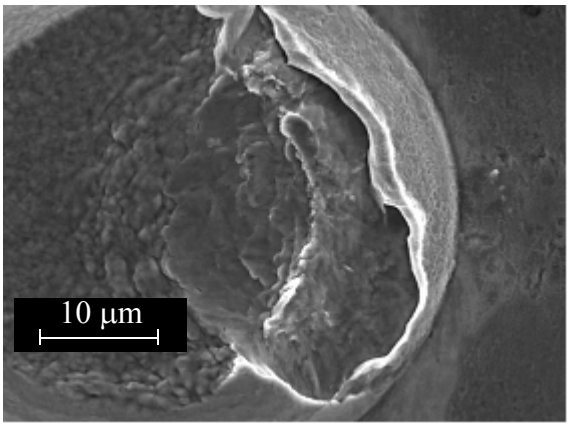

(b)

Fig. 4.16 SEM images of tail bond imprints made with BF of (a) 300 mN and (b) 500 mN. IF = 1000 mN, US = 72 %, BT = 25 ms, T = 220 °C.

to that of WBA. The errors of WBA are larger with low BF than with high BF (Fig. 4.18). No correlation between the TBF and the WRA is found.

4.2.3.3 The Effects US and BF on Interface Morphology and Composition

The tail bond imprints are studied with SEM after wire pull test. Figures 4.19 (a) - (c) show SEM micrographs of imprints obtained with US of 52 %, 60 %, and 72 %, respectively. With US = 52 %, no fracture residues on TBBF are observed in Fig. 4.19 (a), only Cu residues remain at the edge of the crescent bond but not in the center, indicating an insufficient bond. As US increases to 60 %, fracture residue islands are observed at the edge of the TBBF as shown in Fig.

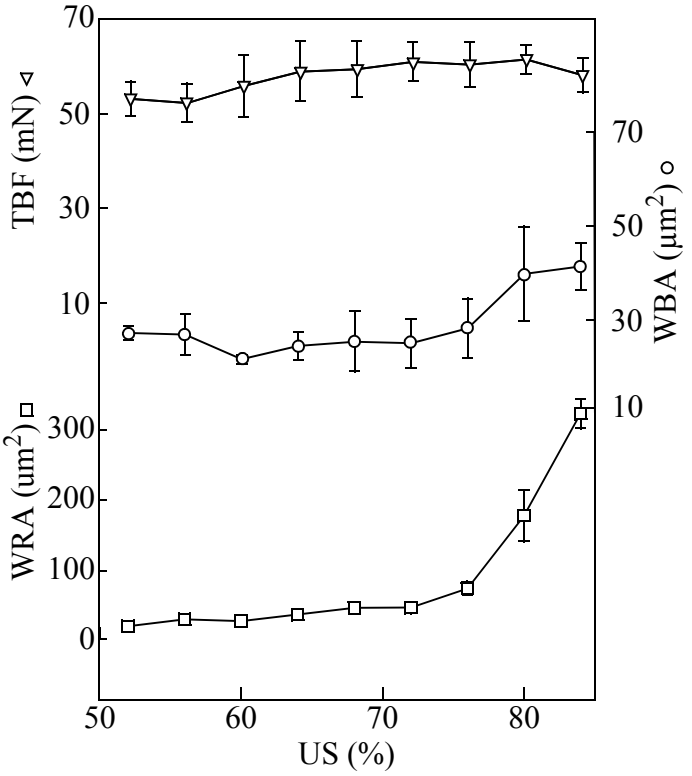

Fig. 4.17 TBF, WBA, and WRA vs. US. IF = 1000 mN, BF = 500 mN, BT = 25 ms, T = 220 °C.

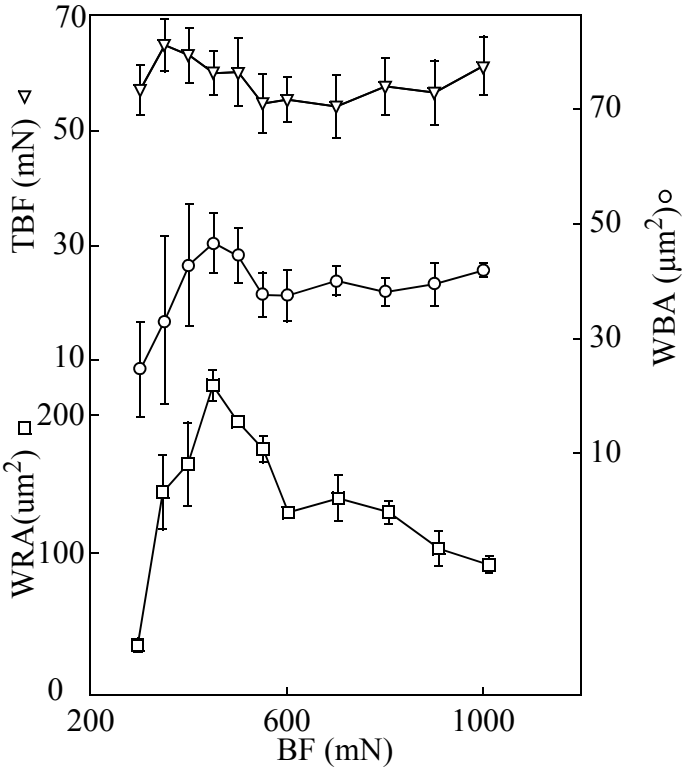

Fig. 4.18 TBF, WBA, and WRA vs. BF. IF = 1000 mN, US = 72 %, BT = 25 ms, T = 220 °C.

4.19 (b). With US = 72 %, a fracture line indicated by B in Fig. 4.19 (c) was developed inside TBBF. The fracture line is about 9 μm inside of the capillary chamfer. BSE image of the tail like that in Fig. 4.21 show that the fracture did not occur in the wire. Ag diepad is fractured and Ag residue is attached on the bottom of the wire tail. No residue of Cu is found, but a grey shade along the line D in Fig. 4.20.

In order to identify the composition of the grey line observed in BSE image in Fig. 4.20, EDX line scanning is performed starting from the border between crescent and tail bond extending in wire direction as shown in Fig. 4.22. The results are shown in Fig. 4.23. It is found that the grey line is Cu. The highest Cu contents are detected at around 9 μm from point E. As US increases from 52 % to 80 %, the highest Cu contents obtained increases from 10 at% to 40 at%. The Cu

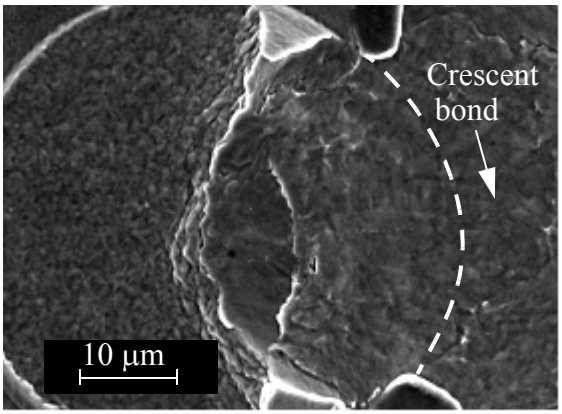

(a)

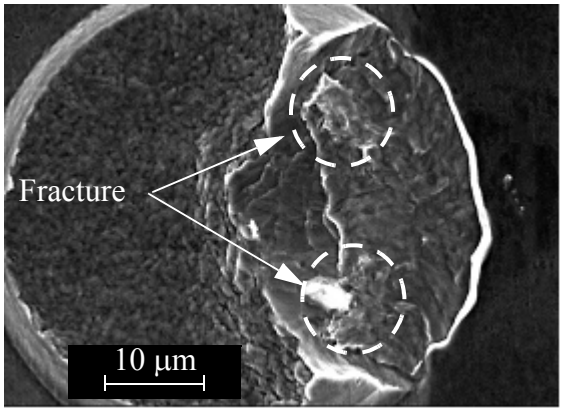

(b)

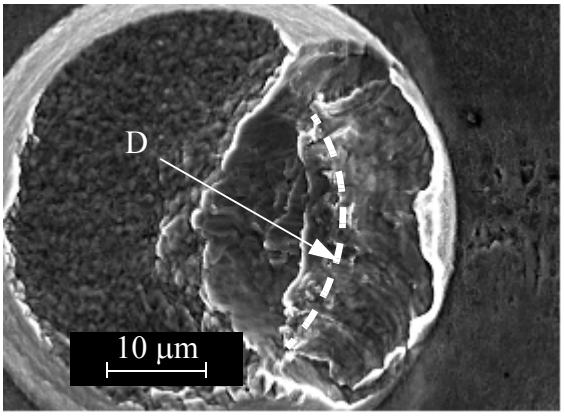

(c)

Fig. 4.19 SEM images of the imprint of TBA at US of 52 %, (b) 60 %, and (c) 72 %. IF = 1000 mN, BF = 500 mN, BT = 25 ms, T = 220 °C.

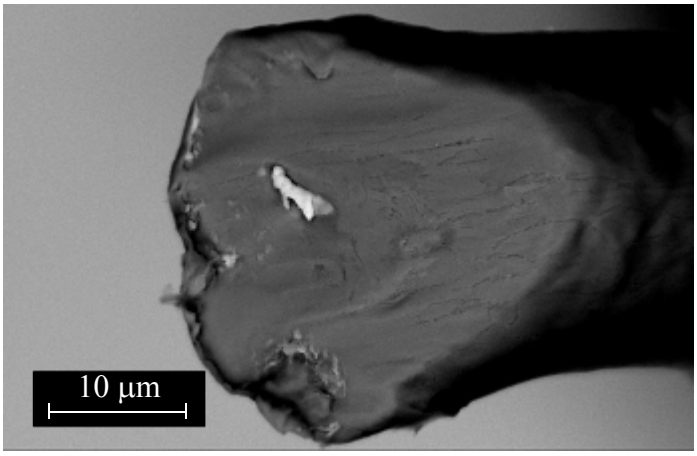

Fig. 4.21 BSE image of the bottom of wire tail after tail breaks.

contents on the other portion of TBA is around 10 at%. Cu has diffused into the Ag diepad during the tail bonding process.

The effect of bonding force on interface morphology and composition is studied. Figures 4.24 (a) and (b) are BSE images showing the tail bond area obtained with BF of 300 mN and 1000 mN, respectively. With the lower BF, no trace of Cu is apparent on the TBBF. As BF increases to

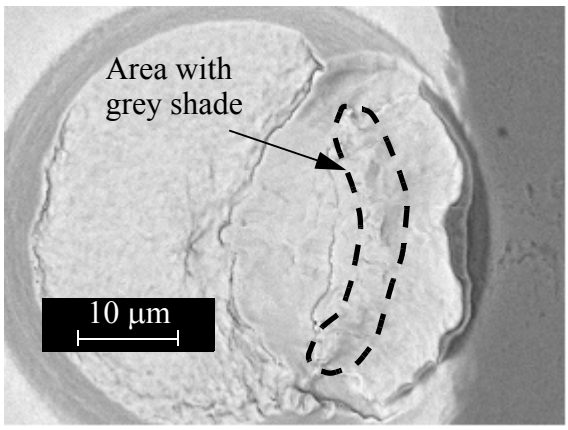

Fig. 4.20 BSE image of the imprint of TBA with US of 72 %. IF = 250 mN, BF = 500 mN, BT = 25 ms, T = 220 °C.

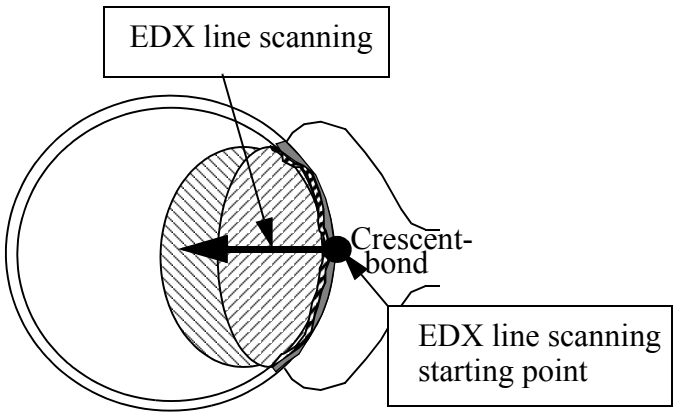

Fig. 4.22 Schematics of EDX line scanning.

1000 mN, a grey line of Cu, indicated by γ, is observed which is located at around 10 μm away from the chamfer imprint.

To confirm the change of Cu contents with BF changes, EDX line scannings are carried out along a line like that shown in Fig. 4.22. The results are shown in Fig. 4.25. With BF = 300 mN, no significant changes of Cu contents in TBBF are observed. With BF = 600 mN, a maximum of 38 at% of Cu is found. With BF = 1000 mN, the area where Cu is detected has expanded toward the crescent bond. The highest amount of Cu detected is about 83 at%.

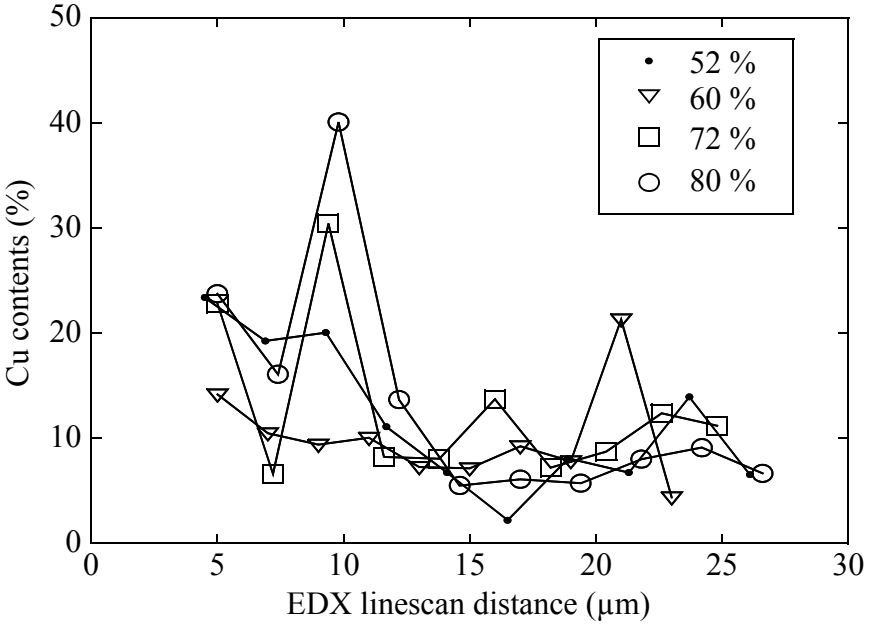

Fig. 4.23 Cu contents change obtained with EDX as US increases. IF = 1000 mN, BF = 500 mN, BT = 25 ms, T = 220 °C.

4.2.4 Discussion

4.2.4.1 Influence of US on tail bond growth

The tail bond formation kinetics with respect to rising ultrasound parameters is discussed using Figs. 4.19 (a), (b), and (c). With low US, only deformation in the TBBF is observed (Fig. 4.19 (a)). As US is increased, the fractures start at the periphery of the TBBF (Fig. 4.19 (b)), and

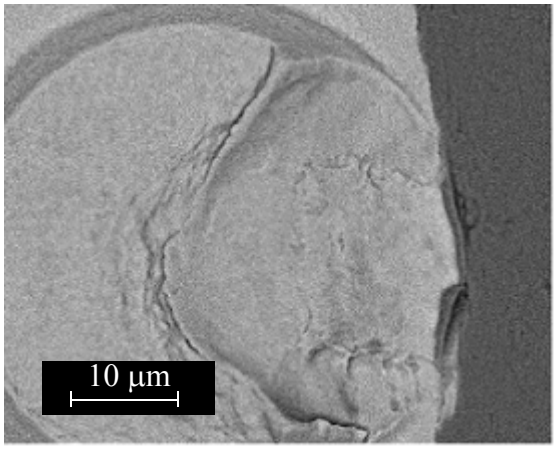

(a)

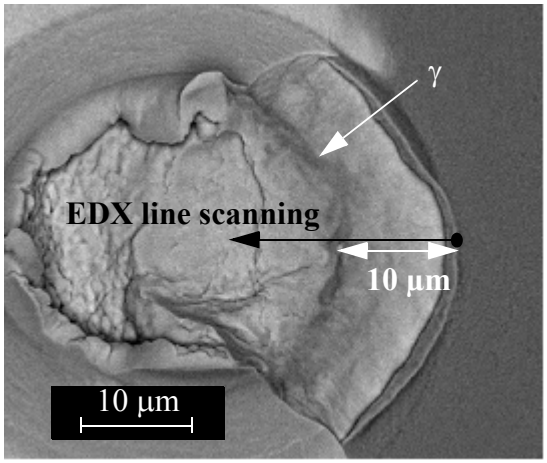

(b)

Fig. 4.24 BSE images of tail bond area at different BF. (a) 300 mN and (b) 1000 mN.

extend to the center of the TBBF (Fig. 4.19 (c)). This bond formation description agrees with those reported in Au wire crescent bonding [28, 27] and Al wedge bonding processes [85]. With further increase of US, tail bond extends to the inside of the capillary hole which is 8-10 µm away from the capillary chamfer as shown in Fig. 4.26. In addition, the WRA is increased toward the capillary hole as US increases. The tail bond formation with US is summarized in Fig. 4.27. Due to the force applied, ultrasonic friction does not occur with low US. As US increases, the ultrasonic friction starts at the edge of contact area as indicated by "β", resulting in a "partial bond" which fractures during wire tail break leaving a characteristic "fracture area". With increasing US, the WR is growing from the capillary chamfer to the hole. With further increase of US, WR and WBA cover all of TBBF.

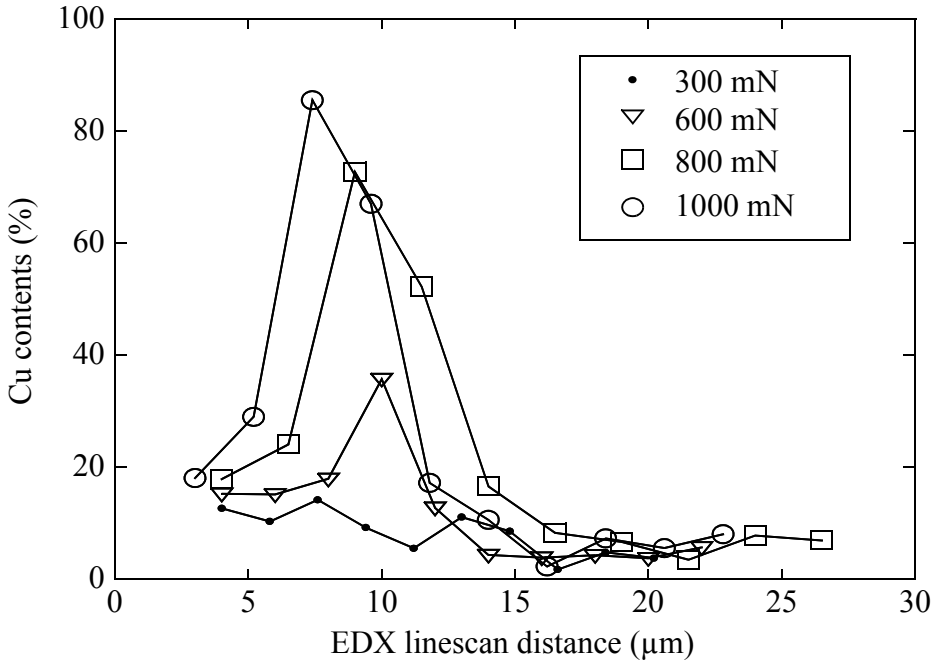

Fig. 4.25 Cu contents change obtained with EDX as BF increases. IF = 1000 mN, US = 72 %, BT = 25 ms, T = 220 °C.

4.2.4.2 Relationship between TBF and WBA

The tensile strength (σ_{UTS}) of wire in conventional wire tensile test is expressed using

$$\sigma_{UTS} = \frac{f}{A} \tag{4.2}$$

where σ_{UTS} is tensile strength of the wire, f is applied force to break the wire, and A is cross-sectional area of the wire.

For TBF measurement, the Eqn (4.2) can be modified using

$$TBF = \sigma_{WR} \times A_{WBA} \tag{4.3}$$

It can be known from the Eqn. (4.3) that the TBF is dependant on deformed wire strength (σ_{WRA}) and area (WBA) where the wire breaks.

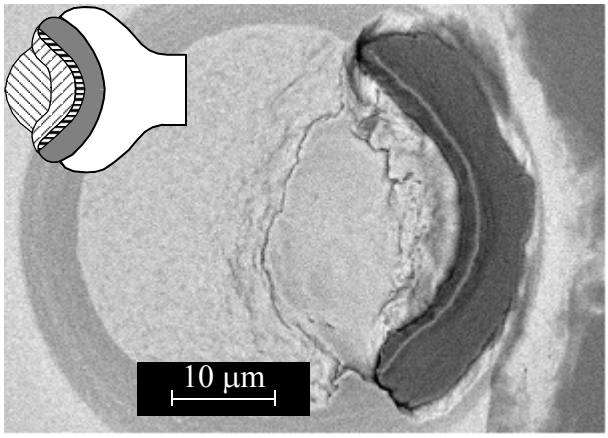

Fig. 4.26 BSE image of tail bond imprint with US of 80%.

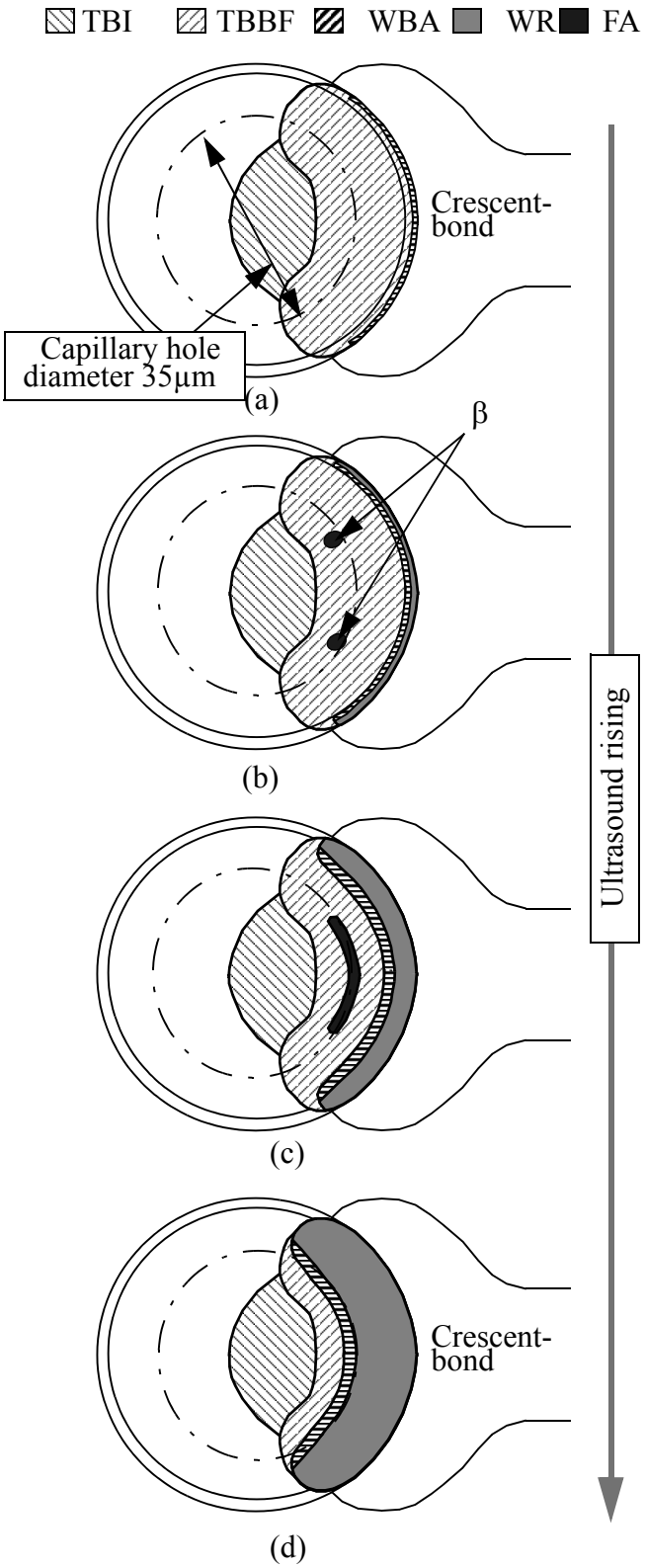

Fig. 4.27 Mechanism of tail bond formation as US increases.

The results obtained with US and BF as shown in Figs. 4.17 and 4.18 indicate that the TBF does not directly relate to WBA. It is because of the additional interfacial bond strength (IBS) as shown in Fig. 4.19 (additional fracture area). Hence, the TBF can be expressed using

$$TBF = \underbrace{\sigma_{WR} \times A_{WBA}}_{WRS} + \underbrace{\sigma_{IBBF} \times A_{IBBF}}_{IBS} \quad (4.4)$$

No indication of fracture on the TBI is observed with US lower than 52 % as shown in Figs. 4.19 (a) and which means that the IBS becomes zero. The TBF becomes proportional to σ_{WR} and A_{WBA}. The TBF is 53.7 mN and the A_{WBA} is 28.7 μm^2 with US of 52 % as shown in Fig. 4.17. The σ_{WRA} is calculated to be 1.9 mN/μm^2. As US increases, ultrasonic friction increases, resulting in IBS increase. Therefore, the correlation between TBF and WBA is smaller for US larger than 75 % (Fig. 4.17). Mayer and Schwizer [86] reported that ultrasonic friction increases first and then decreases as BF increases. As shown in Fig. 4.18, with BF lower than 500 mN the correlation between the TBF and WBA is not found because the IBS in the Eqn. (4.4) increases. Hence, in order to find the correlation IBS should be considered. On the other hand, as BF increases, ultrasonic friction decreases, resulting in less interfacial fracture occurring. The effect of the IBS is reduced, resulting in a larger correlation between the TBF and WBA.

The tensile breaking load (force) of 25μm Cu wire is measured with Instron 5540 Microtester (MA, USA). In order to have statistically reliable average, a total of 20 measurements were performed. The wire length and test speed used [87] are 254 mm and 25.4 mm/min, respectively. The tensile breaking force obtained is 127 $\pm$ 4 mN. The radius of the wire used here is 12.5 μm. With Eqn. 4.2, the σ_{UTS} is calculated to be 0.52 mN/μm^2. It is concluded that the σ_{WRA} is 3.6 times higher than σ_{UTS} when US, BF, and IF of 52 %, 500 mN, and 1250 mN, respectively, are applied

on the Cu wire for bonding. The increase of the σ_{WRA} compared to σ_{UTS} is accounted with the increase of the material strength by material plastic deformation [88].

4.3 Summary

The innovative use of a proximity sensor attached to a commercial wire bonder allowed for the first time to concurrently optimize the two process responses PF and TBF for an example wire bonding process. The tail bond imprints are investigated with SEM. The major findings from this study are summarized as follows:

- Increasing the ultrasonic bonding time results in higher TBF but lower PF values. Values for PF and TBF are highest for process temperatures higher than the stability range of Ag oxide.

- US/BF PWs for average and cpk values are not directly overlapping. The US optimized for maximum average PF needs to be increased to maximize cpk_{PF}. The opposite is observed for TBF. The US optimized for maximum average TBF needs to be reduced to maximize cpk_{TBF}.

- There is a partial overlap of PWs for the cpk values of PF and TBF. The PW for TBF is smaller than that for PF. The Cu wire bonding process robustness was improved for the example process by reducing the BF from 700 mN to 450 mN. The new setting simultaneously achieves PF and TBF cpk values of at least 2.

- Tail bond quality depends on the interfacial bond strength and the deformed wire breaking strength. With high US or low BF, interfacial bond strength is higher than that with low US or high BF. Wire breaking strength is dominant with low US or high BF.

- Wire material (Cu) is diffused into the Ag surface on the tail bond imprint 8 - 10 μm away from the capillary chamfer. The amount of Cu is highest for high US and BF values. The wire residue increases into the inside chamfer of the capillary. Surface fracture of the Ag diepad extends into the center of the tail bond with US increase.

- For strong tail bonds, the Ag diepad surface fractures leaving Ag residues on the wire tail.

Chapter 5 Influence of Substrate Material Pick-up on Free Air Ball

Chip damages, such as pad peeling, cratering, or dielectric layer delamination, are major concerns in thermosonic Cu ball bonding process [58, 60, 79]. As low - *k* materials which are mechanically weaker than SiO_2 are applied as dielectric layers in order to increases performance and decrease noise by cross talk in microelectronic device, minimizing chip damage becomes a challenge.

Despite a number of studies performed, there is still lack of understanding of the sporadic occurrence of chip damage in thermosonic wire bonding. Especially, no studies have been reported on the possibility of metallization material being picked up by the wire tail during breaking from the metallization and the effect of such pick - up on the Cu wire FAB formation. The substrate material pick - up on the wire tail are discussed in Chapter 5.2. The effects of bonding parameters on the substrate material pick up are demonstrated in Chapter 5.3. The influences of the substrate material pick up on FAB diameter, hardness, and oxidation are reported in Chapters 5.4, 5.5, and 5.6, respectively.

5.1 Bond - off Process Modifications

The tail breaking process has been described in Chapter 2.1 and is understood by investigating tail bond imprint micrographs in Chapter 4.2. In this chapter, a new finding with closely looking at the tail bond imprint is reported as illustrated in Fig. 5.1.

All FAB samples have diameters of 50 µm and are produced within 30 min using a nominal substrate temperature of 150 °C and a shielding gas mixture of 95 % N_2 and 5 % H_2. The samples are removed from the bonder, mounted with epoxy at ambient temperature, and cross-sectioned.

A Leco DM-400 Microhardness tester is used to make up to three indentations per cross-sectioned FAB. The holding time is 15 s. The Vickers Hardness (HV) is calculated with $HV = 1.854 \times F / D^2$, where $F =$ 50 mN is the applied indentation force and D is the area of indentation measured with an optical microscope with image-pro software (Media cybernetics, Bethesda, MD, USA). An example of a cross-sectioned FAB with indentation marks is shown in Fig. 5.2

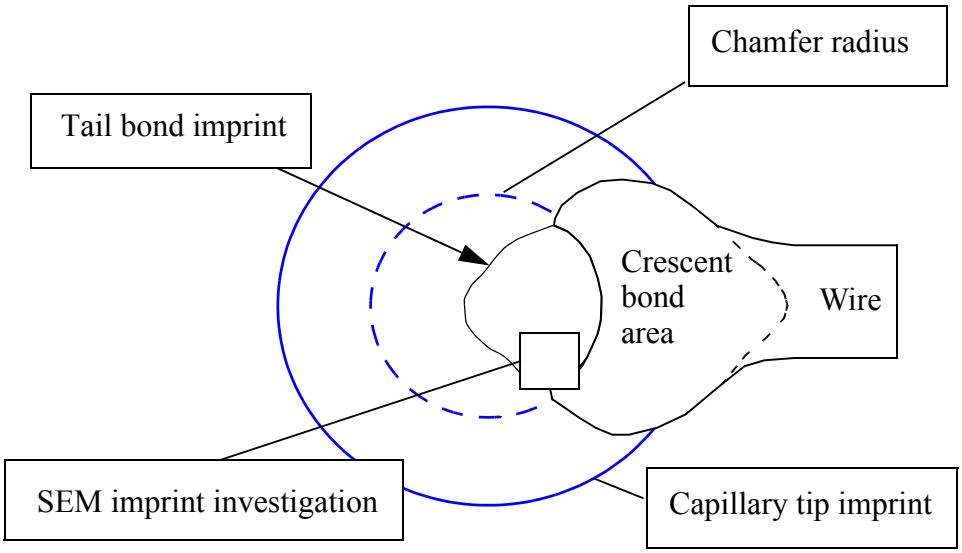

Fig. 5.1 Top view of tail and crescent bonds.

Three bond-off process modifications with and without EFO are made. These modifications serve the respective purposes of providing pick up evidence, understanding pick up process better, and comparing the FABs produced with and without pick up.

Process modification 1 (PM1) is a standard bond-off of the required wire end sample followed by a manual bending operation, as shown in Figs. 5.3.(a) - (e) and listed in the following.

(a) Creating a wire tail.

(b) the wire tail is manually bent using a stiff wire as a tool.

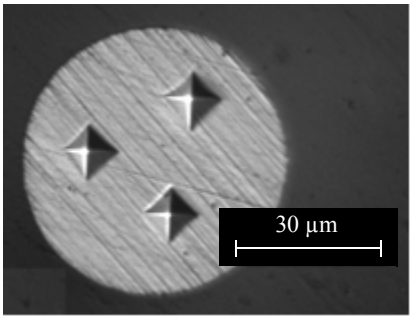

Fig. 5.2 Optical microscopy of indentation marks.

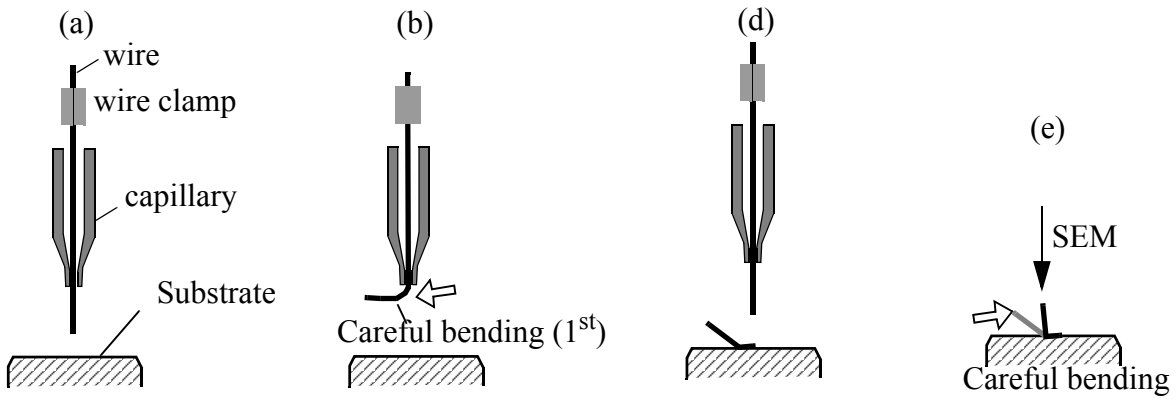

Fig. 5.3 Illustration of bond - off process without EFO fire in order to investigate the pick up by Cu wire tail. Arrows indicate careful bending.

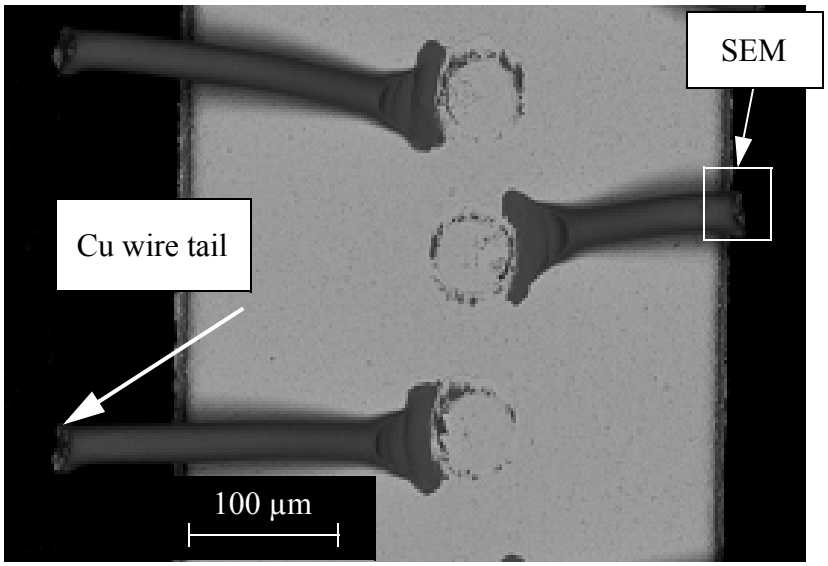

Fig. 5.4 Bond - off process without EFO fire exposing the tail end underside suitable for material pick up investigation.

(c) A standard bond-off process is performed. The standard bond-off process leaves the bent wire piece on the metallization

(d) One more bending operation is manually carried out, resulting in the remaining wire standing at 90º for SEM observation. Examples of resulting samples are shown in Fig 5.4.

Process modification 2 (PM2) allows to study the flattened zone of the wire where it was pressed to the substrate and is illustrated in Figs. 5.5 (a) - (h), corresponding to the following steps.

(a) Creating a wire tail.

(b) Wire tail is carefully bent as indicated by an arrow.

(c) A bond-off without US is performed, creating an initial flattened contact area on the wire piece.

(d) The lack of US results in the wire not sticking on the metallization and moving up with the capillary to the set position.

(e) The wire is bent again.

(f) a normal bond-off is performed with US, BF, and IF of 60 %, 450 mN, and 1000 mN, respectively.

(g) Due to the US used, the bent wire piece remains bonded on the metallization.

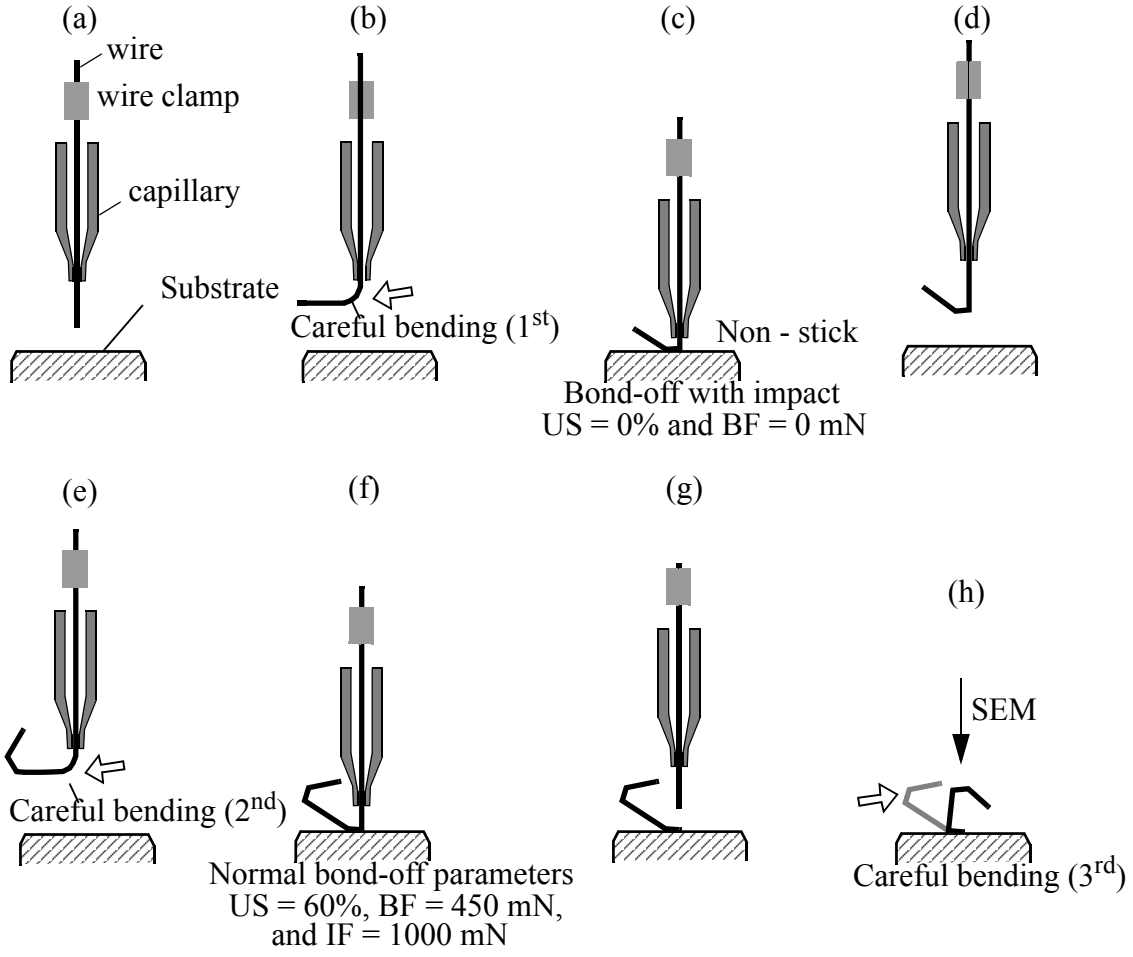

Fig. 5.5 Illustration of bond - off process modification for studying the pick up by impact. Arrows indicate careful bending.

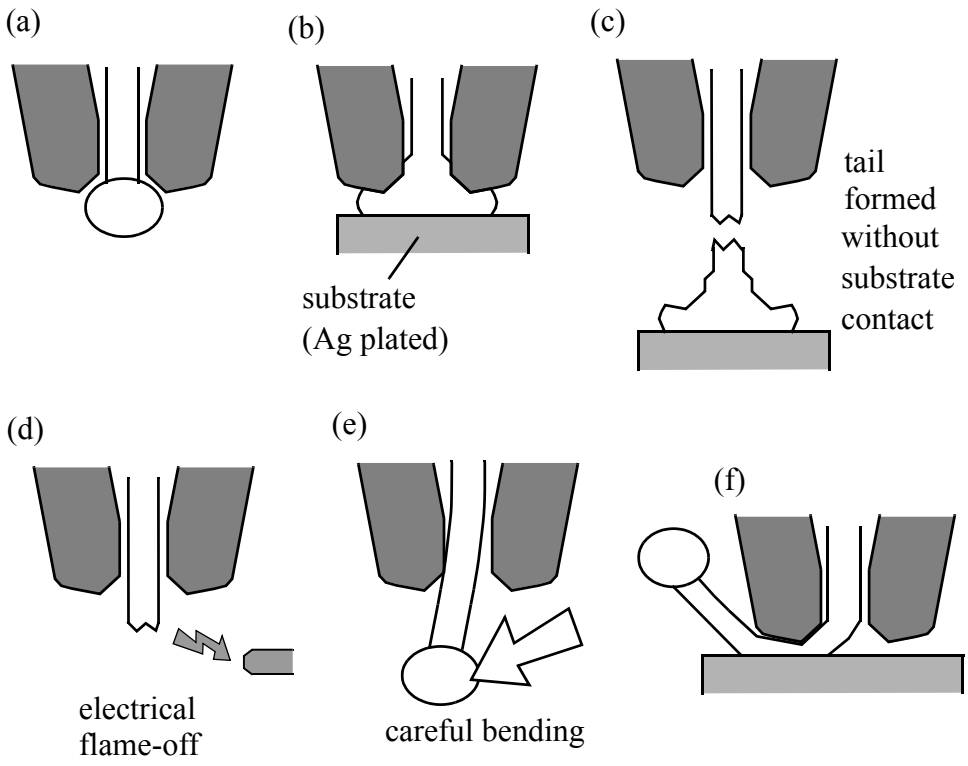

Fig. 5.6 Illustration of bond-off process modified to obtain FAB without Ag pick up. Arrow indicates careful bending.

(h) The wire piece is bent to expose the initial contact area of the wire piece for SEM observation.

Process modification 3 (PM3) aims to obtain FABs without substrate material pick-up for comparison. The bond-off process is modified as illustrated in Figs. 5.6 (a) to (f). The details of this procedure are explained in the following.

(a) A single EFO is carried out to produce a 50 μm diameter FAB.

(b) A normal bond - off operation is carried out without bending the wire. A ball is bonded.

(c) During the subsequent wire breaking operation, the wire breaks in the heat - affected - zone above the ball. A tail without any Ag pick - up is produced.

(d) An EFO is made to wire material which had no physical contact to the substrate metallization.

(e) The resulting wire with FAB will be bent over manually to allow for a normal bond - off.

(f) A normal bond - off is made. The FAB sample is fixed to the substrate and ready for inspection.

5.2 Pick up of Substrate Metallization

The SEM image of an imprint area as defined in Fig. 5.1 is shown in Fig. 5.7 showing ductile fractures indicated by arrows. The BSE image of a similar sample produced with the same process is shown in Fig. 5.8 (a) confirms that no Cu residue piece is left on the substrate and the fracture occurs inside the substrate material. The study of BSE images of wire tails confirms that substrate material is picked up by the Cu wire as shown in Fig. 5.9. The EDX results shown in Fig. 5.10 confirms that the white areas in Fig. 5.9 are Ag. Similar white areas picked up by Cu

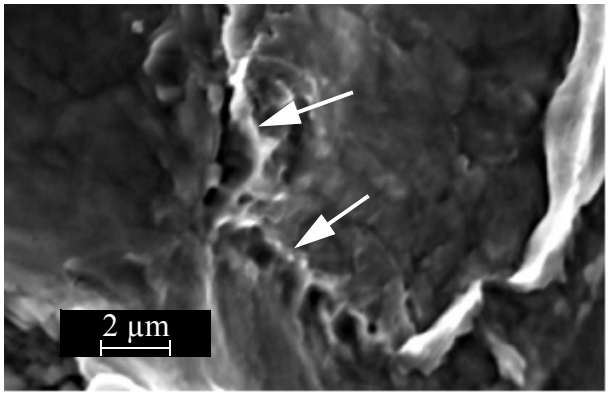

Fig. 5.7 SEM of Cu tail bond imprint on Ag plated substrate showing fractured area in Fig. 5.1.

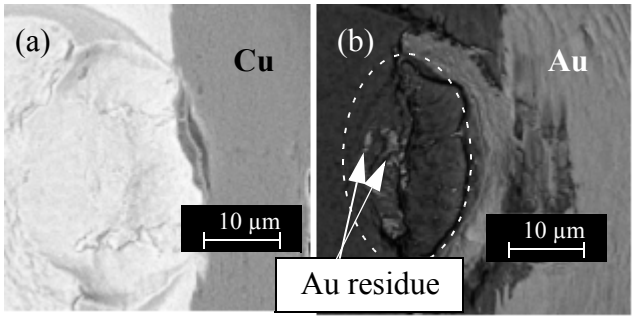

Fig. 5.8 Tail bond imprint made with (a) Cu and (b) Au wires.

wire tail when tail break occurs on BGA Au substrate are observed as shown in Fig. 5.11. The EDX results shown in Fig. 5.12 confirms that the white areas in Fig. 5.11 are Au.

However, with Au wire, the fracture occurs inside the wire material, resulting in Au residue left on the imprint as shown in Fig. 5.8 (b). In addition, Au wire tail picks up Ag from leadframe as shown in Fig. 5.13. Tail bond imprint observation of Au wire is made on Ag plated leadframes only as the determination of Au left on Au substrates is not straightforward.

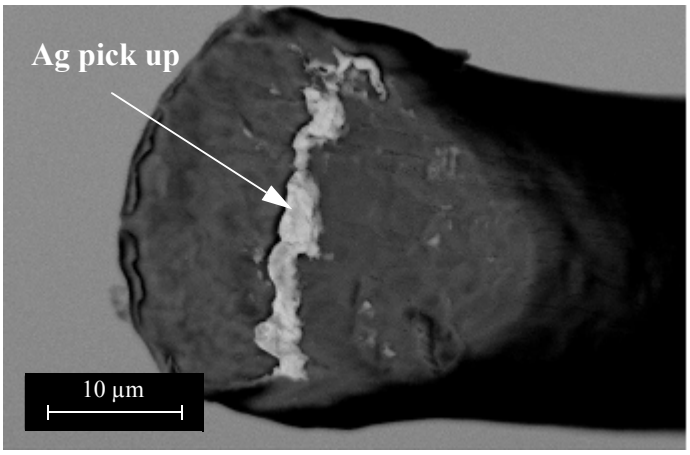

Fig. 5.9 Ag pick up found on Cu tail when Cu wire is bonded on Ag leadframe.

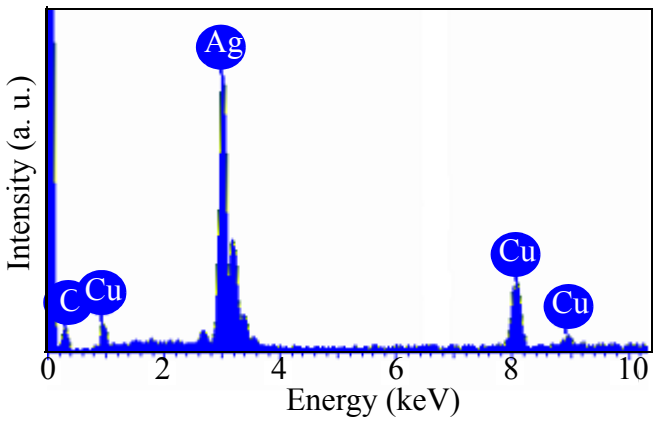

Fig. 5.10 EDX result of the white area in Fig. 5.9.

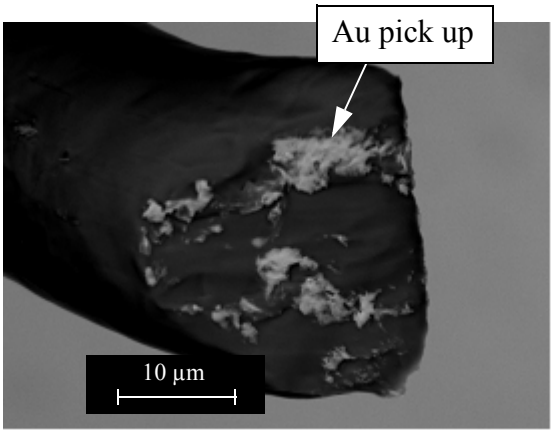

Fig. 5.11 Au pick up found on Cu tail when Cu wire is bonded on Au BGA substrate. IF, US, BF, BT, and T are 400 mN, 50%, 450 mN, 25 ms, and 150 °C, respectively.

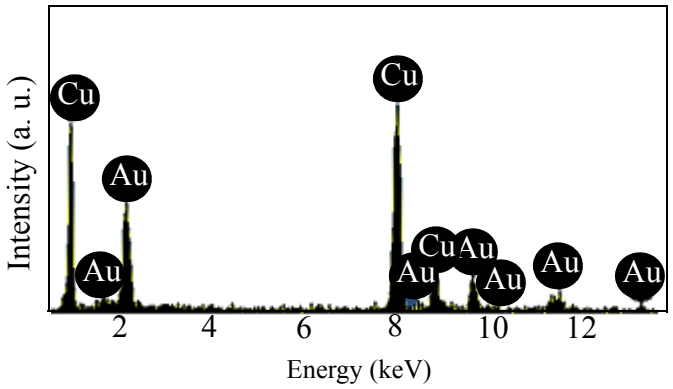

Fig. 5.12 EDX result of the white area in Fig. 5.11.

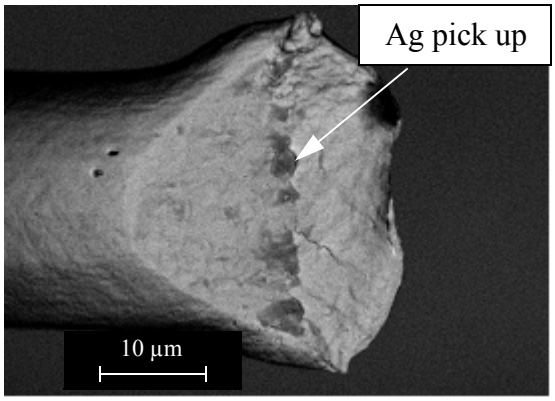

Fig. 5.13 Ag pick up found on Au tail. IF, US, BF, BT, and T are 400 mN, 50%, 450 mN, 25 ms, and 220 °C, respectively.

5.3 Influence of Bonding Parameters

Two types of processes are investigated to separate the effects of bonding parameters on the amount of pick up. They are impact process (IF without US and BF) which corresponds to a force only process, and friction process (IF with US and BF) which combines force with ultrasound. For simplicity, on Cu wire is used for this parameter study.

5.3.1 Force without Ultrasound

In order to understand the effect of individual process parameters on the pick up of material, first only IF is used to study the Cu wire deformation and pick up on BGA Au substrate using PM2. The IF is varied from 200 mN to 1200 mN in 200 mN steps while US, BF, BT, and T are fixed to 0 %, 0 mN, 5 ms, and 150 °C**,** respectively.

The contact area is investigated with BSE as shown in Figs 5.14 (a) - (d), showing samples after application of IFs of 200, 600, 800, and 1200 mN, respectively. Pick up in the form of bright Au particles is found on the Cu wire with each tested IF value.

The Cu wire with IF of 200 mN is very small [Fig. 5.14 (a)]. As IF is increased to 600mN, circular substructures on bottom of the Cu wire are observed [Fig. 5.14 (b)]. With IF of 800mN, the imprints shape is elongated toward crescent bond [Fig. 5.14 (c)]. The imprints substructure on the wire have an elongated shape with IF of 1200 mN [Fig. 5.14 (d)] towards both wire direction while circular substructures remain in the centre. This observation is discussed using the illustration in Figs. 5.15 (a) and (b) With low IF, Cu wire deformation occurs mainly along the IF direc-

tion (normal force) as shown in Fig. 5.15 (a). As IF increases, Cu wire is further deformed and pushed to the wire directions, creating a lateral material flow component amplified by the angle present at the capillary tip as shown in Fig. 5.15 (b). This material flow causes the enlongated shapes of the imprint structures.

In contrast to Au metallization, material pick up is not observed on the Cu tail with PM2 IF Ag metallization is used as shown in Fig. 5.16.

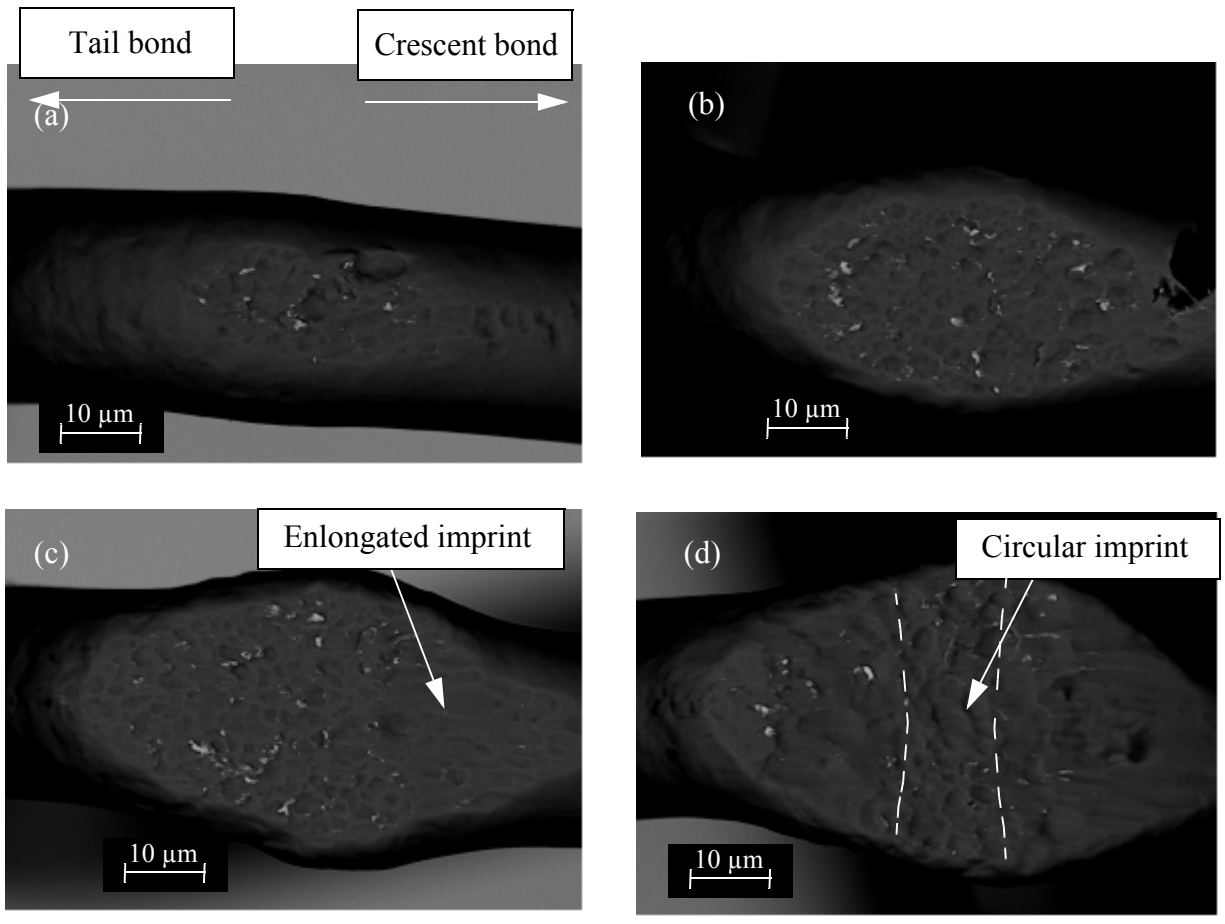

Fig. 5.14 SEM images of Cu wires with IF of (a) 200 mN, (b) 600 mN, (c) 800 mN, and (d) 1200 mN. US, BF, BT, and T are 0 %, 0 mN, 5 ms, and 150 °C, respectively.

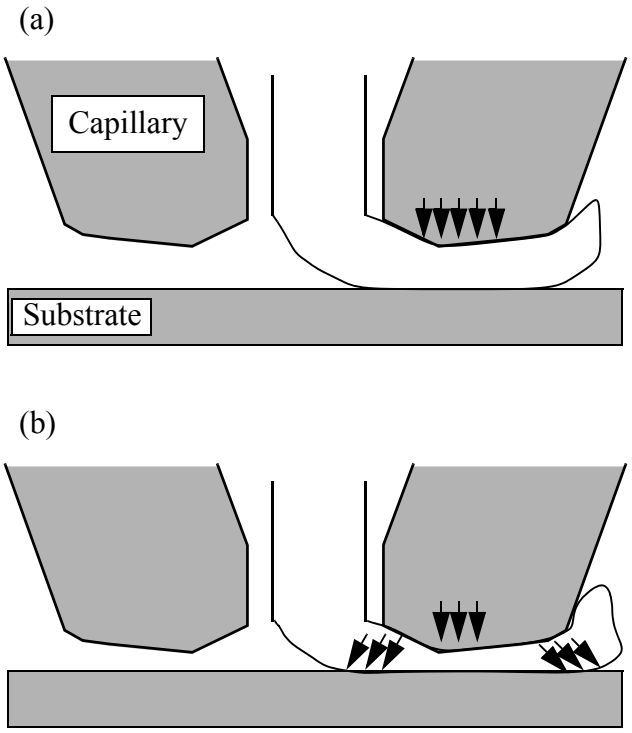

Fig. 5.15 Illustrations of normal and shear force applied during impact. (a) low IF and (b) high IF.

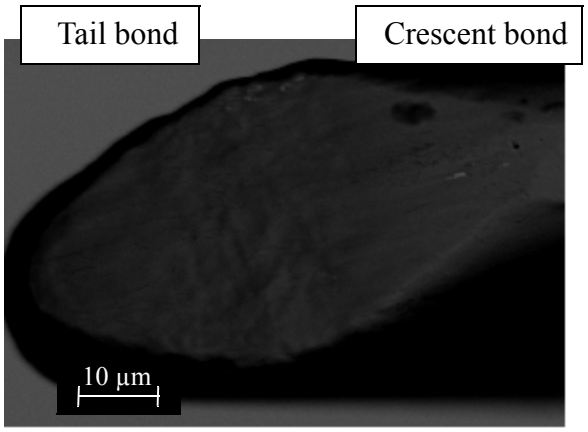

Fig. 5.16 SEM of imprint of Cu wire made on Ag leadframes with IF of 800 mN. US, BF, BT, and T are 0 %, 0 mN, 5 ms and 220°C, respectively.

5.3.2 Ultrasound with Force

To obtain a stable tail breaking force (TBF), the BF parameter is recommended to be under tight control as shown in Fig. 4.11, eg. by fixing it to BF = 450 mN while US and IF are varied for the following study.

The area covered by Au pick ups is quantified with an analysis software. Figure 5.17 shows the measured area of Au pick up, revealing the strong effect of IF. As IF is increased, the area of Au pick up decreases. Figures 5.18 (a) and (b) are example SEM images showing pick ups obtained with IFs of 400 mN and 1000 mN, respectively. With IF = 400 mN, the area of Au pick up increases as US is increased from 50 % to 60 %. With IF higher than 700 mN, no influence of US on Au pick is observed.

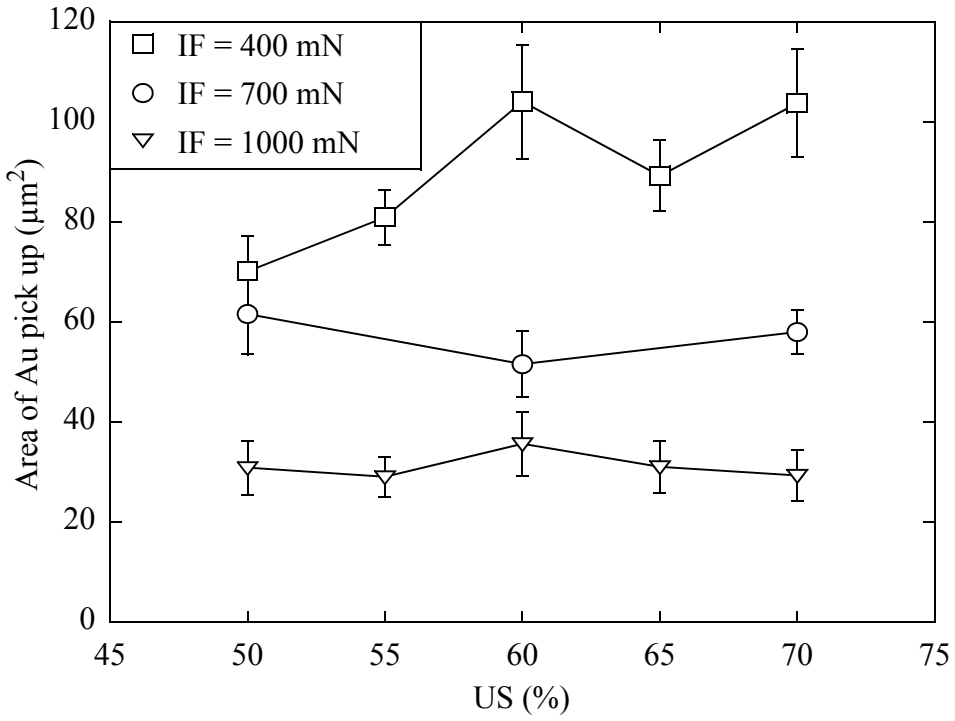

Fig. 5.17 Area of Au pick up depending on US and IF.

The relatively high amount of Au pick up observed with IF = 400 mN may be due to the type of deformation the wire experiences. For such relatively low IF values, the impact type deformation is less dominate than the ultrasound enhanced deformation (UED) of the wire as it forms the contact zone. Figure 5.19, shows experimental results of the wire deformation obtained with various US values between 0 % and 70 %, and with low and high IF values. The Cu wire is highly deformed with IF = 1000 mN and further UED is limited to about 7 % with US of 70 %. In contrast, the Cu wire deformation with US and IF of 0 % and 400 mN, respectively, is 19.43 µm.

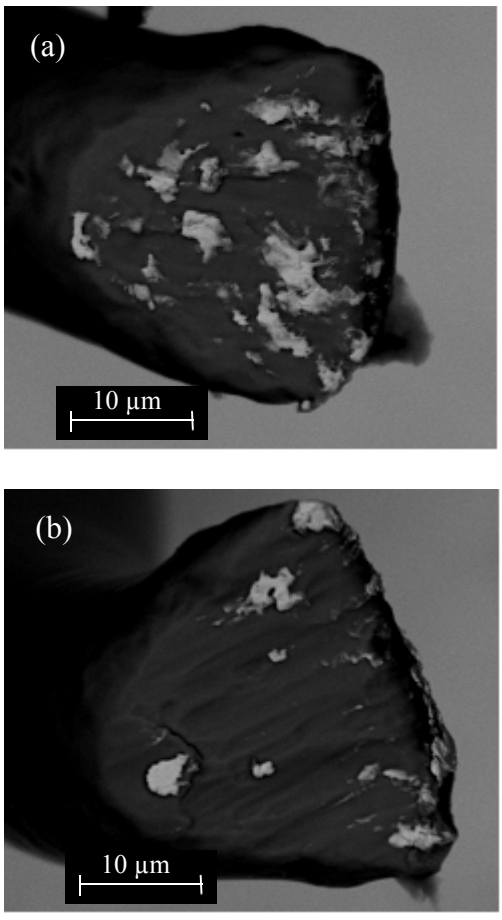

Fig. 5.18 Au pick ups with IFs of (a) 400 mN and (b) 1000 mN. US, BF, BT, and T are 60 %, 450 mN, 25 mN, and 220°C, respectively.

While applying US of 70 %, the Cu wire deformation is increased by about 48 % compared to the value without US.

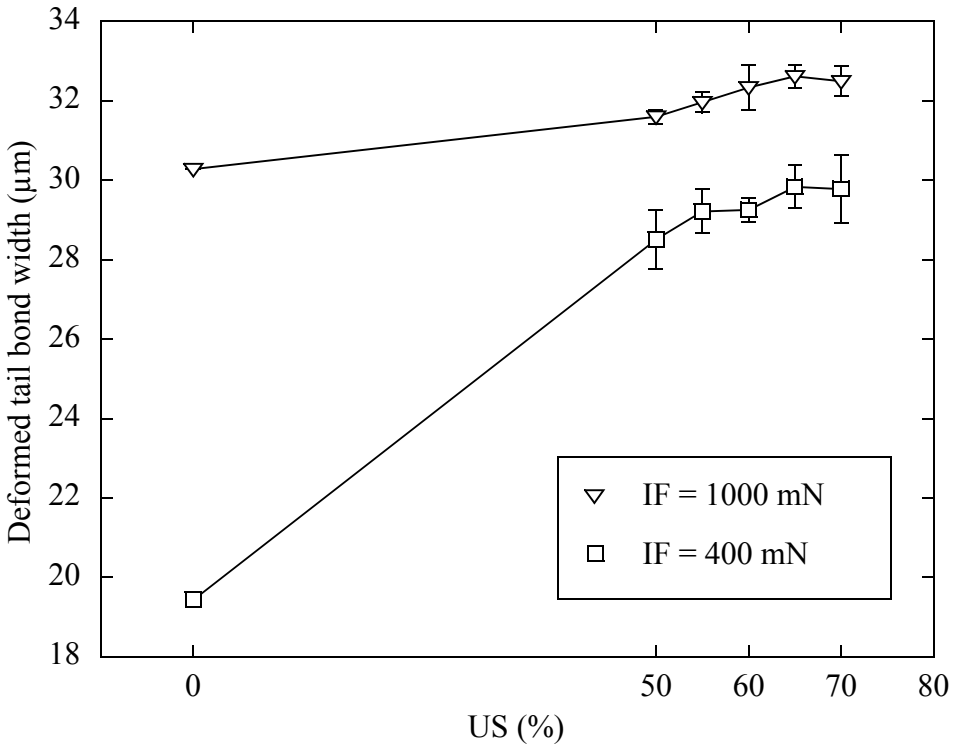

Fig. 5.19 Increase of tail bond width contact region with US and IF.

5.4 Free Air Ball (FAB) Diameter

The effects of the Ag pick up on the FAB diameters are investigated. The currents used to produce FAB samples are 55, 60, 65, 70, and 83 mA while pre-spark voltage and EFO time are 4500 mV and 1 ms, respectively. The diameter measurement are carried out with an optical microscope. An average diameter D is determined using SEM images as e.g. shown in Fig. 5.20, providing d_1 and d_2, i.e. two experimental diameters used to calculate $D = (d_1 + d_2) / 2$ which is used for the subsequent comparisons.

A total of 20 FABs produced with each current are measured. The results displayed in Fig. 5.21 show that the Ag pick up tends to reduce the FAB diameter, but the analysis of the data variation yields that this reduction is not significant. The FAB diameters obtained with and without Ag pick - up are the same with a confidence level above 95 %.

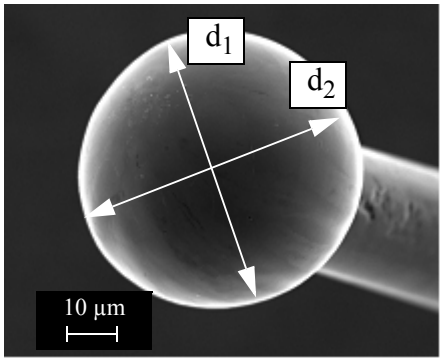

Fig. 5.20 SEM of FAB for diameter measurement.

5.5 FAB Hardness Comparison

The two IF values, 400 mN and 1000 mN are selected to produce Cu FABs with higher and lower amount of Au pick up, respectively. FABs without pick up are used for reference. The FAB hardness results are shown in Fig. 5.22. The average hardness decreases as the amount of Au pick up is increased. The FAB hardness average and standard deviation values measured for high, low, and zero amounts of pick up are 76.8 $\pm$ 3.4 HV, 75.5 $\pm$ 7.14 HV, and 74 $\pm$ 6.0 HV, respectively, showing a monotonous decrease as pick up increases. The *t* - value summarized in Table 5. 1 indicates that the hardness of FAB is significantly (95 % confidence level) reduced with Au pick up with IF of 400 mN.

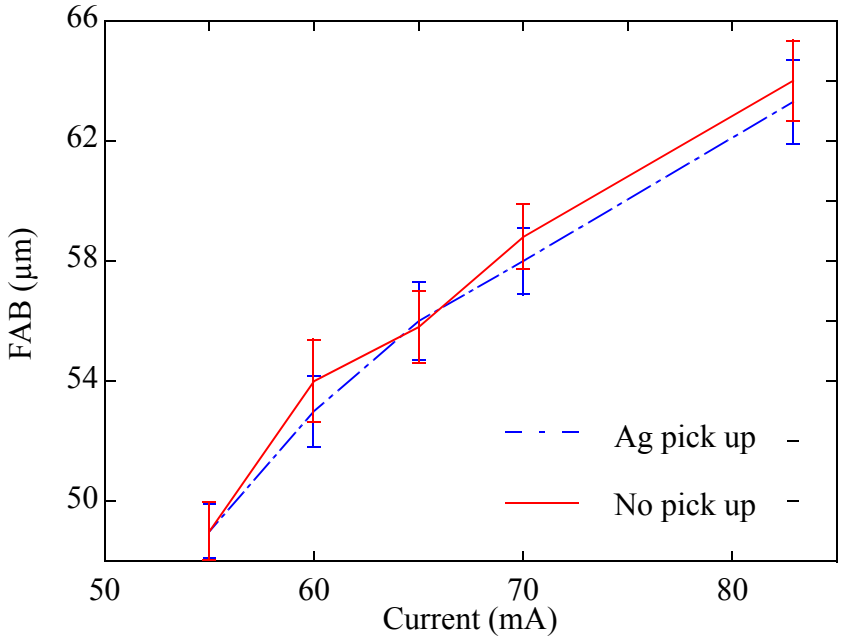

Fig. 5.21 Comparison of FAB diameter with and without Ag pick up. The errorbars indicate the standard deviations.

The same hardness measurement is performed with and without Ag pick up. For simplicity, IF of 400 mN is selected. The results is shown in Fig. 5.23 (b). The FAB hardness average and standard deviation values measured for with and without pick up are 77.8 ± 2.74 HV, 79.5 ± 3.46 HV, respectively, showing a decrease with pick up. From the statistical calculation of t - value = 2.1, it is known that the difference of FAB hardness is significant (95 % confident level). The standard deviations with Au pick up are significantly larger than that without pick up.

It can be known from the comparison of Figs. 5.22 and 5.23 that Au pick up increases the standard deviation of the hardness while Ag pick up does not. The dopants added in Cu wire in manu-

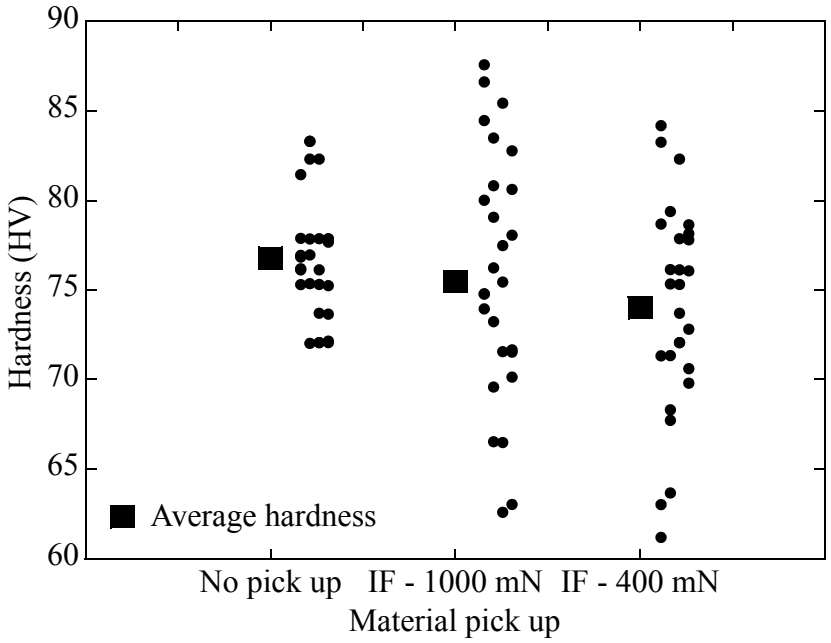

Fig. 5.22 Hardness comparison of FAB with and without Au pick up. The sample size is 30.

Table 5. 1: Summary of t - values obtained with IFs of 400 and 1000 mN.

IF (mN)	*t* - value	Significant Difference
400	2.20	Yes
1000	0.91	No

facturing process are summarized in Table. 5. 2,. The Ag is added in Cu wire during wire manufacturing process which means that Ag picked up by Cu wire tail increases the contents of Ag in the FABs. In contrast, Au picked up by Cu wire tail is a foreign element which is not added during wire manufacturing process.

With the large distribution in FAB hardness as shown in Fig. 5.22, it is difficult to select a hardness for optimization. If the average hardness is assumed to be selected, the FABs with low hardness values result in overbonding while those with high hardness does not reach to the optimum ball bond strength. The ball non -stick on the bonding pad may occur if the FABs have extremely

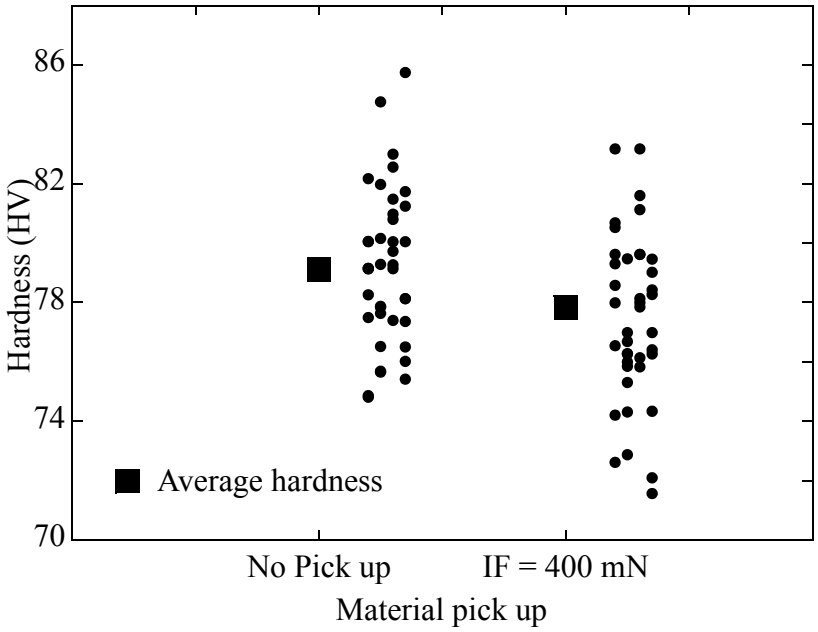

Fig. 5.23 Hardness comparison of FAB with and without Ag pick up. The sample size is 40.

Table 5. 2: Dopants and their contents in Cu wire [80]

Dopants	Ag	Ca	Fe	Al
Contents (ppm)	< 10	< 10	< 1.0	< 10

high hardness. When FAB hardness is increased, higher bonding parameters are required to obtain optimum bonding.

5.5.1 Discussion

It is known that higher hardness of Cu balls than that of Au balls may cause chip damage [3, 58, 81]. Onuki et al [81] reported that with the decrease of ball hardness, chip damage decreases and disappears when the hardness of the ball decreases to a certain value. Hence, hardness values can be used for upper specification limit (USL) for chip cratering.

Using the hardness data obtained with and without Au pick up as shown in Fig. 5.22, the values of process capability index (cpk) is calculated for each set of FAB hardness measurements using

$$cpk = \frac{USL - \overline{H_{HV}}}{3\sigma} \tag{5.1}$$

where $\overline{H}_{HV}$ is an average hardness.

To visualize the effect of the standard deviation on process capability, the cpk values as USL is changed are shown in Fig. 5.24. USL higher than 119 HV and 110 HV for material pick up by Cu wire tail, with IFs of 1000 mN and 400 mN is required in order to have $cpk_{HV} > 2$. It is concluded that in many cases and in spite of reducing the average FAB hardness, substrate material pick up by Cu wire tail increases the probability of the chip cratering during Cu ball bonding process.

The estimated volumetric fractions of Au in 50 µm diameter Cu FABs obtained with IF of 400 mN and 1000 mN are 0.08 % and 0.03 %, respectively. The wire used is 99.99 % pure Cu

containing less than 0.01 % (100 ppm) impurities. The estimated Au contents from pick up exceeds the specified impurity content. The relative Au contents increases as FAB diameter is decreased as shown in Fig. 5.25. For an FAB that is 35 μm in diameter, Au contents can be 0.23%. according to the estimation. The pick up thickness is roughly estimated using the SEM image shown in Fig. 5.26, indicating thickness ranging between 0.1 μm and 1 μm. For simplicity, the pick up thickness is estimated to be 0.5 μm in subsequent volume estimations.

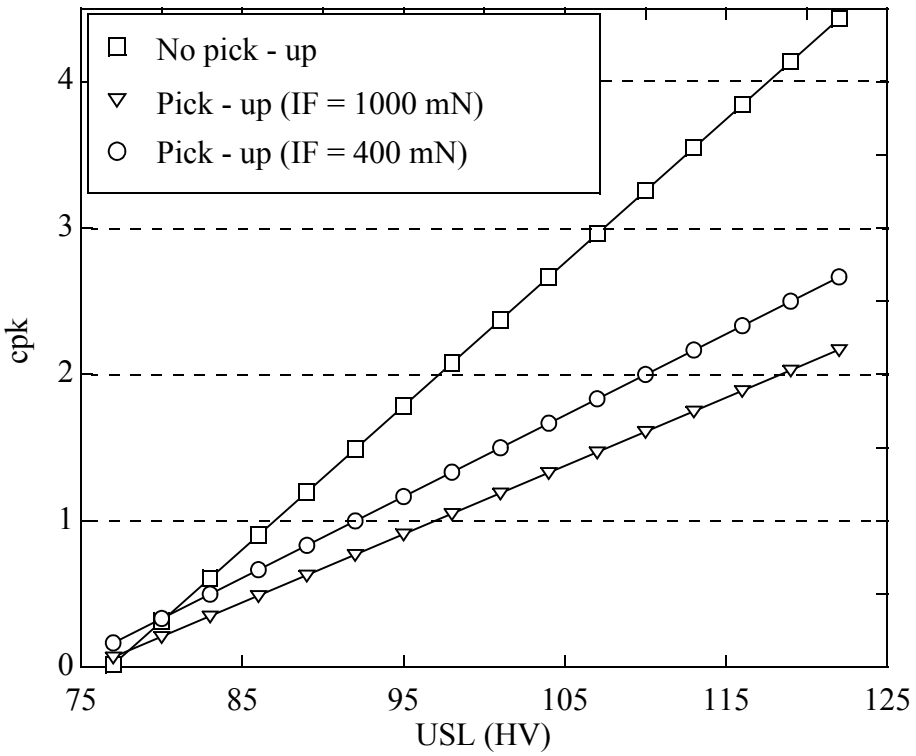

Fig. 5.24 Calculated cpk values as USLis increased.

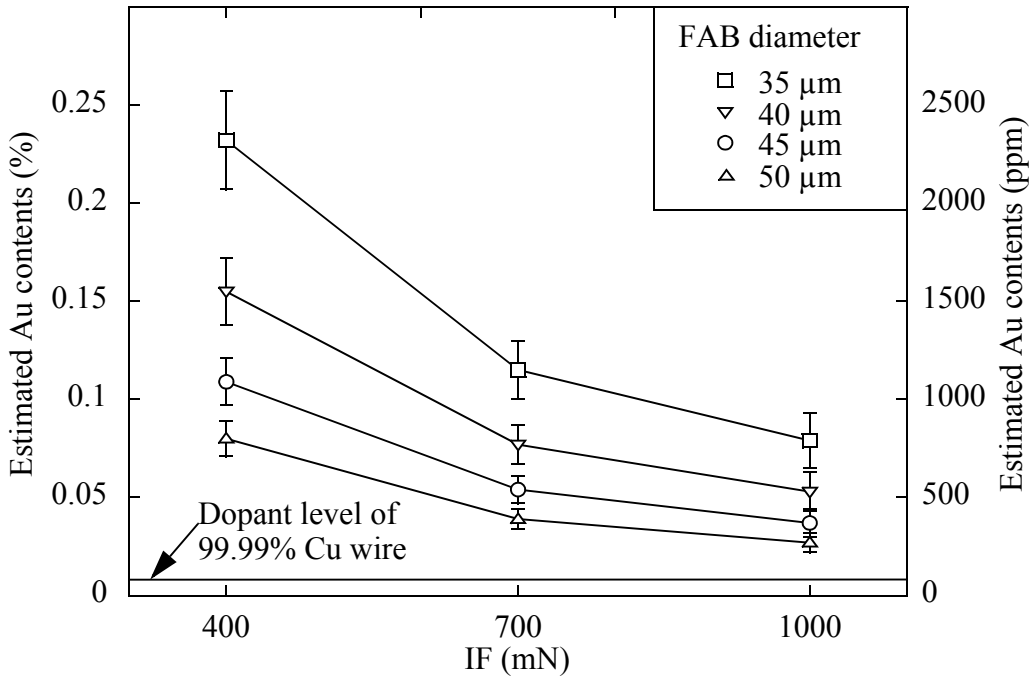

Fig. 5.25 Au pick up content changes in FAB with IF when FAB diameters are varied.

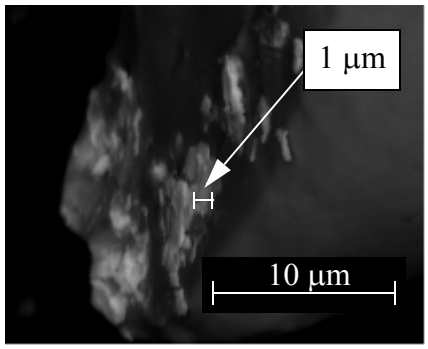

Fig. 5.26 Thickness of Au pick up.

5.6 Oxidation of Free Air Ball (FAB)

Studies [89, 90] have been carried out in order to protect the hot Cu FAB from oxidation. The use of a shielding gas of 95 %N_2 and 5 %H_2 (forming gas) with optimized gas flow rate can prevent FAB oxidation.

The electrode-to-wire distance (EWD) is changed from 50 µm to 500 µm in steps of 50 µm to study the oxidation behavior of the Cu FAB. Figure 5.27 illustrates capillary, wire tail, and electrode to define the EWD during the EFO process. A shielding gas mixed with 5 %H_2 and 95 %N_2 with a flow rate of 0.5 l/min is used.

FABs with circular shapes like that shown in Fig. 5.28 are formed using all EWD values. However, for EWD values of 300 µm and higher, lines are formed on the FAB surface both with and without Ag pick up. An example for this is shown in Fig. 5.29. EDX results summarized in

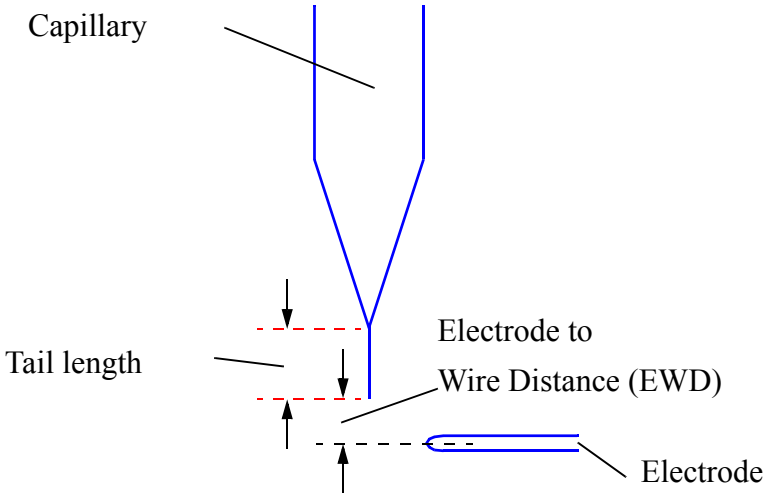

Fig. 5.27 Definition of tail length and EWD.

Table 5. 3 show that significantly higher amounts of O and Ag are observed on the lines than the line-free area. A total of 10 measurements from 5 different FABs are conducted for reliable statistical values. As they occur when using the larger EWD distances, the actual position of FAB ball

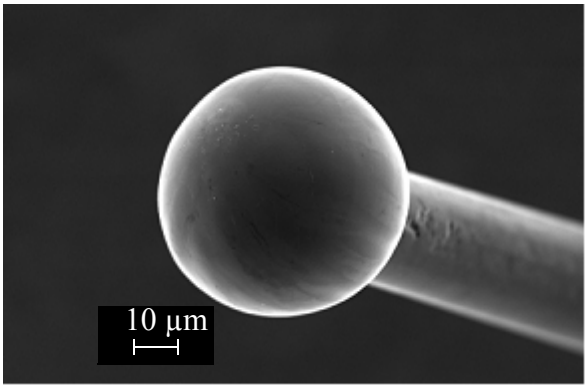

Fig. 5.28 SEM of FAB formed with EWD = 100 µm.

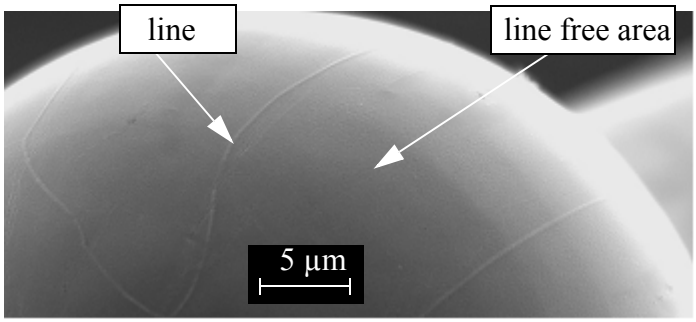

Fig. 5.29 Oxide line formation on the FAB surface at EWD of 300 µm.

Table 5. 3: Material contents measured at locations on FAB surface (Fig. 5.29). The sample size is 10.

	Line	Line free area
O (wt%)	3.05 ± 1.05	0.27 ± 0.26
Cu (wt%)	95.6 ± 0.96	99.35 ± 0.60
Ag (wt%)	1.09 ± 0.47	0.38 ± 0.24

during EFO process might be as shown in Fig. 5.30 (b). Even though in the beginning the wire tail is in the shielding gas effective region (SGER) as shown in Fig. 5.30 (a), the melting and resolidification of the material to produce the FAB changes the wire end position. The EFO consumes enough wire length so that the FAB is at least partly above the SGER where more oxygen is in the gas (Fig. 5.30 (b)), resulting in Cu FAB oxidation.

After etching of FABs in a solution mixed with 30 ml HCl + 10 g $FeCl_3$ + 120 ml Ethanol for 30 s, grain boundary lines are found, as shown in Fig. 5.31, which are similar (possibly identi-

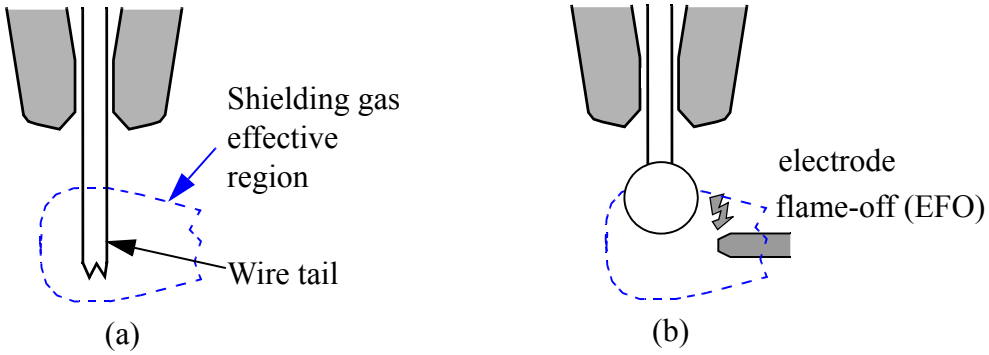

Fig. 5.30 Illustrations of sub-optimum shielding gas positioning with respect to (a) tail before EFO and (b) FAB after EFO. Upper part of FAB outside effective shielding region.

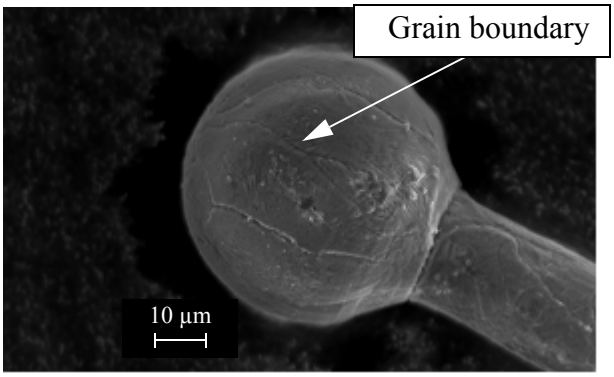

Fig. 5.31 SEM of Cu FAB after etching showing lines indicating grain boundaries.

cal) to the oxide lines in Fig. 5.29. Oxide growing faster along grain boundaries than normal to grain boundaries was reported with other materials [91, 92].

5.7 Summary

During investigation of the tail bond imprint as discussed in Chapter 4, the substrate surface fractures in the tail bond area are found. The fractured substrate materials can be attached on the wire tail end after tail breaking. The evolution of the wire tail end are studied in detail with SEM and Micro - hardness tester. The major findings from this study are summarized as follows:

- Cu wire tail picks up Ag and Au from the leadframe and BGA substrate, respectively, during tail breaking process. In case of Au wire, both Ag pick up and Au wire fracture occur. The amount of substrate material pick up with Au wire is much smaller than that with Cu wire due to the Au wire being fractured by itself, leaving the Au reside on the tail bond area.

- The substrate material pick up can be reduced, but can not be completely removed by controlling the bonding parameters. The lower the impact force, the higher the amount of Ag and Au pick ups on the Cu tail. Ultrasonic enhanced deformation is accompanied by a larger amount of pick up than if a process is dominated by impact deformation.

- The amount of Au pick up estimated in the Cu FAB exceeds the typical impurity and dopant levels in the wire. For Cu wire, the specific effects of the Au pick up must be taken into consideration for thermosonic ball bonding process.

- Compared with FABs obtained without pick up, FABs with Au pick up have a lower average FAB hardness. However, its standard deviation is higher. Therefore, Au pick up in Cu FAB can lead to more FABs that are exceptionally hard.

Chapter 6 Conclusions

Methods of improving the crescent bond quality and the tail bond stability with Cu and insulated Au wires have been demonstrated. Descriptions of the tail bonding process mechanisms based on tail breaking force measurement and tail bond imprint studies have been explored.

When bonding insulated wire, the insulation layer cracks where the underlying wire is heavily deformed. Such cracks occur at the contact zone periphery during initial deformation with a relatively high impact force. In a modified bonding process with a cleaning stage, a combination of low impact force, ultrasound, and 20 μm shift results in efficient local insulation layer removal. The removed layer remains on the substrate surface outside the new bonding zone. The cleaning stage before the basic bonding process improves the insulated Au wire pull force by about 26 %, bringing it well inside the range obtained with bare wire and the basic process.

The in-situ online tail breaking force measurement shows that the tail breaking force strongly depends on the bonding parameter combination. Using plasma cleaning prior to bonding, the tail breaking stability of the Cu wire process increases significantly. Maximizing PF using the conventional pull test will not automatically maximize TBF. Process parameter changes that improve the PF performance can deteriorate the TBF performance. In a case where a process was optimized using the conventional pull test, an efficient guideline to improve the TBF performance while maintaining an acceptable PF performance is the reduction of the bonding force parameter.

Tail bond quality depends on the interfacial bond strength and the deformed wire breaking strength. With high US or low BF, interfacial bond strength is higher than that with low US or high BF. Wire breaking strength is dominant with low US or high BF. Wire material (Cu) is diffused into the Ag surface on the tail bond imprint with the peak concentration 8 - 10 μm away

from the capillary chamfer. The amount of diffused Cu is highest for high US and BF values. The amount of Cu wire residue increases into the chamfer of the capillary as US increases. Surface fracture of the Ag diepad extends into the center of the tail bond as US increases.

The Cu wire tail picks up Ag and Au from the leadframe and the BGA substrate, respectively, during the tail breaking process while the Au wire tail fractures by itself, leaving the Au residue on the tail bond imprint. The lower the impact force, the higher the amount of Ag and Au pick up on the Cu tail due to ultrasound enhanced deformation in contrast to impact deformation. The amount of Au pick up estimated in the Cu FAB exceeds the typical impurity and dopant levels in the wire. Compared with FABs obtained without pick up, FABs with Au pick up have lower average FAB hardness. However, the standard deviation is higher. Therefore, Au pick up in Cu FAB can lead to more FABs that are exceptionally hard. This may be a possible reason for sporadic underpad damage.

References

[1] A. W. Wieder, “Status, trends and challenges in microelectronics for the next 10 to 15 years,” *Electrical Eng*., Vol. 79, pp. 79 - 84, 1996.

[2] E. J. Vardaman (2007, July), “Advanced packaging interconnect trends and technology development” K&S interconnect technology symposium. [Online]. Available: http:// www.kns.com/_temp/downloads/agendaJuly2007/1.pdf.

[3] G. G Harman, “Wire bonding in microelectronics: materials, processes, reliability, and yield," 2nd ed., McGraw-Hill, 1997.

[4] J. N. Aoh, C. L. Chuang, “Development of a thermosonic wire bonding process for gold wire bonding to copper pads using argon shielding,” *J. Electron. Mater.*, Vol. 33, pp. 300 - 310, 2004.

[5] J. Beleran, A. Turiano, D. Calpito, D. Stephan, Saraswawti, F. Wulff, C. Breach, “Tail pull strength of Cu wire on gold and silver - plated bonding leads,” in *Proc. SEMICON Singapore*, 2005, pp. 1 - 8.

[6] S. Okikawa, M. Tanimoto, H. Watanabe, H. Mikino, and T. Kaneda,”Development of a coated wire bonding technology,” *IEEE Trans. Comp. Hybrids, Manuf. Technol.,* Vol. 12, pp. 603 - 608, 1989.

[7] R. Lyn, W. Crockett,”Assembly using X-wire^{TM} insulated bonding wire technology,” in *Proc. SEMICON Singapore*, 2007, pp. 1 - 7

[8] J. Lee, M. Mayer, Y. Zhou, and S. J. Hong, “Iterative optimization of tail breaking force of 1mil wire thermosonic ball bonding processes and the influence of plasma cleaning,” *Microelectron. J.* Vol. 38, pp. 842 - 847, 2007.

[9] J. Lee, M. Mayer, Y. Zhou, and J. Persic, "Microelectronic wire bonding with insulated Au wire: Effects of process parameters on insulation removal and crescent bonding," Accepted in *Mater. Trans*.

[10] J. Lee, M. Mayer, Y. Zhou, S. J. Hong, and J. T. Moon, "Concurrent optimization of crescent bond pull force and tail breaking force in thermosonic Cu wire bonding process," Accepted in *IEEE Trans. Electron. Packag. Manuf.*

[11] J. Lee, M. Mayer, Y. Zhou, S. J. Hong, and J. T. Moon, "Silver pick up during tail formation and its effect on Cu free air ball diameter and hardness," Submitted to *IEEE Trans. Comp. Packag. Technol*.

[12] J. Lee, M. Mayer, Y. Zhou, S. J. Hong, J. T. Moon, and J. Persic, "Influence of gold pick up on the hardness of copper free air ball," Submitted to *Microelectron. Reliab*.

[13] G. Harman and J. Albers, "The ultrasonic welding mechanism as applied to aluminum- and gold-wire bonding in microelectronics," *IEEE, Trans. Parts, Hybrids, Packag.,* Vol. PHP-13, pp. 406 - 412, 1977.

[14] S. Murali, N. Srikanth, C. Vath 3, "Grains, deformation substructures, and slip bands observed in thermosonic copper ball bonding," *Mater. Charact.,* Vol. 50, pp. 39 - 50, 2003.

[15] Z. W. Zhong, T. Y. Tee, J. E. Luan, "Recent advances in wire bonding, flip chip and lead-free solder for advanced microelectronics packaging," *Microelectron. Int.*, Vol. 24, pp. 18 - 26, 2007.

[16] P. Ratchev, S. Stoukatch, B. Swinnen, "Mechanical reliability of Au and Cu wire bonds to Al, Ni/Au, and Ni/Pd/Au capped Cu bond pads," *Microeletron. Reliab.,* Vol. 46, pp. 1315 - 1325, 2006.

[17] ITRS (2006):The International Technology Roadmap for Semiconductors - Assembly and Packaging Update, pp. 9 - 10. Available: http://www.itrs.net.

[18] K. S. Goh, Z. W. Zhong, “Two capillary solutions for ultra fine - pitch wire bonding and insulated wire bonding,” *Microelectron. Eng,.* Vol. 84, pp. 362 - 367, 2007.

[19] N. L. Deblieck, P. J. Feller,”The evaluation of thermosonic wedge bond width and optimal pull strength,” in *Proc. International Symposium on Microelectronics*, 1996, pp. 444 - 449.

[20] MIL-STD-883E: Bond strength (desructive bond pull test), METHOD 2011.7, 1989, pp. 1 - 6.

[21] G. Harman, “Reliability and yield problems of wire bonding in microelectronics - the application of materials and interface science” International society for hybrid microelectronics, McGraw - Hill, 1989.

[22] D. Montgomery, Introduction to Statistical Quality Control, John Wiley and Sons, New York, 2004.

[23] K. C. Joshi,”The formation of ultrasonic wire bonds between metals,” *Welding J.,* Vol. 50, pp. 840 - 858, 1971.

[24] J. E. Krzanowski, N. Murdeshwar,”Deformation and bonding processes in aluminum ultrasonic wire wedge bonding,” *J. Electron. Mater.,* Vol. 19, pp. 919 - 924, 1990.

[25] J. K. Kim and B. L. Au,”Effects of metallization characteristics on gold wire bondability of organic printed circuit boards,” *J. Electron. Mater.,* Vol. 30, pp. 1001 - 1011, 2001.

[26] G. Harman and J. Albers,”The ultrasonic welding mechanism as applied to aluminum- and gold-wire bonding in microelectronics,” *IEEE Trans. Parts, Hybrids, Packag.*,Vol. PHP-13, pp. 406 - 412, 1977.

[27] M. Weissenfelt, P. Collander, E. Jarvinen, T. Laurinolli, “A practical method for evaluating and adjusting ultrasonic wire bonding process,” in *Proc. 29th Electro. Comp. Conf.*, 1979, pp. 309 - 314.

[28] Y. Zhou, X. Li, N. J. Noolu,”A footprint study of bond initiation in gold wire crescent bonding,” *IEEE Trans. Compon. Packag. Manuf. Technol. Part A*, Vol. 28, pp. 810 - 816, 2005.

[29] I. Lum, M. Mayer, Y. Zhou,”Footprint study of ultrasonic wedge-bonding wire aluminum wire on copper substrate,”*J. Electron. Mater.*, Vol. 35, pp. 433 - 442, 2006.

[30] K. C. Joshi,”The formation of ultrasonic bonds between metals,” *Welding J.,* Vol. 50, pp. 840 - 848, 1971.

[31] B. Langenecker,”Effects of ultrasound on deformation characteristics of metals,” *IEEE Trans. Sonics Ultrasonics,* Vol. SU-13, pp. 1 - 8, 1966.

[32] G. A. Hayes and J. C. Shyne,”The influence of ultrasonic energy on kinetic processes in solids” *IEEE Trans. Sonics Ultrasonics*, Vol. SU - 16, pp. 68 - 75, 1969.

[33] A. Schneuwly, P. Groning, L. Schlapbach, and V. P. Jaecklin, "Influence of surface contamination on metal/metal bond contact quality,"*J. Electron. Mater.*, Vol. 27, pp. 990 - 997, 1998.

[34] Brunner, “Tail bond strength measurement - feasibility report” K&S internal report ,1999.

[35] K.S Goh, Z. W. Zhong, "Two capillary solutions for ultra-fine-pitch wire bonding and insulated wire bonding," *Microelectron. Eng.* Vol. 84, pp. 362 - 367, 2007.

[36] J. Schwizer, “CMOS force sensors for wire bonding and flip chip process characterization,” Dissertation, ETH No. 15293, Zurich, 2003.

[37] "ITRS (2006): International technology roadmap for semiconductors - assembly & packaging, Updated, pp. 1 - 19. Available: http://www.itrs.net.

[38] J. Onuki, M. Koizumi, I. Araki, "Investigation of the reliability of copper ball bonds to aluminum electrodes," *IEEE Trans. Comp. Hybrids. Manuf. Technol.,* Vol. CHMT-12, pp. 550 - 555, 1987.

[39] Saraswati, E. P. P. Theint, D. Stephan, H. M. Goh, E. Pasamanero, D. R. M. Calpito, F. W. Wulff, and C. D. Breach, "High temperature storage (HTS) performance of copper ball bonding wires," in *Proc. Electron. Packag. Technol. Conf.* 2005, pp. 602 - 607.

[40] K. S. Goh, Z. W. Zhong, "A new bonding tool solution to improve stitch bondability," *Microelectron. Eng.* Vol. 84, pp. 173 - 179, 2007.

[41] N. Srikanth, S. Murali, Y. M. Wong, C. Vath 3, "Critical study of thermosonic copper ball bonding," *Thin Solid Films*, Vol. 462 - 463, pp. 339 - 345, 2004).

[42] F. W. Wulff, C. D. Breach, D. Stephan, Saraswati, K. Dittmer and M. Garnier, "Further characterization of intermetalic growth in copper and gold ball bonds on aluminum metallization," in *Proc. SEMICON Singapore,* 2005, pp. 35 - 43.

[43] D. Calpito, I. Qin, E. Pasamanero, E. Theint, and T. C. Wei,"Very long, ultra-low loop testing for new bonding wire development," in *Proc. SEMICON Singapore*, 2006, pp. 1 - 8.

[44] H. K. Kung, "Evaluation of sweep resistance of Q Auto - loop and Square - loop bonds for semiconductor packaging technology," *Microelectron. Reliab.,* Vol. 47, pp. 1103 - 1112, 2007.

[45] Y. F. Yao, B. Njoman, K. H. Chua, T. Y. Lin, "New encapsulation development for fine pitch IC devices," *Microelectron. Reliab*., Vol. 45, pp. 1222 - 1229, 2005.

[46] Y. F. Yao, T. Y. Lin, K. H. Chua, “Improving the deflection of wire bonds in stacked chip scale package (CSP),” *Microelectron. Reliab.,* Vol. 43, pp. 2039 - 2045, 2003.

[47] T. Yoshihara, M. Yuki, T. Hayashida, Y. Ohno,” Factors governing wire sweep in plastic IC encapsulation,” *Electron. Commun. Jpn. Part 2 Electron*., Vol. 82, pp. 59 - 67, 1999.

[48] A. Hmiel, R. Wicen, S. Tang,”A novel process for protecting wire bonds from sweep during molding,” in *Proc. IEEE/CPMT Int. Electron. Manuf. Technol. IEMT Symp.,* 2002, pp. 335 - 341.

[49] M. C. Pauet, A. Tremblay, S. Ouimet. R. Tetreault, R. Toutant, ”Improvements and alternatives for ultra fine pitch encapsulation,” in *Proc. Electron. Compon. Technol. Conf.,* 2001, pp. 203 - 209.

[50] R. Lyn, J. Persic, and Y. K. Song,”Overview of X-Wire^{TM} Insulated Bonding Wire Technology,” in *Proc. IMAPS Conf.,* 2006, pp 1-7.

[51] B. Hatton, K. Landskron, W. Hunks, M. Bennett, D. Shhukaris, D. Perovic, and G. Ozin, “Materials chemistry for low - k materials,” *Materialstoday*, Vol. 9, pp. 22 - 31, 2006.

[52] J. Tan, Z. W. Zhong, H. M. Ho, “Wire-bonding process development for low - k materials,” *Microelectron. Eng.,* Vol 81, pp. 75 - 82, 2005.

[53] S. Narasimalu, “Wire bond challenges in low - devices,” *Microelectron. Int.* Vol. 25, pp 34 - 40, 2008.

[54] H. Koyama, H. Shiozaki, I. Okumura, S. Mizuqashira, H. Hiquchi, T. Ajiki, “A new bond failure wire crater in surface mount device,” in *Proc. 26th annual Reliability Pysics*, 1988, pp. 59 - 63.

[55] T. C. Wei and A. R. Daud, “Cratering on thermosonic copper wire ball bonding,” *J. Mater. Eng. Perform.* Vol 11, pp. 283 - 287, 2002.

[56] A. Viswanath, X. Zhang, V. P. Ganesh, and L. Chun, “Numerical study of gold wire bonding process on Cu/Low - k structures," *IEEE Trans. Adv. Packag.* Vol. 30, pp. 448 - 456, 2007.

[57] Y. Liu, S. Irving, and T. Luk, “Thermosonic wire bonding process simulation and bond pad over active stress analysis,” in *Proc. 54th Electron. Comp. Technol. Conf.,* 2004, pp. 383 - 391.

[58] K. Yoyozawa, K. Fujita, S. Minamide, T. Maeda, “Development of copper wire bonding application technology,” in *Proc. Electron. Compon. Conf.,* 1990, pp. 762 - 767.

[59] I. Lum, “Effect of ultrasound in microelectronic ultrasonic wire bonding,” Dissertation, University of Waterloo, Canada, 2007.

[60] V. Wincheli and H. Berg, “Enhancing ultrasonic bond development,” *IEEE Trans. Comp. Hybrids, Manuf. Technol*., Vol. CHMT - 1, pp. 211 - 219, 1978.

[61] Y. J. Kim, J. S. Kim, J. Y. Chung, S. H. Na, J. Y. Kim, S. B. Kim, “Low - k wire bonding,” in *Proc. Electron. Comp. Technol. Conf.,* 2006, pp. 1616 - 1622.

[62] M. Saran, R. Cox, C. Martin, G. Ryan, T. Kudoh, M. Kanasugi, “Elimination of bond - pad damage through structural reinforcement of intermetal dielectrics,” in *Proc. IEEE 36th Annu. Reliabil. Phys. Symp.,* 1998, pp. 225 - 231.

[63] M. Sheaffer, L. Levine, and B. Schlain, “Optimizing the wire bonding process for copper ball bonding, using classic experimental design,” *IEEE Trans. Compon. Hybrids, Manuf. Technol.,* CHMT-10, pp. 321 - 326, 1987.

[64] J. Antony, “Improving the wire bonding process quality using statistically designed experiments,” *Microelectron. J.,* Vol. 30, pp. 161 - 168, 1999.

[65] N. E. Zhang, G. A. Stenback, D. M. Wardrop, “Interval Estimation of the process capability index,” *Commun. Stat.: Theory and Methods,* Vol. 19, pp. 4455 - 4470, 1990.

[66] S. Lambert, “The influence of temperature on the efficiency of electroplating from various ionic liquids,” *Circuit world*, Vol. 32, pp. 36 - 41, 2006.

[67] R. D. Srivastava, A. K. Agarwal and R. Sharma, “ Studies on electrolytic Cu-Ni alloy plating,” *Surf. Technol.,* Vol. 9, pp. 171 - 178, 1979.

[68] I. Kenny, J. C. Mitchell, and G. Walsh, “Gold plating on spectacle frames,” *Phathal. Physiol. Opt.,* Vol. 17, pp. 263 - 266, 1997.

[69] S. Ouimet and M. Paquet, ”Overmold technology applied to cavity down ultrafine pitch PBGA package,” *IEEE Trans. Adv. Packag*. Vol. 22, pp. 123 - 128, 1999.

[70] S. Han, K. K. Wang, ”Effects of fillers on wire sweep in semiconductor chip encapsulation,” *IEEE Trans. Comp. Packag. Manuf. Technol. Part B,* Vol. 18, pp. 744 - 750, 1995.

[71] K. K. Shih and J. M. Blum, “Contact resistances of Au-Ge-Ni, Au-Zn and Al to 3-5 Compounds," *Solid state Electron.,* Vol. 15, pp. 1177 - 1180, 1972.

[72] D. K. Schroder, “Semiconductor material and device characterization” John Wiley & Sons, Inc, New York, 1998.

[73] H. Ji, M. Li, C. Wang, J. Guan, H. S. Bang, ”Evolution of the bond interface during ultrasonic Al-Si wire wedge bonding process,” *J. Mater. Process. Technol.,* Vol 182, pp. 202 - 206, 2007.

[74] M. Weissenfelt, P. Collander, E. Jarvinen, T. Laurinolli, “A practical method for evaluating and adjusting ultrasonic wire bonding process,” in *Proc. 29th Electro. Comp. Conf.,* 1979, pp. 309 - 314

[75] Y. Ding, J. K. Kim, P. Tong, ”Numerical analysis of ultrasonic wire bonding: Effects of bonding parameters on contact pressure and frictional energy,” *Mech. Mater.,* Vol. 38, pp. 11 - 24, 2006

[76] Y. H. Chan, J. K. Kim, D. Liu, P. C. K. Liu, Y. M. Cheung, and M. W. Ng, “Effect of plasma treatment of Au-Ni-Cu bond pads on process window of Au wire bonding,” *IEEE Trans. Adv. Packag.,* Vol. 28, pp. 674 - 684, 2005.

[77] Y. S. Lin, “ A surface analysis on oxygen plasma-cleaned gold pattern-plated substrates for wire bondability,” *Surf. Coat. Technol.,* Vol. 173, pp. 47 - 57, 2003.

[78] Zhang, Stenback and Wardrop, “Interval Estimation of the process capability index,” *Commun.stat.:Theory and Methods,* Vol. 19, pp. 4455 - 4470, 1990.

[79] H. Koyama, H. Shiozaki, I. Okumura, S. Mizugashira, H. Higuchi, T. Ajiki, “A new bond failure wire crater in surface mount device,” *in Proc. Annu. Reliabil. Phys. Symp.,* 1998, pp. 59 - 63.

[80] Certification of compliance provided by MKE with bonding wires.

[81] J. Onuki, M. Koizumi, H. Suzuki, I. Araki, T. Iizuka, “Influence of ball - forming conditions on the hardness of copper balls,” *J. Appl. Phys,.* Vol. 68, pp. 5610 - 5614, 1990.

[82] T. Shima and J. Tominaga, “Optical transmittance study of silver particles formed by AgO_x thermal decomposition,” *J. Vac. Sci. Technol.,* Vol. A21, pp. 634 - 637, 2003.

[83] I Lum, J. P. Jung, Y. Zhou, ”Bonding mechanism in ultrasonic gold ball bonds on copper substrate,” *Metall. Mat. Trans. A,* Vol. 36A, pp 1279 - 1286, 2005.

[84] J. Qi, N. C. Hung, M. Li, D. Liu, ”Effects of process parameters on bondability in ultrasonic ball bonding,” *Scripta Mater.,* Vol. 54, pp. 293 - 297, 2006.

[85] I. Lum, M. Mayer, Y. Zhou, ”Imprint study of ultrasonic wedge bonding with aluminum wire on copper substrate,” *J. Electro. Mater.,* Vol 35, pp. 433 - 441, 2006.

[86] M. Mayer and J. Schwizer,”Thermosonic ball bonding model based on ultrasonic friction power,” in *Proc. Electron. Packag. Technol. Conf.,* 2003, pp. 739 - 743.

[87] ASTM Standard - F219 - 96:Standard test methods of testing fine round and flat wire for electron devices and lamps, ASTM International, 2002, pp. 1 - 3.

[88] A. Yamashita, Z. Horita, T. G. Langdon, “Improvement the mechanical properties of magnesium and a magnesium alloy though severe plastic deformation,” *Mater. Sci. Eng.,* Vol. A300, pp. 142 - 147, 2001.

[89] S. L. Khoury, D. J. Burkhard, D. P. Galloway, T. A. Scharr, ”A comparison of copper and gold wire bonding on integrated circuit devices,” *IEEE Trans. Compon. Hybrids, Manuf. Technol.,* Vol. 13, pp. 673 - 681, 1990.

[90] I. Singh, J. Y. On, L. Levine, ”Enhancing fine pitch, high I/O devices with copper ball bonding,” in *Proc. Electron. Compon. Technol Conf.,* 2005, pp. 843 - 847.

[91] A. Undisz, U. Zeigmeister, M. Rettenmayr, M. Oechsle, ”On the mechanism of internal oxidation in platinum-zirconium alloys. A TEM study,” *J. Alloy Compd.,* Vol. 438, pp. 178 - 183, 2007.

[92] C. Thorning, S. Sridhar, ”The role of grain boundary diffusion in initial selective oxidation kinetics of a manganese-aluminum TRIP steel,” *J. Phase Equilib. Diffus.,* Vol. 26, pp. 539 - 546, 2005.